Fiber-coupled Ultra-high-Q Microresonators for Nonlinear and Quantum Optics

Thesis by

Sean Michael Spillane

In Partial Fulfillment of the Requirements

for the Degree of

Doctor of Philosophy

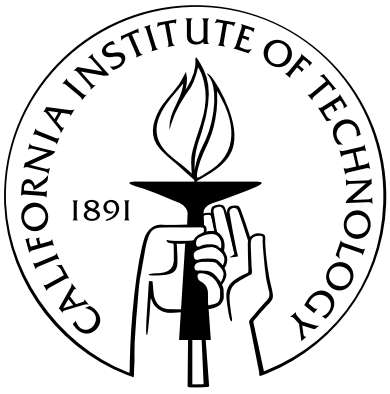

California Institute of Technology

Pasadena, California

2004

(Defended May 25, 2004)

To my family and Cecily

Acknowledgements

First of all, I would like to thank my thesis advisor, Prof. Kerry Vahala, for his guidance throughout my time at Caltech. The creative freedom and independence he encouraged was invaluable for understanding the rigors of scientific research. I am also indebted to Prof. Oskar Painter for many insights throughout my graduate career. Our numerous discussions have shown me how to recognized and focus on the truly novel aspects of research.

I have learned much from the many members of the Vahala group that I have had the opportunity to interact with (Deniz Armani, Andrea Martin, Tal Carmon, Bumki Min, Hosein Rokhsari, and Lan Yang). They have been instrumental in my maturity as a scientist. Special thanks also goes to Rosalie Rowe, who has been extremely helpful in day to day administrative matters.

I would also like to acknowledge Kevin Parkin, Carlos Romero, Julie Liu, and Robert Strittmatter for their friendship over the years. They have been there to listen to my many frustrations with graduate school and have been a welcome reservoir of support and entertainment which has made my time at Caltech much more enjoyable.

I would like to specifically thank Ashish Bhardwaj for his genuine interest in my scientific progress. His unwavering support and promotion on my behalf are extremely rare, which I will never forget. I wish him all the best and hope that I get the chance again to work with him in a scientific setting.

In particular, I would like to acknowledge Tobias Kippenberg for his innumerable contributions in the progression of this thesis, and especially for the many enlightening technical discussions over drinks. His enthusiasm, excitement, and voice of reason were essential in the sometimes lonely and frustrating times of graduate school. I can honestly say that the quality of this thesis would not be the same without his friendship.

My family has been instrumental in my success throughout the years. Without their love

and support I would not be the person I am today.

And finally, in this short space I cannot fully express my gratitude to Cecily for her patience and unconditional support over the last few years. Her love and devotion has been truly inspirational.

Abstract

The ability to confine optical energy in small volumes for long periods of time is desirable for a number of applications, ranging from photonics and nonlinear optics, to fundamental studies in quantum electrodynamics. Whispering-gallery-mode microresonators are a promising cavity to study, due to the ability to obtain quality factors exceeding 100 million in micron-scale volumes. This thesis investigates the suitability of ultra-high-quality factor silica microresonators (both silica microspheres and silica toroidal microresonators) for nonlinear and quantum optics. Crucial to the actual use of these structures is the ability to efficiently excite and extract optical energy. The first part of this thesis investigates the ability to achieve near lossless coupling between a fiber-taper waveguide and a silica microresonator. It is shown that a coupling ideality (which is the fraction of energy coupled into the desired fiber mode) in excess of 99.97% is possible, meaning that optical energy can be coupled both to and from the optical resonator with near perfect efficiency.

Using tapered fibers, low threshold stimulated Raman scattering is observed in both silica microspheres and silica microtoroids at record low incident pump powers below 100 microwatts, much lower than previous devices. High conversion efficiencies ($> 35\%$) are also realized. Furthermore, the conditions for optimized performance of both stimulated Raman scattering and parametric oscillation in a microcavity are described.

Lastly, the suitability of toroidal microcavities for strong coupling cavity quantum electrodynamics is investigated. Numerical modeling of the optical modes demonstrates a significant reduction of modal volume with respect to spherical cavities, while retaining high quality factors. The extra degree of freedom of toroid microcavities can be used to achieve improved strong-coupling characteristics, and numerical results for atom-cavity coupling strength, critical atom number and critical photon numbers for cesium are calculated and shown to exceed values currently possible using Fabry-Perot cavities. Modeling predicts atom-cavity coupling

rates exceeding 700 MHz and critical atom numbers approaching 10^{-7}.

Contents

List of Figures

List of Tables

Chapter 1

Introduction

A high-Q resonant structure allows the temporal storage and buildup of optical energy. It has been well-known that spherical cavities possess whispering-gallery-type modes which can in principle be confined for a very long time through total internal reflection on the cavity interface. Braginsky and Ilchenko [1] realized that the whispering-gallery modes of dielectric silica microspheres had the potential to experimentally exhibit extremely long photon storage times, exceeding a microsecond. This allowed the realization of low threshold optical microcavity effects, such as lasing and nonlinear wave generation [2]. Experimental work by Vernooy et al. [3] has demonstrated a record quality factor as high as 9 billion, limited only by the optical absorption of silica. This ability to confine light for a significant amount of time in a small volume had profound implications for many different areas [4]. The strong dependence of the optical resonance position and width on the cavity surface characteristics allows probing of the external environment, such as high sensitivity detection of chemical or biological species [5]. Furthermore, the low optical loss of silica microcavities allows the creation of lasers with submicrowatt thresholds [6].

The large amount of resonant power buildup in ultra-high-Q microcavities means that for an input power of 1 mW coupled into a cavity with a quality factor of 100 million (readily achievable in silica microspheres), the circulating power is on the order of 100 Watts. Furthermore, since all this power is concentrated into a small dielectric volume, below 1000 cubic microns, circulating intensities of 1 GW/cm^2 are reached. This value in is the regime where nonlinear effects, even in a weakly nonlinear material such as silica, can be observed [7].

The study of nonlinear optics in microcavities was pioneered by the work of Richard Chang and Anthony Campillo on highly nonlinear liquid microdroplets. They found that it was pos-

sible to obtain a wide variety of nonlinear optic effects, including stimulated Raman scattering [8, 9] and stimulated Brillouin scattering [10], at very low input thresholds (on the order of milliwatts of input power). Already, this threshold was comparable to or less than other nonlinear devices, such as nonlinear silica fiber lasers [11] and hydrogen-filled laser cavities [12]. However, while liquid microdroplets could attain low nonlinear thresholds, they were unsuitable for long-term investigations and practical photonics applications. Thus, silica microspheres were a natural solid-state analogue to investigate [13], with numerous theoretical predictions of substantially lower nonlinear thresholds [1, 14]. However, experimental realization of nonlinear effects was solely limited to either thermal effects [15] or a single study of the Kerr effect in a low temperature microsphere [16].

Before the use of ultra-high-Q microresonators for photonics applications could advance, the problem of efficient excitation and extraction of optical energy from these structures needed to be solved. Most previous studies of silica microspheres used glass prisms and free-space laser beams to excite the cavity [17]. While this method is relatively efficient, the true advantages of these structures could not be realized, due to both the inability to obtain complete power transfer into the cavity and to extract the optical energy in a manner convenient to further manipulation. Using fiber-optic technology was investigated, with side-polished fibers and fiber half-block couplers used to add compatibility with fiber-optic systems [18]. However, these methods, while an improvement in some areas, did not allow the full potential of silica microspheres to be realized. In 1997, Birks et al. presented a paper which described the coupling between a fiber taper and a silica microsphere [19]. They showed that it was possible to efficiently couple into a microsphere. Vahala et al. then realized that this coupling method should in principle allow near perfect coupling efficiency both into and out of a silica microresonator, while the ability to create near lossless tapers allows significant advantages in fiber compatibility. The beneficial aspects of fiber-tapers allowed Cai et al. to realize true critical coupling in the optical domain, where the optical filtering from the fiber coupler allowed the resonant transmission through the fiber to vanish [20].

I have followed up upon this work and have showed that it is possible to not only couple energy efficiently into a silica microsphere, but also to extract the optical output with efficiencies above 99% [21]. This fact conclusively proved that by using fiber-tapers, complete power

transfer from the fiber to the cavity is achievable. Tobias Kippenberg and I have used this fact to observe nonlinear stimulated Raman scattering in a silica microsphere, with optical thresholds below 100 microwatts, by far a record value over other types of Raman lasers [22].

However, the use of silica microspheres is not ideal for applications, as not only does this structure possess a complicated (but well-understood) mode and lasing spectrum, but their fabrication process does not lead to easy integration onto a microelectronic chip. Previous microcavities, which are easily controllable and integrable do not, however, possess the high-quality factors necessary to enable low threshold nonlinear operation [23, 24]. Deniz Armani and I developed a process to merge the integrability and control of planar microfabricated resonators, with the high quality factors of silica microspheres. The resultant structures consist of a toroidally shaped silica cavity supported on a silicon chip [25]. These structures were also found to have advantages over spherical cavities by the ability to modify the toroidal geometry [26, 27]. However, the modal properties are not easily solvable in this cavity structure. Numerical characterization of the optical properties of these structures indicates benefits over spherical cavities, which have been experimentally verified.

The use of a high-Q optical microcavity can also dramatically change the spontaneous emission characteristics of atoms, as predicted by Purcell [28] and later investigated by Kleppner [29]. When the optical cavity loss and mode volume becomes small enough, an atom can coherently interact with the cavity for a substantial period of time [30]. This capability is desirable for quantum information studies [31, 32, 33], where the future use of quantum systems envisions a combination of a quantum medium interacting with optical microcavities and fiber-optic networks to transport the quantum fields [34, 35, 36]. Thus, the combination of a high-Q, small mode volume microcavity with low-loss fiber coupling and transport is needed. Chip-based silica toroidal resonators are a promising candidate to satisfy these requirements. The last part of this thesis discusses the capabilities of toroids to obtain strong-coupling between an atomic medium and the cavity electromagnetic field.

Thesis Outline

Chapter 2 begins by describing the general terminology used to characterize optical microcavities. Then, the fabrication and optical properties of both silica microspheres and silica toroidal microresonators are investigated and numerical calculations of the modal properties

of these two geometries are presented. In Chapter 3 the conditions for efficient coupling with fiber-optic tapers are discussed and experimentally investigated. Chapter 4 first derives the conditions for stimulated Raman scattering and Parametric oscillation in a microcavity. Then, experimental results are presented for Raman lasing in both silica microspheres and silica microtoroids. Chapter 5 discusses the suitability of microtoroids for strong-coupling cavity QED, by numerically investigating the modal properties for coupling to a cesium atom. Comparison with competing cavity types is also given. And lastly, Chapter 6 presents a brief summary.

Chapter 2

Optical microcavities

2.1 General properties of microcavities

Optical microcavities [2] consist of resonant structures where the cavity dimensions are on the order of a small multiple of the wavelength of light. The main properties of interest in a microcavity are the following:

Quality factor Q:

The loss of a resonant cavity is an important parameter, as it strongly determines the potential applicability of a cavity for many different areas. Cavity loss is commonly expressed in terms of quality factor, which is related both to the linewidth $\Delta\lambda$ of the resonance located at λ, and to the cavity photon lifetime τ through the equation,

$$Q = \frac{\lambda}{\Delta\lambda} = \omega\tau \tag{2.1}$$

where ω is the optical frequency ($\omega = 2\pi c/\lambda$). This intrinsic relation between cavity photon lifetime and cavity bandwidth illustrates the role quality factor plays in determining the resonant bandwidth and loss for passive cavity filtering, and also in the determination of thresholds for active processes such as lasing and nonlinear optical wave generation. The overall quality factor of a whispering-gallery-mode cavity is due to many mechanisms [37], which can be decomposed into the following equation:

$$\begin{aligned} 1/Q_{total} &= 1/Q_{mat} + 1/Q_{WGM} + 1/Q_{ss} + 1/Q_{contam} + 1/Q_{coupling} \\ &= 1/Q_{intrinsic} + 1/Q_{coupling} \end{aligned} \tag{2.2}$$

where Q_{total} denotes the total cavity quality factor. The intrinsic cavity quality factor $Q_{intrinsic}$ is due to contributions from both the resonator material loss (Q_{mat}), radiation loss present in a curved dielectric cavity (Q_{WGM}), scattering from surface imperfections (Q_{ss}), and any contaminate on either the cavity surface or inside the dielectric (Q_{contam}). $Q_{coupling}$ represents the energy loss due to input/output coupling. Strictly speaking, this separation of each contribution to cavity loss is only valid when each loss is weak, such that only a small fraction of the optical energy is lost upon each round-trip in the cavity [38]. However, for all the studies in this work this approximation holds, as both the use of ultra-high-Q resonators and fiber couplers satisfy these conditions.

Free spectral range:

The free spectral range (FSR) of a cavity represents the frequency (wavelength) spacing between successive longitudinal modes. This definition, commonly used for Fabry-Perot (FP) cavities, is somewhat ambiguous for the cavities in this work, as the mode spectrum is highly complex. However, by using the most direct analogy to a FP, a microresonator can be considered a FP cavity wrapped around onto itself, such that the periphery of the resonator corresponds to the FP mirror spacing. By doing this, the modes which determine the FSR are the successive modes which have the same transverse mode structure. For an azimuthally-symmetric resonator of radius R and refractive index n[1], the FSR is approximated by

$$\begin{aligned} \Delta\nu_{FSR} &= \frac{c}{2\pi nR} \\ \Delta\lambda_{FSR} &= \frac{\lambda^2}{2\pi nR} \end{aligned} \tag{2.3}$$

For a typical microcavity with a diameter of 30 microns, and a refractive index of 1.45 at a wavelength of 1550 nm, this expression gives a FSR of 17.6 nm, very close to the exact answer of 17.9 nm (by directly solving the modes of a microsphere, as discussed in section 2.2.2). As a side note, this large mode spacing is one of the reasons microresonators have obtained so much interest, for fields ranging from channel-dropping components in telecommunications [39] to single-mode laser sources [23].

[1]More accurately, n should be replaced by the effective index of the optical mode, n_{eff}. This is also true for the formulas of cavity finesse and buildup factor. However, for a simple estimate the use of the material refractive index is convenient.

Finesse:

Finesse ($\mathcal{F}$) is the ratio of the cavity mode spacing to the cavity bandwidth. This definition factors in both the cavity loss (Q) and cavity mode spacing (FSR) to obtain a dimensionless single parameter which characterizes the ability to resolve the cavity resonance structure, as given by

$$\mathcal{F} = \frac{\Delta\lambda_{FSR}}{\Delta\lambda} = \frac{\lambda Q}{2\pi n R} \tag{2.4}$$

Knowledge of cavity finesse is useful for a wide range of subjects, as it determines several properties, for example, the amount of spectral noise/power a resonant filter passes, and the amount of energy amplification in a resonant system. Cavity finesses in ultra-high-Q whispering-gallery microresonators can exceed 10^6 [3], with the record for an optical resonator determined in the course of this work.

Mode volume:

The volume that each cavity mode occupies is dependent on the cavity resonant field distribution, which in turn depends on the particular cavity geometry. Modal volume plays a fundamental role in many applications of microcavities [4], resulting in optical energy that is tightly confined to physical volumes on the order of hundreds to a couple thousand cubic microns (in some cases even below a cubic micron [40, 41, 42]). This coupled with the low loss possible in high-Q microcavities results in a very large energy density in the cavity. These large energy densities are of use for areas ranging from nonlinear optical wave generation [22] to quantum optics, where the large electric field per photon can allow a strong interaction with an atomic system [30]. There are a number of definitions of modal volume, but this work will focus on two of them, the quantum mode volume,

$$V_m = \frac{\int_{V_Q} \epsilon(\vec{r})|\vec{E}|^2 d^3\vec{r}}{|\vec{E}_{\max}|^2} \tag{2.5}$$

and the nonlinear modal volume,

$$V_m^{NL} = \frac{(\int_{V_Q} |\vec{E}|^2 d^3\vec{r})^2}{\int_{V_Q} |\vec{E}|^4 d^3\vec{r}} \tag{2.6}$$

where $|\vec{E}|$ represents the cavity electric field, $\epsilon(\vec{r}) = n^2(\vec{r})$ the refractive index at $\vec{r}$ squared, and V_Q denotes the integration volume. These are so named as equation 2.5 is used in determining the quantum interaction of an atom and an electromagnetic field [43], and equation 2.6 is common in describing nonlinear wave generation in optical media[2] [11, 1].

Circulating power:

One of the benefits of the long photon storage time in high-Q microcavities is that they can build up a significant internal circulating power with low pump powers. This cavity build-up factor is expressed by

$$\frac{P_{circ}}{P_{input}} = \frac{\lambda Q_0}{\pi^2 n R} \frac{K}{(1+K)^2} \tag{2.7}$$

where Q_0 denotes the intrinsic cavity Q and $K \equiv Q_0/Q_{coupling}$ is the ratio of the intrinsic cavity photon lifetime (equivalently Q) to the photon lifetime due to coupling. This formula indicates that the cavity buildup factor is proportional to Q, explaining why ultra-high quality factor cavities can result in a substantial amplification of the input resonant field energy. For the resonators studied in this work, the build-up factor is on the order of 10^5 to 10^6 for optimal coupling conditions, which allows the attainment of very large circulating powers ($>$ 100 Watts) with modest input powers (1 mW).

2.2 Silica microspheres

Spherical microcavities are the most common type of structures which possess ultra-high quality factors. Their optical properties have attracted much interest, ranging from optical diagnostics of liquid microdroplets [8], to the study of very low threshold lasing and nonlinear processes in solid silica microspheres [1, 6]. From a practical standpoint, the use of silica microspheres as a high-Q cavity is advantageous, as they have been extensively studied, and are readily produced.

[2]For silica microcavities these two definitions give near equivalent values.

2.2.1 Fabrication

The beauty of silica microspheres is that they are very easily produced in a laboratory setting. Upon heating the end of a silica preform, such as a quartz rod or optical fiber (as used in this thesis), the end reflows to form a spherical volume under the influence of surface tension. Due to the high viscosity of silica, the reflowed structure is both highly spherical (eccentricities on the order of 1-2%), and extremely uniform. The spherical surface has very low intrinsic roughness (measured on the order of 1 nm), and thus has a very small surface scattering loss [3]. For the work in this thesis the reflow process was performed with a CO_2 laser [13], which allows the creation of small spherical cavities, ranging from below 20 microns to over 100 microns. Figure 2.1 shows an optical micrograph of a silica microsphere. The sphere is attached to the fiber stem from which it was formed. The presence of the fiber stem can usually be ignored, as the excited optical modes typically lie in the equatorial plane and thus has negligible overlap with this perturbed region.

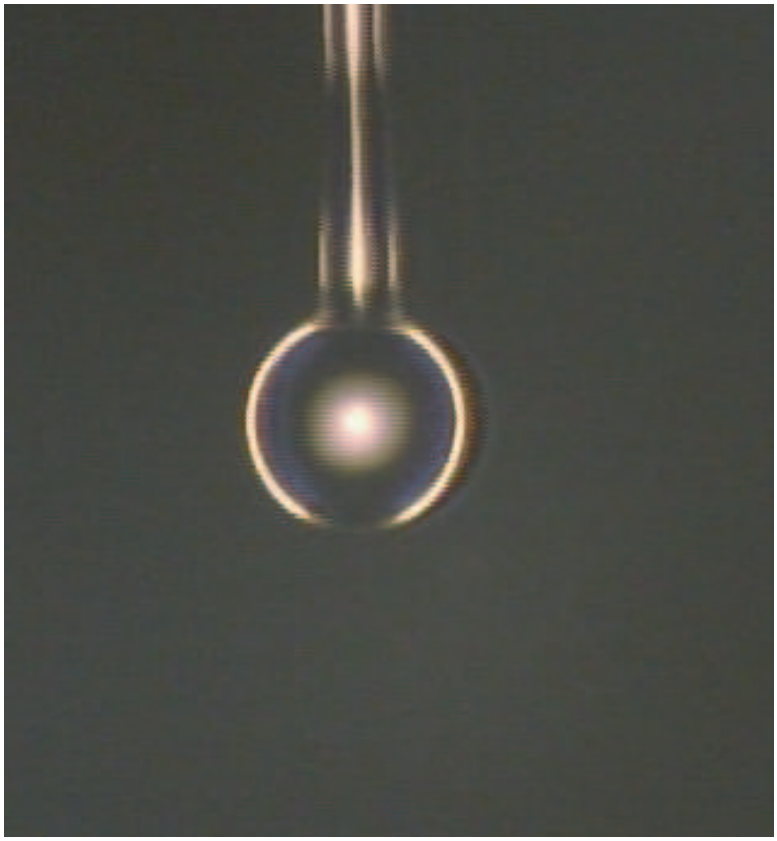

Figure 2.1: Optical micrograph of a silica microsphere with a diameter of approximately 30 microns. The sphere is attached to the end of a tapered optical fiber from which it was formed.

2.2.2 Optical properties

The optical modes of a spherical dielectric cavity are very well known, and can be derived explicitly by consideration of Helmholtz's equation in spherical coordinates [44, 45]. The modes are characterized by a set of four quantum numbers (q, l, m, p), where q denotes the radial mode order, l and m the angular quantum numbers, and p the polarization (TE or TM). For a dielectric cavity of radius R and refractive index n (the external index is assumed to be unity) the optical fields are given by [2],

$$\begin{aligned}
\vec{E}^{TE}(r,\theta,\phi) &= \begin{cases} j_l(nkr)\vec{X}_{lm}(\theta,\phi) & \text{if } r < R \\ j_l(nkR)h_l^{(1)}(kr)/h_l^{(1)}(kR)\vec{X}_{lm}(\theta,\phi) & \text{if } r > R \end{cases} \\
\vec{B}^{TE}(r,\theta,\phi) &= -\frac{1}{k}\nabla \times \vec{E}(r,\theta,\phi) \\
\\
\vec{B}^{TM}(r,\theta,\phi) &= \begin{cases} j_l(nkr)\vec{X}_{lm}(\theta,\phi) & \text{if } r < R \\ j_l(nkR)h_l^{(1)}(kr)/h_l^{(1)}(kR)\vec{X}_{lm}(\theta,\phi) & \text{if } r > R \end{cases} \\
\vec{E}^{TM}(r,\theta,\phi) &= -\frac{1}{\epsilon(\vec{r})k}\nabla \times \vec{B}(r,\theta,\phi)
\end{aligned} \tag{2.8}$$

where $\vec{X}_{lm} = [l(l+1)]^{-1/2}\vec{L}Y_{lm}$ denotes the vector spherical harmonics (with $\vec{L} = \vec{r} \times i\nabla$), and j_l and $(h_l^{(1)})$ represent the spherical Bessel (Hankel) functions, respectively. The resonance position and width are obtained by solving the characteristic equation [46],

$$n^{1-2b}\frac{[nkRj_l(nkR)]'}{nkRj_l(nkR)} = \frac{[kRh_l^{(1)}(kR)]'}{kRh_l^{(1)}(kR)} \tag{2.9}$$

where b represents the polarization of the optical mode (1 for TM and 0 for TE). The prime denotes differentiation with respect to the argument. This equation accounts for radiation through the use of an outgoing wave boundary condition outside the cavity, as given by the complex Hankel function of the first kind. Solution of this equation results in a complex wavenumber, $k = k_r + ik_i$, which determines both the resonance wavelength ($\lambda = 2\pi/k_r$) and the radiation quality factor ($Q_{rad} = k_r/(2k_i)$).

2.2.2.1 Resonance locations

The numerical solution of equation 2.9 gives directly the resonant wavelength for a given set of mode numbers. While this is readily solvable with a computer, an analytic approximation is useful for quick insight. There have been a number of approximate expressions for the resonance locations of a sphere [47], all based on asymptotic expansions of the characteristic equation, valid for high l numbers. Below is one of the more accurate expressions, obtained by Schiller [48]:

$$2\pi R/\lambda = \frac{\nu}{n} - \frac{\zeta_q}{n}(\frac{\nu}{2})^{1/3} + \sum_{k=0}^{k_{max}} \frac{d_k(n,\zeta_q)}{\nu^{k/3}(n^2-1)^{(k+1)/2}} \tag{2.10}$$

where n is the refractive index inside the sphere (external index assumed to be unity), ζ_q is the q^{th} zero of the Airy function (q denotes the radial mode order), and $\nu = l{+}1/2$. The coefficients $d_k(n,\zeta_q)$ up to $k_{max} = 8$ are tabulated in reference [48], with the first four coefficients given by

$$\begin{aligned} d_0 &= -p \\ d_1 &= 2^{1/3}3(n^2-1)\zeta_q^2/(20n) \\ d_2 &= -2^{2/3}n^2p(-3+2p^2)\zeta_q/6 \\ d_3 &= \frac{350n^4(1-p)p(-1+p+p^2) + (n^2-1)^2(10+\zeta_q^3)}{700n} \end{aligned}$$

With $p = 1$ for TE modes and $p = 1/n^2$ for TM modes.

2.2.2.2 Quality factor

The quality factor of a spherical cavity is made up of all the loss contributions mentioned in section 2.1 [49]. Consideration of the intrinsic silica absorption limited Q results in a quality factor exceeding 10 billion for resonant wavelengths covering 850 nm to past 1600 nm. In practical structures (such as the structures in this work) the measured intrinsic quality factors are much lower than this value, and therefore other loss mechanisms must dominate. For smaller cavity sizes, the radiation loss due to the curvature of the dielectric interface can play a crucial role. While the radiation loss can be easily found through solution of equation 2.9, a simple approximate expression can be used to gain insight into the scaling of radiation loss

as a function of the cavity parameters [46]:

$$Q_{rad} = \frac{1}{2}\left(l+\frac{1}{2}\right) n^{-(1-2b)}(n^2-1)^{1/2} e^{2T_l} \tag{2.11}$$

where

$$T_l = \left(l+\frac{1}{2}\right)(\eta_l - \tanh\eta_l)$$

$$\eta = arccosh\left\{ n\left[1 - \frac{1}{l+\frac{1}{2}}\left(t_p^0 \xi + \frac{n^{1-2b}}{\sqrt{n^2-1}}\right)\right]^{-1}\right\}$$

$$\xi = \left[\frac{1}{2}\left(l+\frac{1}{2}\right)\right]^{1/3}$$

$$b = \{1\ (TM), 0\ (TE)\}$$

The derivation of this expression uses asymptotic expansions of the spherical Bessel and Hankel functions in equation 2.9. Comparison of this expression with exact solution of the characteristic equation (see Appendix A) reveals that there is a significant error for the principle diameters of resonators studied in this work, however this error is primarily in the absolute value of the radiation Q, not in the scaling behavior versus diameter.

Figure 2.2 shows a plot of the whispering-gallery quality factor as a function of microsphere diameter for a wavelength of 850 nm. This data was found for both the TE and TM polarized fundamental modes by direct numerical solution of the characteristic equation (2.9). The graph indicates that the radiation loss is a nearly exponential function of diameter, with a slight difference between both polarizations. The TE polarized mode has a slightly higher radiation Q due to the fact that the mode profile is more confined inside the sphere. This exponential dependence of radiation Q on sphere size means that there is a critical size above which the radiation loss can be neglected, as other loss mechanisms have a slower variation with diameter. For a quality factor near 100 million at a wavelength of 850 nm, this point occurs for a sphere with a diameter of 12 microns. When considering operation in the 1550 nm wavelength band, this point now occurs around a 25 micron diameter. On the other hand, for structures with smaller cavity diameters the radiative quality factor will often dominate the overall quality factor.

Experimentally, the quality factors of high-Q resonators degrade quickly with time, with

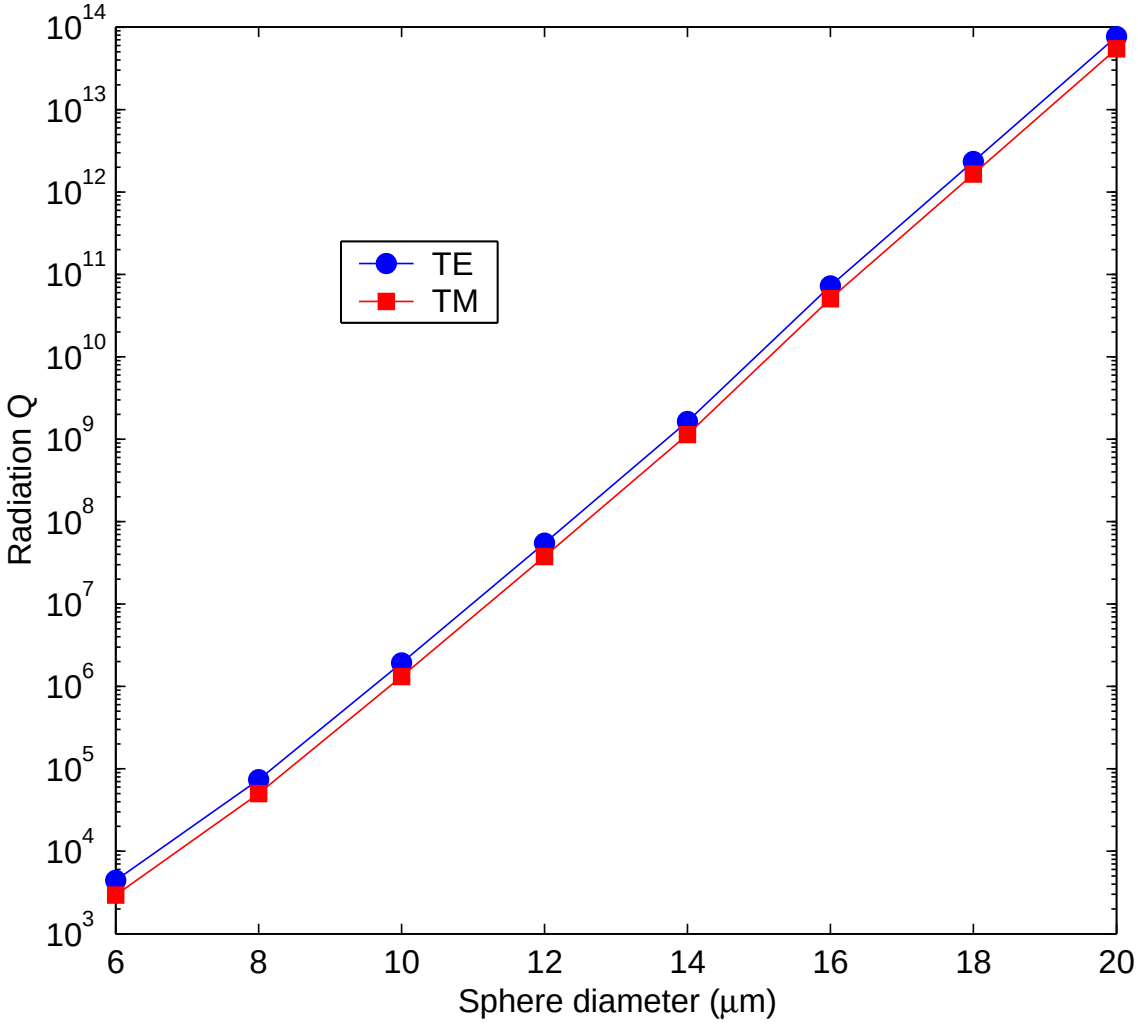

Figure 2.2: Radiation Q as a function of microsphere size for the fundamental TE (blue circles) and TM (red squares) modes at a wavelength near 850 nm. For sphere diameters above 16 microns the overall quality factor will be limited by intrinsic silica absorption and other loss mechanisms.

values falling below 100 million in the space of approximately 12 hours. Not only does this clearly suggest that surface contamination is responsible for the Q degradation, but as this process happens very quickly (and all fabrication and measurements were done in the ambient environment with limited protection from airborne contaminates), the initially measured Q's are limited by contamination as well. Probably the most dominant contaminate is OH and water molecules adsorbed onto the cavity surface [49]. Water absorbs strongly in the infra-red, and readily attaches to the hydrophilic silica surface with a time scale on the order of a couple minutes after initial preparation. While there have been attempts to derive approximate expressions for the water limited quality factor for a spherical cavity [3], these expressions are technically valid only for resonators with diameters much larger than studied in this thesis. Furthermore, these expressions give water-limited quality factors of 10 million, much lower than the values routinely measured in this work (up to 700 million).

Thus, in order to investigate the limiting quality factor for a silica cavity in the presence of water, a simple calculation was performed which determines the effect of a single monolayer of water adsorbed on the cavity surface. This is done by taking the fraction of optical energy which overlaps the water monolayer, combined with the absorption coefficient of water [50], to obtain a water-limited quality factor. Figure 2.3 shows the resulting limiting quality factor for a 60 micron diameter microsphere. In this figure the wavelength dependence of water absorption was used, along with also including the intrinsic silica absorption data [51] (which only affects the overall result for very small wavelengths where water absorption is negligible). The data indicates a minimum Q occurs near 1450 nm, which correspond to a peak in water absorption. Near a wavelength of 1550 nm, the data indicate that a quality factor near 700 million is possible, which matches reasonably well with experimental observations (it is relatively easy to obtain quality factors up to approximately 500 million at 1550 nm, but very hard to realize higher values).

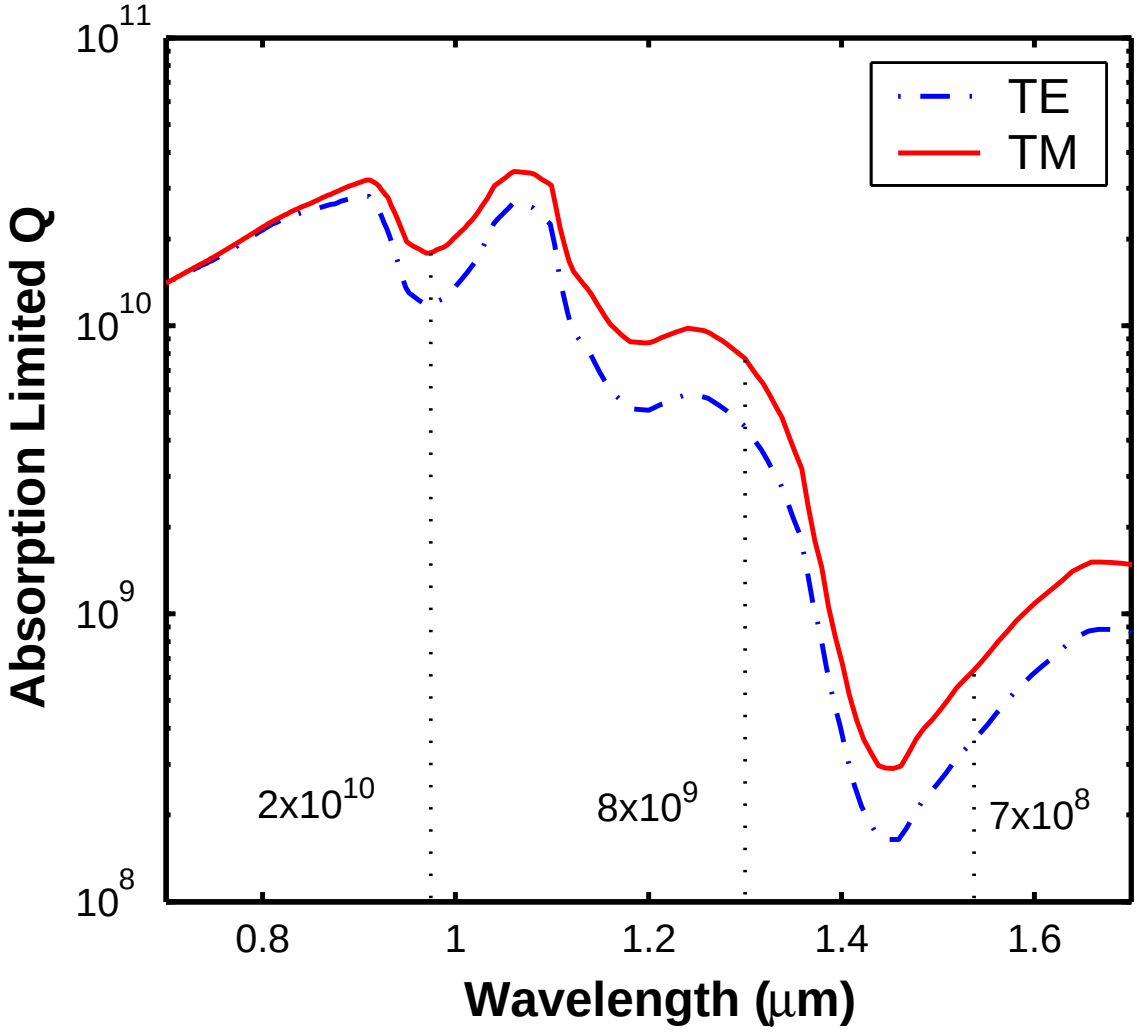

Figure 2.3: Absorption limited quality factor for a 60 micron diameter microsphere assuming a monolayer of water is adsorbed onto the cavity surface. Quality factors as high as 700 million are possible at a wavelength of 1550 nm.

2.2.2.3 Mode volume

The mode volume for a sphere can be determined using formula 2.5 or 2.6 with the modal fields given by equation 2.8. Figure 2.4 shows the calculated mode volume for the fundamental TE and TM polarized modes of a silica microsphere as a function of diameter. The mode volume can be well approximated by

$$V_{m,sphere} \simeq \begin{cases} 1.02 D^{11/6} (\lambda/n)^{7/6} & \text{TE} \\ 1.08 D^{11/6} (\lambda/n)^{7/6} & \text{TM} \end{cases} \tag{2.12}$$

This approximate dependence is given by the solid lines in the figure. The mode volume for the TM polarized mode is slightly higher than the TE modes due to the added external extent of the TM modes.

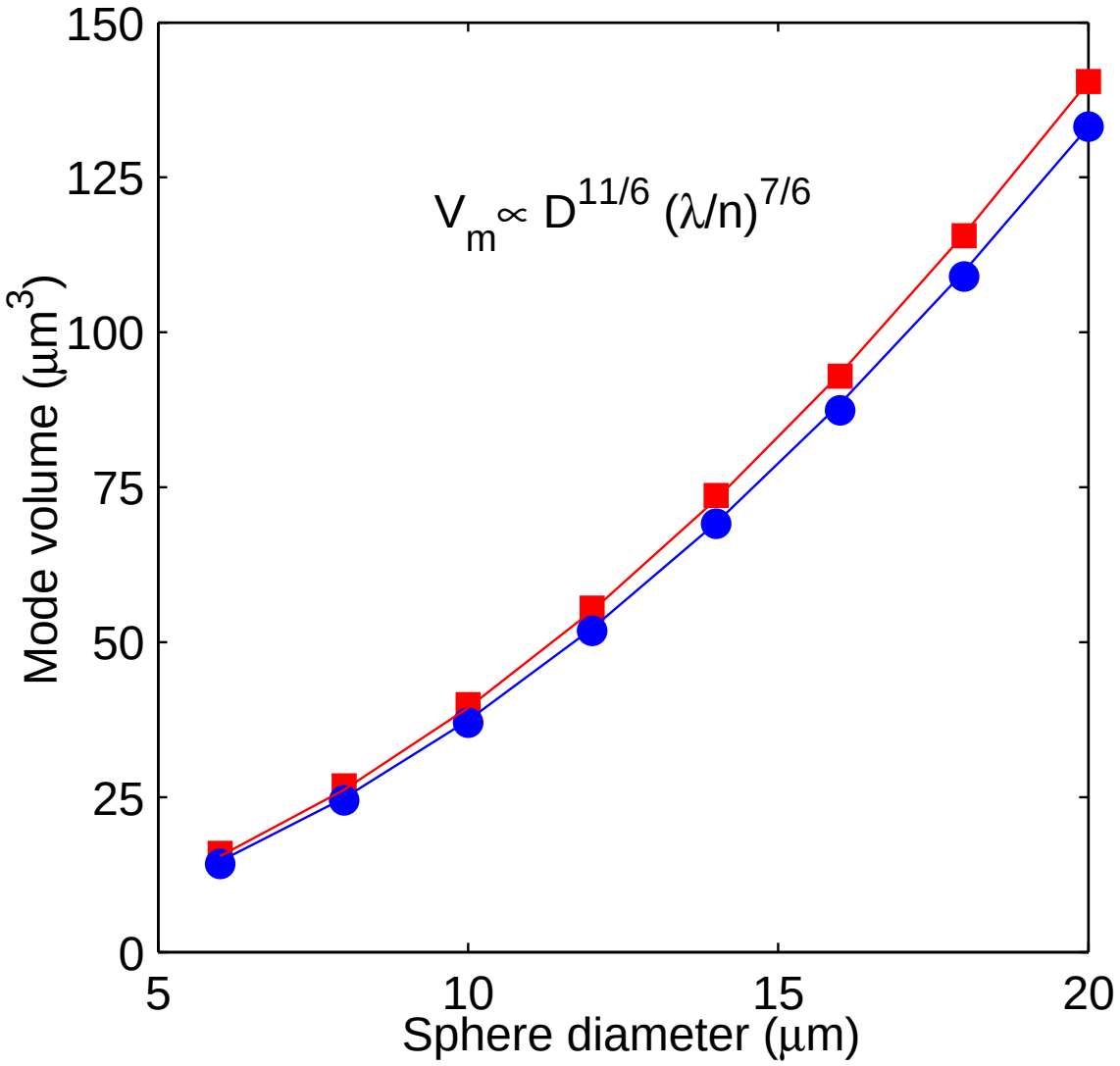

Figure 2.4: Mode volume for a silica microsphere as a function of diameter for a wavelength of 850 nm, for TE (blue circles) and TM (red squares) fundamental modes. The mode volume scales as $V_m \propto D^{11/6}(\lambda/n)^{7/6}$, as indicated by the solid lines.

2.3 Silica microtoroids

It is usually desirable from an experimental and practical standpoint to study planar microcavity designs. Planar microcavities possess the advantages of ease of integration and fabrication parallelism, allowing the accurate control of resonator properties while simultaneously leveraging the existing semiconductor fabrication infrastructure to enable a level of integration with other resonator structures and control structures in a compact footprint [52]. Free-supported microcavities such as silica microspheres arguably allow better experimental flexibility, with improved performance when considering quality factor or finesse. However, these cavities typically require bulky control and manipulation structures, effectively negating any advantage in terms of their physical footprint. Additionally, this severe size penalty detracts from any practical use of these structures.

Thus, a new fabrication method that combines the integrability and control of planar microcavity structures with the performance of freely supported ultra-high-Q silica microspheres was developed. Insights on the necessary modifications to enable ultra-high-Q planar structures can be obtained by investigating the individual contributions to the intrinsic Q of a cavity (as illuminated in section 2.1). For a silica-based cavity, the intrinsic material absorption loss is low enough that the material loss limited Q is on the order of 10^{11} [49]. Surface contaminant absorption (primarily by hydroxyl groups) limits the Q to around the mid 10^8 range for a monolayer adsorbed on the surface at a wavelength of 1550 nm. We can thus eliminate both these degradation mechanisms as being responsible for the low Q in planar structures by noting that silica microspheres possess identical mechanisms while still possessing ultra-high-Q. Furthermore, whispering-gallery-loss only plays a dominate role when the physical size is small, around a 25 micron diameter for 1.5 μm wavelengths. This leaves material inhomogeneities and surface scattering as possible limiting mechanisms. In particular, surface scattering due to the lithographic and etching processes appear to be the dominant mechanism limiting the cavity quality factor.

A significant drawback of ultra-high-Q cavities such as microspheres and microdroplets is the inability to easily integrate other functions in a compact space, such as additional resonators and waveguiding structures. The holders and droplet generators typically occupy a volume much larger than the cavity itself, negating the benefits of compact size. The ability to

integrate high-Q cavities onto microchips is a step forward to the ultimate promise of high-Q microcavites, such as dense integration with other structures.

2.3.1 Fabrication

Initial demonstrations of high-Q chip-based resonators was obtained using standard semiconductor processing techniques, followed by a laser-reflow process [53], as outlined in reference [25] (figure 2.5). In brief, conventional optical lithography was used to pattern disk-shaped pads of thermally grown silicon oxide on a silicon substrate. Then, xenon diflouride gas was used to selectively etch the silicon isotropically, leaving silica disks suspended on silicon pillars[3] [54]. In order to obtain ultra-high quality factors, typically denoted as 100 million and above, both the surface quality and optical homogeneity must be good. Borrowing from the fabrication process of silica microspheres, CO_2 laser irradiation is used to selectively heat and reflow the patterned silica. The combination of thermal isolation of the initial preform periphery and thermal heat sinking of the preform interior through the strong heat conduction of the silicon support pillar results in a preferential melting of the preform along the disk periphery under laser irradiation. Surface tension then induces a collapse of the silica disk, resulting in a toroidally-shaped boundary, with the final geometry controlled by a combination of irradiation flux and exposure time. Importantly, as the optical mode resides in the extremely uniform reflowed periphery of the structure, the quality factors of optical whispering-gallery modes can be very large, with experimental values typically 100 million or above. Figure 2.6 shows a scanning electron micrograph of a typical toroidal microcavity[4]. Our group has currently measured quality factors as high as 500 million at a wavelength of 1550 nm (corresponding to a photon lifetime of approximately 400 ns), close to the highest quality factors of silica microspheres fabricated in our laboratory.

[3]Incidentally, these structures can possess quality factors exceeding 3 million.

[4]I want to briefly mention that Ilchenko has developed a variation on a spherical cavity which they call a microtorus [55]. However, the geometry of the toroidal resonators discussed in this thesis are much closer to an actual torus.

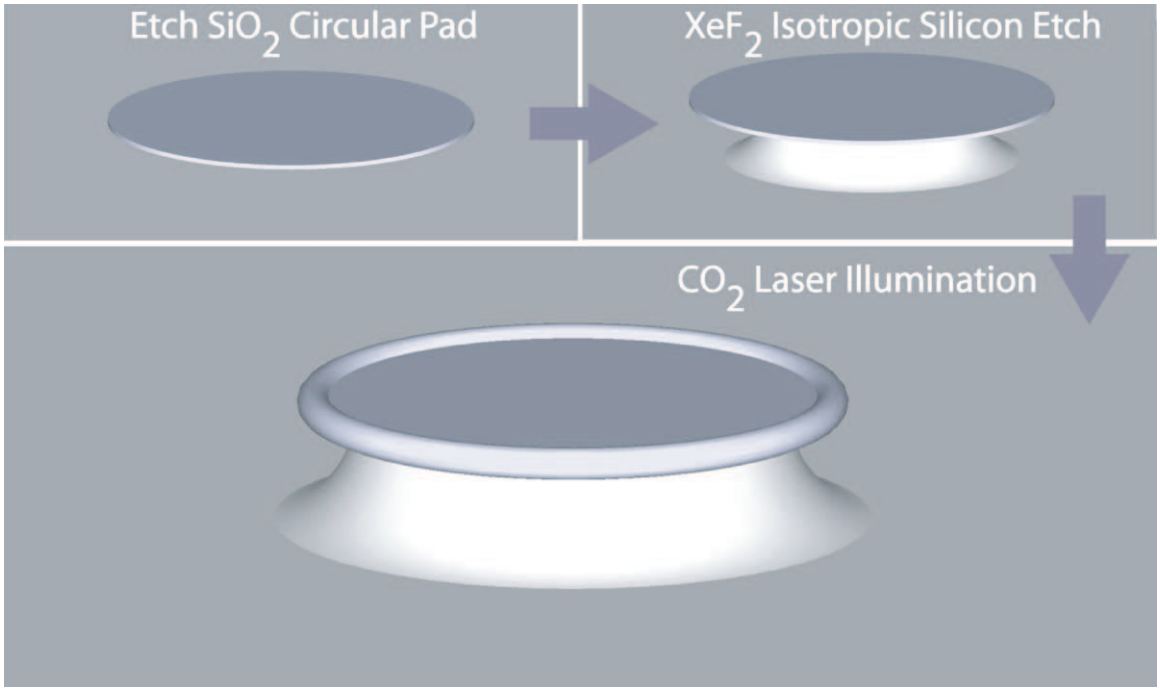

Figure 2.5: Process flow for the fabrication of a toroidal microresonator. After creating a silica circular disk on a silicon substrate by photolithography and wet-etching, an isotropic XeF_2 etch was used to undercut the silica pads, leaving silica disks suspended on a silicon pillar. A CO_2 laser reflow process is then used to create the final ultra-high-Q toroidal structure.

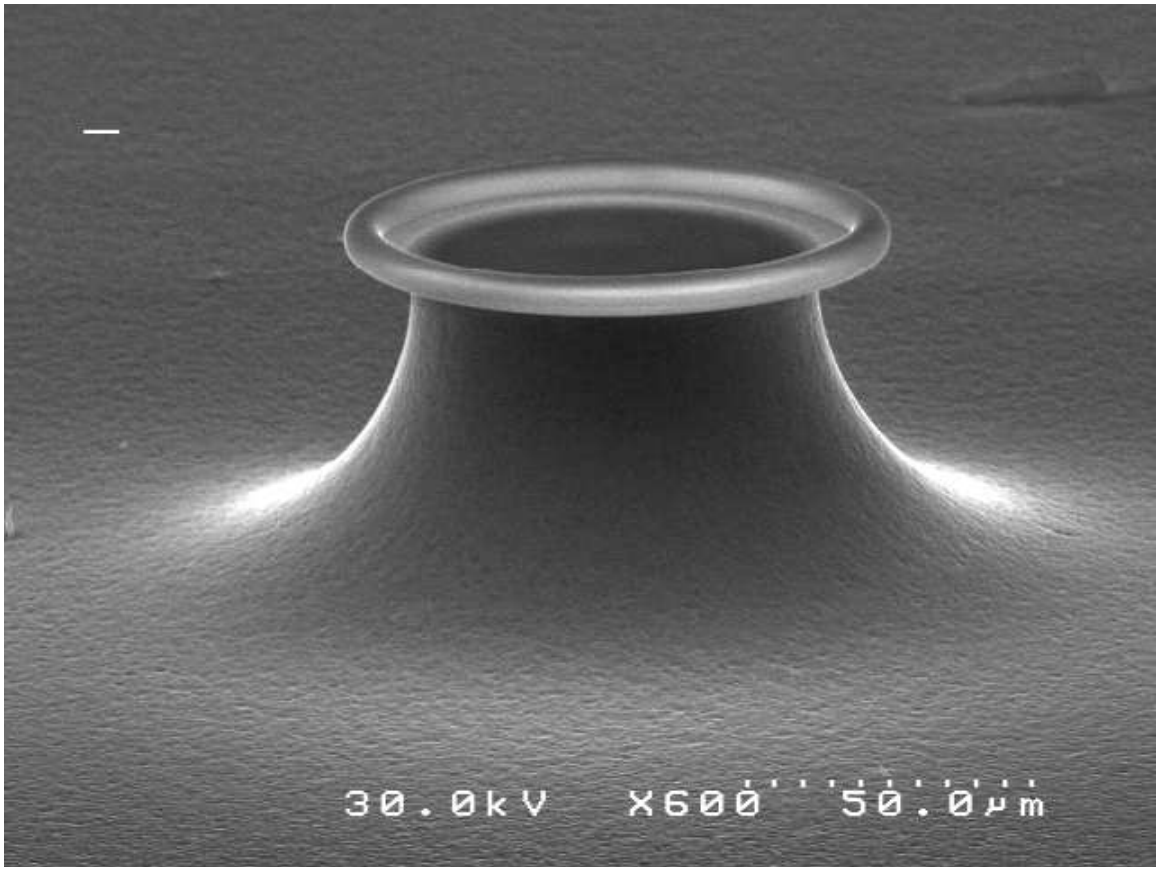

Figure 2.6: Scanning electron micrograph of an ultra-high-Q toroidal microcavity.

2.3.2 Optical properties

The optical modes of a toroidal dielectric cavity are not analytically solvable, as Helmholtz's equation is not separable in this coordinate system. However, the ability to predict the optical properties, especially the resonance wavelengths, mode volumes, and radiation quality factors, is very important in understanding the utility and applicability of these structures to both passive and active optical studies. The microtoroid geometry, which exhibits a dumbbell-shaped cross section, can in most cases be considered a torus (expressed in terms of the principle diameter D, and the minor or inner diameter d). The presence of the supporting structure only affects the optical mode when the toroid diameter becomes comparable to the radial extent of the optical mode which occurs at an inner diameter below approximately 1.5 microns for an optical mode with a wavelength of 850 nm, and approximately 2.8 microns for at a wavelength of 1550 nm. Furthermore, through improvements in fabrication the influence of the toroid support can in principle be minimized. While approximate expressions for the optical behavior of these structures for both the low compression (sphere-like) and high compression (step index fiber-like) regimes can be derived, operation in the intermediate geometrical regime is desired, as these are both experimentally accessible and retain the most desirable properties of whispering-gallery-type microcavities. Therefore, I developed a numerical approach to characterize the optical modes of the cavity over the complete geometrical range possible, using a two-dimensional finite element eigenmode/eigenvalue solver, after explicitly accounting for the rotational symmetry, as described in more detail in Appendix A. The optical modes are calculated in a full-vectorial model, which provides the complete electric field dependence. The accuracy of the numerical technique was carefully verified by comparison with the solution for a microsphere cavity. The results for the mode volumes, resonance wavelengths, and field profiles were in excellent agreement. Furthermore, the error in the radiation quality factor was less than 10% over a wide value of radiation Q's (10^3 to 10^{14}), demonstrating that this method can give the accuracy required to investigate the fundamental radiation loss limits in the cavity geometries of interest in this thesis.

2.3.2.1 Resonance locations

In a toroidally-shaped cavity, the added dielectric confinement results in a shift of the resonance to higher frequencies (lower wavelengths) for a given m number. Figure 2.7 shows the resonance wavelength for a fundamental mode in a 30 micron principle diameter toroidal cavity as the inner diameter is reduced, for m=81 and a refractive index n=1.45. The data are shown for both TE and TM polarized modes. There is an initially slow reduction of wavelength when the deviation from a spherical cavity is small, as shown in the figure inset. Upon further reduction of the toroidal inner diameter, the mode approaches that of a step-index fiber and the resonance wavelength is strongly dependent on the inner diameter.

One of the main drawbacks for spherical cavities is that the azimuthal m modes are degenerate in frequency. In practice, the slight residual eccentricity means that these modes are slightly split, with analysis showing frequency shifts on the order of 10 GHz [17]. As this shift is much smaller than the FSR of these cavities, this creates a problem when considering practical applications of these structures (i.e., multiline lasing and cross-talk). However, the breaking of the spherical symmetry in a toroidal cavity suggests that these azimuthal modes are no longer degenerate. To investigate this, the wavelength separation between the fundamental and first order azimuthal modes was determined as a function of inner diameter for a principle diameter of 30 microns at a resonance wavelength near 1550 nm. Figure 2.8 shows the calculated wavelength separation. We see that the wavelength separates very quickly, indicating that this very beneficial degeneracy lifting occurs even for modest deviations from a microsphere. For comparison, the FSR of the cavity is also indicated. Only the first higher-order mode is calculated, however the geometrical effect will be much stronger for the still higher-order modes, leading to an even faster degeneracy lifting.

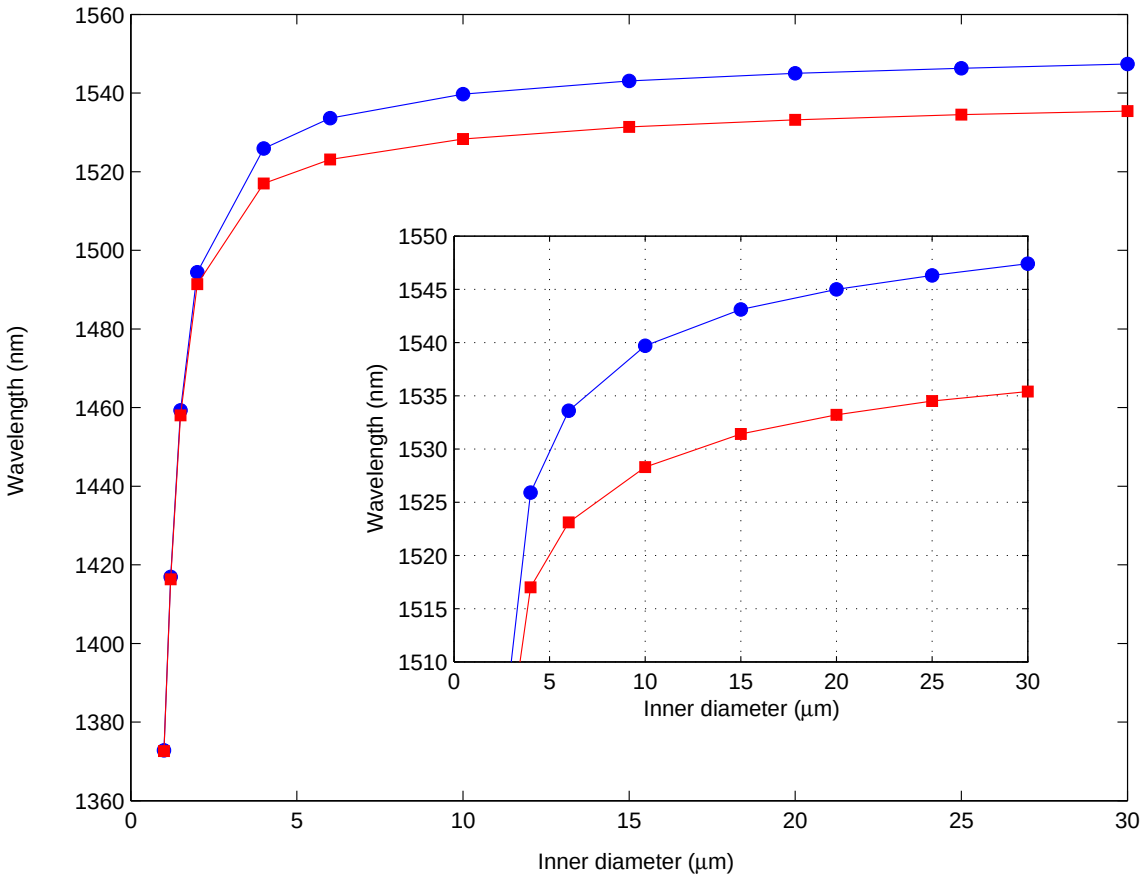

Figure 2.7: Resonance wavelength for TE (blue circles) and TM (red squares) as a function of inner diameter for a toroid with a principle diameter of 30 microns. The data show a slow decrease of resonance wavelength for large inner diameters, as illustrated by the expanded view in the inset. Upon significant compression of the mode the resonance wavelength decreases dramatically.

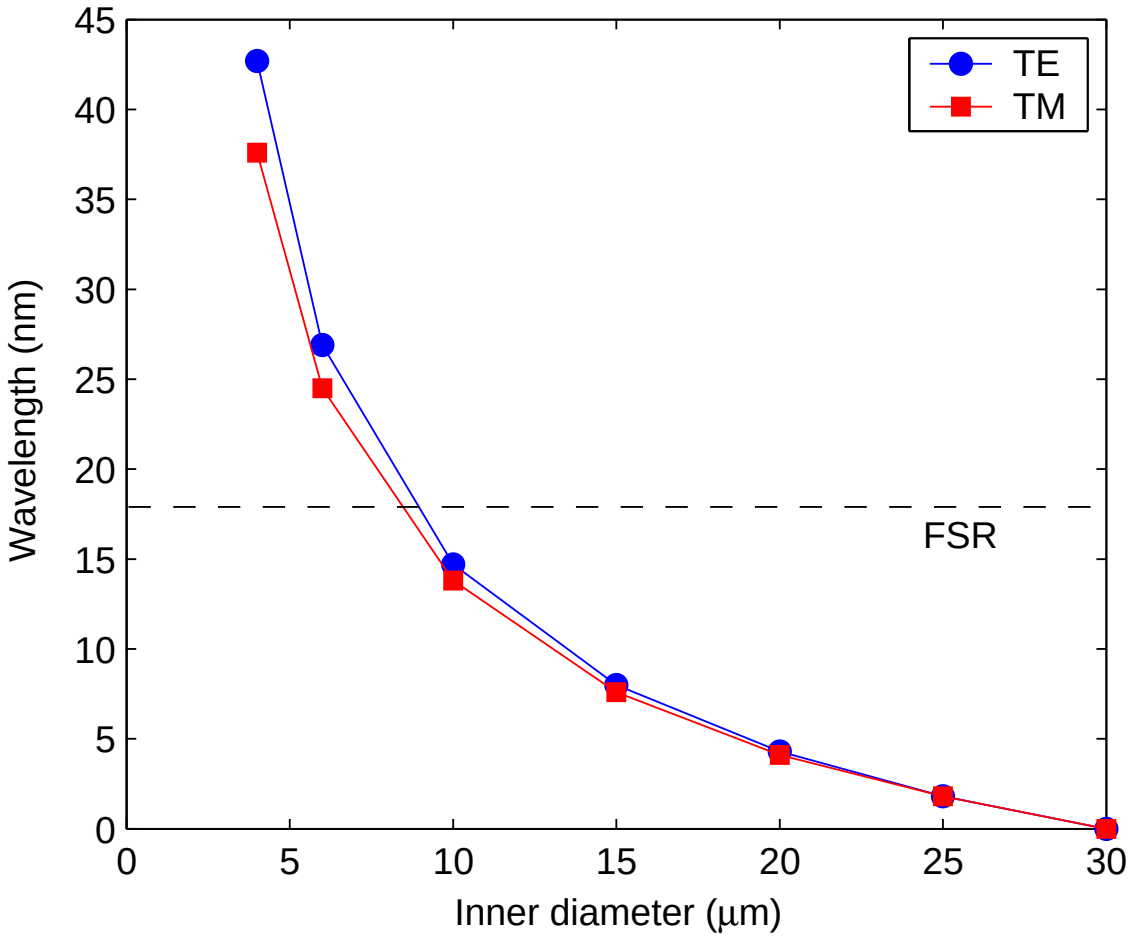

Figure 2.8: Wavelength separation between the fundamental and first higher-order azimuthal mode as a function of inner diameter for a toroid with a principle diameter of 30 microns.

2.3.2.2 Quality factor

The additional dielectric confinement in a toroidal cavity not only shifts the resonance location, but also increases the radiation loss of the structure. Intuitively, this arises from the fact that the optical mode becomes more extended into the external environment, allowing a larger fraction of power to extend beyond the radiation caustic[5], and is subsequently lost. In more precise terms, as the toroid inner diameter is reduced, the mode l number is also reduced, which causes the radiation caustic to be located closer to the cavity surface (the radiation caustic is located at a radius of $R_c = l\lambda/(2\pi)$ for an external index of unity). For a toroid in the sphere-like geometry regime, a simple analogy is that the radiation loss will scale approximately as that of a spherical cavity with the same l number. However, in the highly compressed step-index fiber-like regime, the optical mode is quite different and the radiation loss is expected to increase much more rapidly. This is also supported by the fact that for highly-confined toroids the radiation caustic can be located either at or inside the cavity principle diameter. Using the approximation for a spherical cavity (equation 2.11) in this regime results in a quality factor that is far too large.

The numerical finite-element method was used to determine the effects of geometrical confinement on the radiative quality factor. Figure 2.9 shows a calculated radiative quality as a function of inner diameter for a silica toroid with a principle diameter of 20 microns, corresponding to the fundamental TE and TM modes at a wavelength of 850 nm. The data indicate that there is indeed an initial slow reduction of the quality factor when the optical mode retains whispering-gallery behavior, with a scaling in qualitative agreement with that predicted from the spherical cavity analogy. However, when the optical mode transitions into a step-index fiber-like mode (for inner diameters below approximately 1 micron) the drop-off of the radiative Q is much more dramatic, with decreases over an order of magnitude for a change of inner diameter of just 50 nm. Furthermore, the initial difference in radiative quality factor for TE and TM polarizations vanish.

[5]The radiation caustic for a circularly symmetric cavity is the point at which the optical phase velocity of the guided mode (which scales as l/r) exceeds the speed of light in the external medium. At this point the mode cannot be bound and thus radiates.

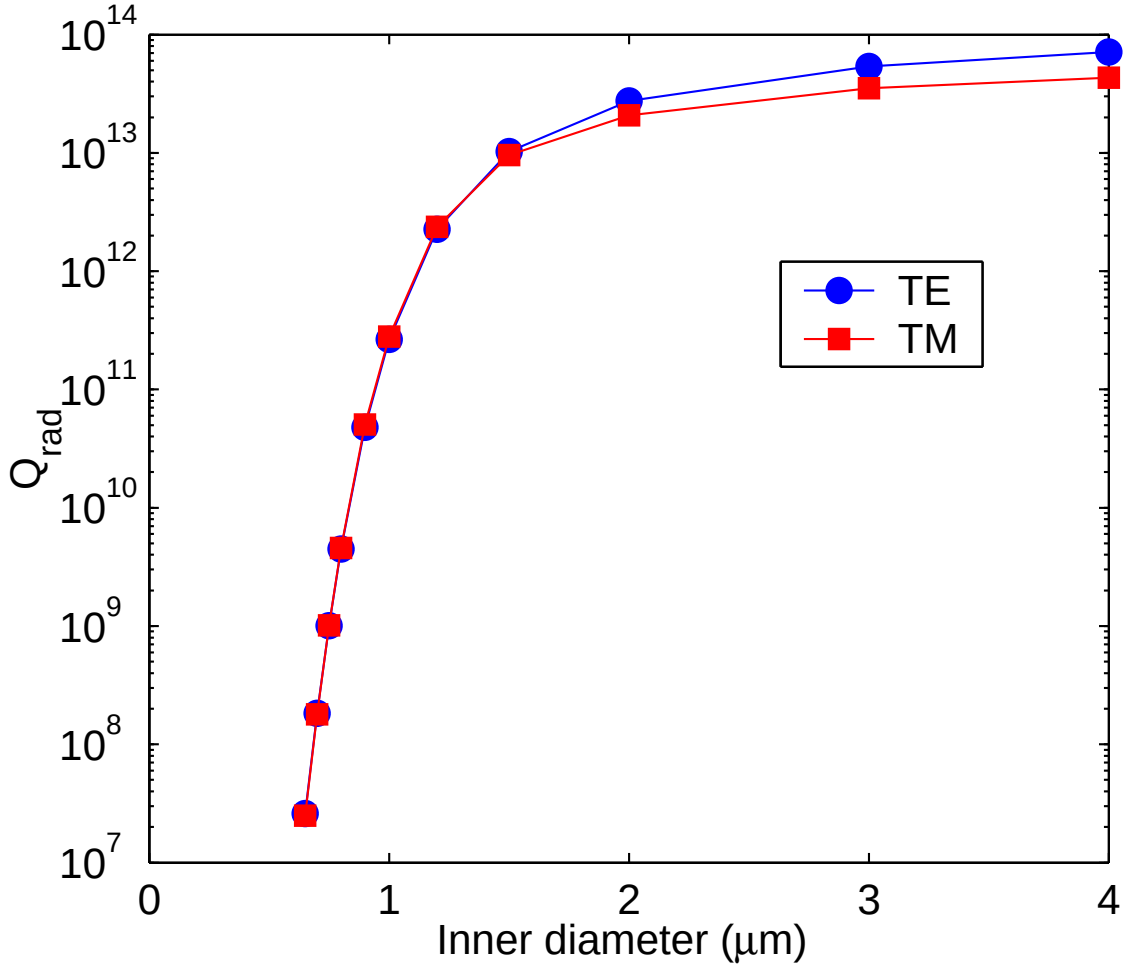

Figure 2.9: Calculated radiation loss for a toriodal microcavity as a function of inner diameter, for a principle diameter of 20 micron. Both TM (red squares) and TE (blue circles) polarizations are shown. The data show that there is a slow reduction of Q as the optical mode is compressed while the mode acts primarily as a whispering-gallery-type mode. However, as the geometrical confinement increases to such a point where the optical mode approaches that of a step-index fiber, there is a much stronger reduction of quality factor.

2.3.2.3 Mode volume

The presence of stronger vertical/azimuthal dielectric confinement in a toroid structure can profoundly modify the optical mode volume. Figure 2.10 shows the calculated modal volume for a fundamental cavity mode in a 50 micron principle diameter structure as the inner (minor) diameter is reduced. In this graph the wavelength was fixed near 1550 nm, for both TE and TM polarizations. The data indicates that there is a uniform reduction of modal volume as the toroidal inner diameter is reduced. There is an initial slow reduction, primarily from compression in the vertical direction, which arises from the increased local dielectric curvature at the cavity equator. However, once the inner diameter is reduced such that the optical mode is additionally confined in the radial direction, the optical mode transitions to that of a step-index optical fiber. This results in a much faster reduction of modal volume, as indicated for inner diameters below approximately 4 microns. In this high compression regime, both TE and TM polarized toroidal modes converge to near identical modal volumes, which is a result of the fact that in a step-index fiber both cavity modes are analogous to the HE_{11} fiber mode. The data show that an overall modal volume reduction of a factor of seven is possible for this particular principle diameter.

When considering the suitability and performance of toroidal cavities, it turns out that often the most significant factor is that the modal volume is reduced over that of a spherical cavity. This results from the fact that the actual radiation loss limit of these structures is rarely approached, even for spherical cavities (provided larger sizes are used, above approx. 25 microns at 1550 nm), which is true for most of the experiments in this thesis. Thus, a tremendous advantage is to have an approximate model for the functional dependence of the optical mode volume in a toroidal cavity, negating the need for time-consuming modeling.

As mentioned above, depending on the ratio of the toroidal principle and inner diameters, the cavity appears either “sphere-like” or “step-index fiber-like.” So to first order, the mode volume is expected to be similar to that of a sphere with diameter (D) for large inner diameters, and close to the mode volume of a step-index fiber of diameter (d) wrapped around into a circle of diameter D. However, a better approximation for the sphere-like regime can be obtained by noting that the optical modes of a sphere can be approximated as a two-dimensional harmonic oscillator in the radial and azimuthal (vertical) directions. Upon reduction of the

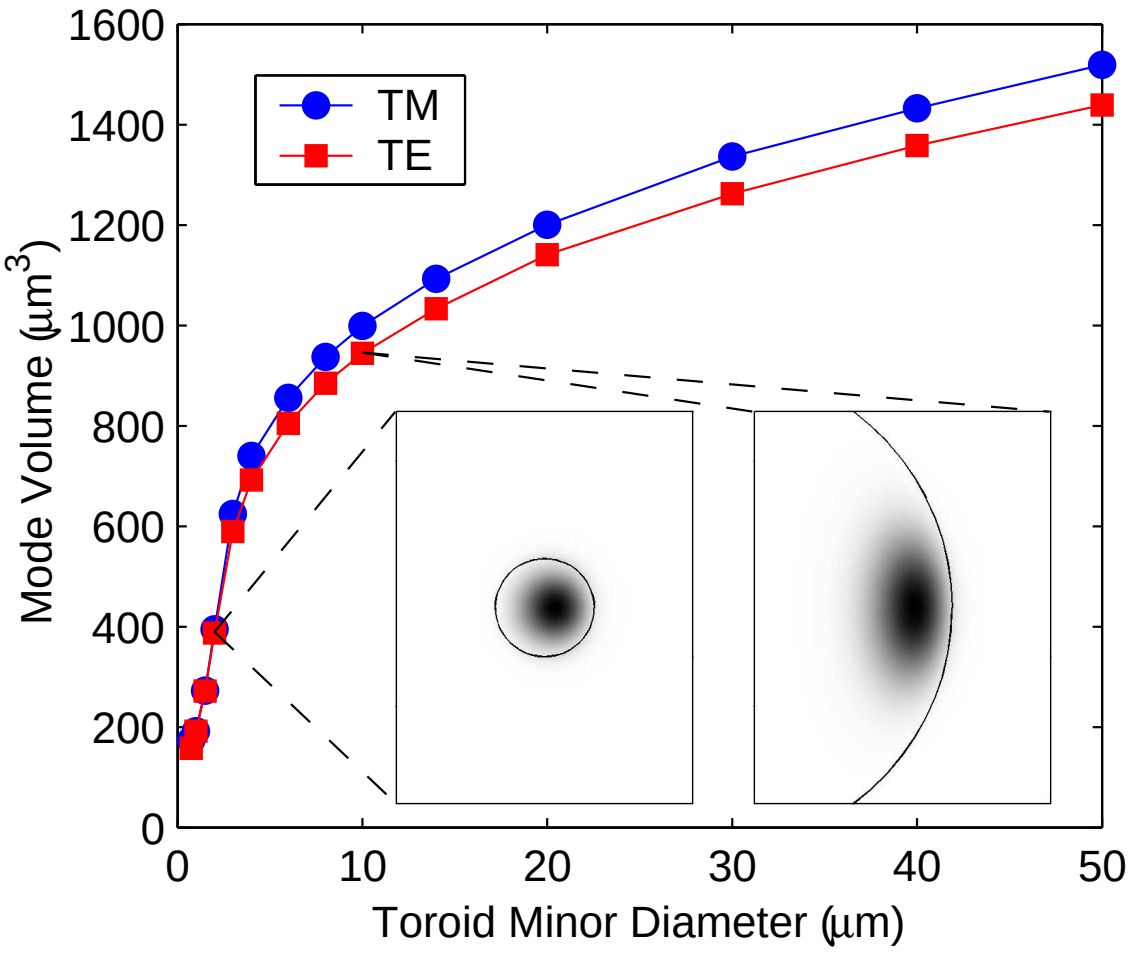

Figure 2.10: Calculated modal volume for a 50 micron principle diameter toroid as a function of inner diameter. The data shows the fundamental mode (both TE and TM polarizations) for a resonance wavelength near 1550 nm. Inset shows the respective electric field profiles.

inner diameter, the optical mode is only compressed in the azimuthal direction, thus suggesting the total mode volume scales in a similar way. This results in a simple formula for the sphere-like regime as given by $(d/D)^{1/4}V_m^{sphere}$. Figure 2.11 shows the calculated TM polarized mode volume from figure 2.10, along with the calculated mode volume for a wrapped step-index fiber and the sphere-like regime using the simple expression just presented. The data indicate that both approximations give good agreement in their respective regimes of validity[6]. However, in practice often the most suitable geometry (both from a fabrication standpoint and performance perspective) lies in the intermediate regime, where both expressions have a large error (around 20% by inspection of the figure). Improved agreement can thus be obtained by using the empirical equation,

$$V_m^{toroid}(d,D) \simeq \left[\left(\pi D A_m^{fiber}(d)\right)^{-3} + \left((\frac{d}{D})^{1/4} V_m^{sphere}(D)\right)^{-3}\right]^{-1/3} \tag{2.13}$$

where $A_m^{fiber}(d)$ represents the mode area of a step-index fiber with diameter d. This expression preserves the asymptotic behavior at both geometrical extremes and provides excellent agreement in the intermediate regime (given by the black line in figure 2.11 and inset). Over the entire range a mode volume error less than 4% was obtained. This formula also was verified to give excellent agreement for both TM and TE polarized modes and for principle diameters lower than 50 microns. Likely the agreement extends for larger principle diameters as well, but this formula was only verified for a principle diameter up to 50 microns, which was sufficient for the experiments in this thesis.

[6]There is an interesting consequence to being able to describe both the low and high compression regimes by simple scaling laws when considering the maximum amount of compression possible in a toroidal cavity. As the mode volume for a sphere scales nearly quadratically (section 2.2.2.3) with diameter and the volume for a wrapped fiber linearly, the compression ratio scales linearly with principle diameter D. This means that larger principle diameter cavities can have dramatic mode volume enhancements over microspheres.

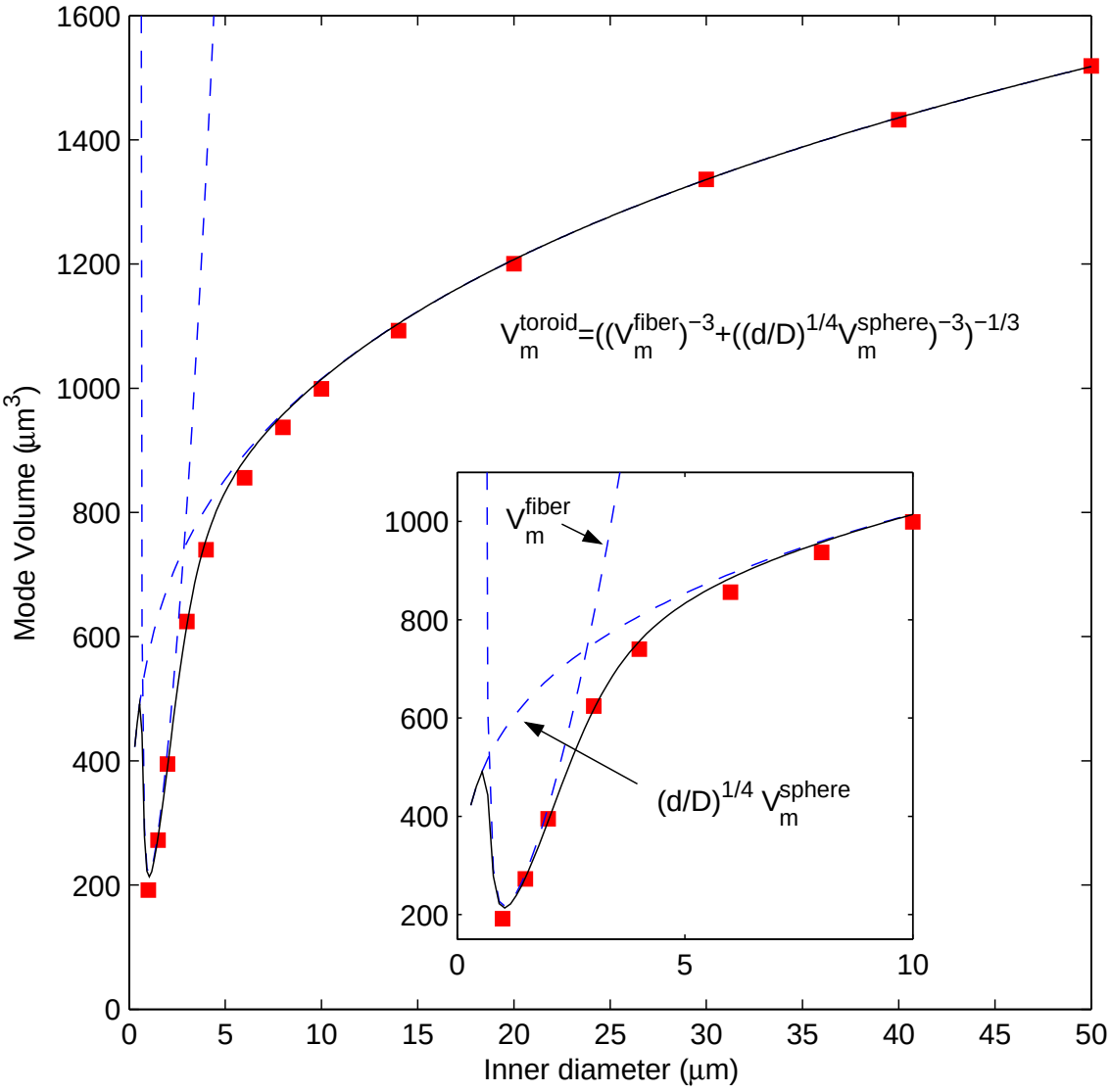

Figure 2.11: Comparison of the approximate mode volume formula for a toroid with the numerical calculation (black line). Both the asymptotic sphere-like and fiber-like behavior is shown with dotted lines. Excellent agreement is observed for all inner diameters (error $< 4\%$).

Chapter 3

Optical coupling of microcavities

The study of the optical properties of ultra-high-Q (UHQ) microcavities requires the ability to optically excite and probe the resonator. Furthermore, the investigation of the full potential of UHQ structures to realize high performance devices, such as low-loss passive elements and low-threshold active elements such as nonlinear sources, requires an ability to both efficiently excite the modes of the cavity and to efficiently extract optical energy from the cavity. There are several commonly used techniques to couple optical microcavities. These fall into two classes: phase-matched and non-phase-matched techniques. Of the two, phase-matched schemes offer a dramatic advantage in terms of coupling efficiency both into and out-of the cavity, relegating non-phase-matched[1] schemes (of which free-space illumination is the sole member) to systems where experimental limitations and/or simplicity is coupled with a sufficient excitation power and detection margin such that the gross inefficiency is tolerable. Additionally, precise characterization of the properties of optical microcavities is extremely difficult for broad illumination schemes, as multiple whispering gallery modes (WGM's) are excited spatially, and the emission is detected in a radial fan of energy from the perimeter. For these reasons, phase-matched couplers are commonly used.

Phase-matched coupling techniques can again be subdivided into two areas, direct and evanescent couplers. Direct couplers, such as grating couplers fabricated on the cavity surface [56], possess the advantage of free-space illumination/emission simplicity along with the ability

[1]Non-phase-matched techniques do not have the ability to have the excitation wave and the confined wave in the resonator to have the same phase-velocities. This means that there is an effective walk-off of the excitation and cavity waves over the interaction region, lowering the amount of coupling. This phase-velocity is given by the effective modal index of the optical mode, which in the case of free-space illumination is the refractive index of the external medium (commonly near unity for UHQ structures), whereas the resonator mode modal index is between the refractive index of the core and external medium (and usually very near the core index). Thus by necessity any guided wave cannot be phase-matched to a free-space beam.

to phase-match, thus in principle allowing high efficiency. However, as the effect of this coupling method on the intrinsic cavity properties is unclear, I will focus on evanescent coupling methods, which are quite mature in the literature.

3.1 Evanescent coupling techniques for optical micro-cavities

3.1.1 Prisms

Up until about the mid-90's, prism coupling was the sole technique used to phase-match UHQ microspheres. Prism coupling consists of a laser beam which undergoes total internal reflection in a prism, such that the external evanescent field of the beam at the reflection region overlaps the whispering-gallery-mode field of the optical resonator (Figure 3.1). This method is inherently flexible, allowing phase-matching by changing the incident angle of the input beam (as long as the angle still satisfies the total internal reflection condition), and observation of optical energy which has interacted with the resonator at the prism output. It is possible both to excite individual resonances and to observe them through a spatially resolved output spectrum [17]. While this method is well-proven and flexible, it has a couple drawbacks. First, the coupler is bulky, which while somewhat desirable from a stability standpoint (intrinsic fluctuation of the coupler can have a profound effect on the coupling properties of fiber-tapers), negates most of the practical advantages of micron-scale devices[2]. Furthermore, integration with chip-based cavities is, while possible, relatively difficult.

From a performance side, however, prisms have a relatively severe drawback as opposed to newer coupling designs: a low degree of coupling ideality and spatial mode matching. The precise definition of coupling ideality will be discussed in section 3.3.1, however, in simplistic terms, what happens is that the optical energy in the cavity radiates in a cone centered around the optimal phase-matching angle (which is determined by the mode of interest) [58, 59]. This cone thus contains a spread of modes with slightly different k-vectors. The consequence of

[2]I must note that there is a variation on this theme which uses angle-polished optical fibers. This method, developed by Ilchenko et al. at JPL, looks for all purposes as a prism coupler, with the added advantage of fiber-compatibility [57]. While addressing much of the drawbacks of prism coupling, the performance of this scheme, to the level of detail of tapered-fiber couplers as shown in this thesis, has not yet been demonstrated.

this is that although the input beam (to a good degree) and the resonator mode are single mode, the output beam is not. Thus experiments where modal purity of the output energy is desirable are not readily studied using this approach (as manifested by the inability to observe true critical coupling, where all optical energy is coupled into the resonator). Additionally, this fact combined with the limited ability to spatially mode-match the resonator may have played a role in the relatively few experimental observations of nonlinear optical effects in microspheres (besides thermal nonlinear effects), which are easily observable using tapered fiber couplers.

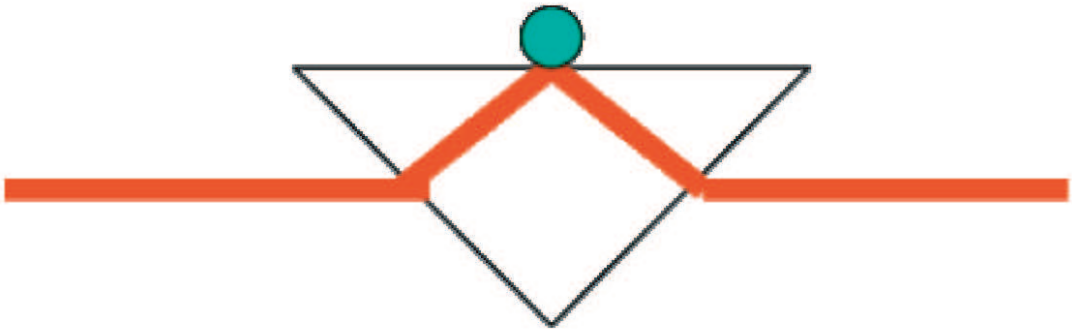

Figure 3.1: Illustration of prism coupling between a free-space beam and an optical microcavity. The optical microcavity is placed in the evanescent field of the optical wave upon total internal reflection at the prism interface. By control of the incident angle efficient excitation can be achieved.

3.1.2 Planar structures

One of the main advantages of planar waveguides is the ready integration with planar lightwave circuitry. Thus the ability to use planar waveguides to couple to UHQ microresonators, such as the chip-based toroidal cavities studied in this thesis, would facilitate integration of these structures with additional functionality. The use of planar waveguide couplers has been around for many years, with the technology mature. Typically, these waveguides are used in a simple rectangular or ridge waveguide configuration. For the most part, these waveguides have only been applied to relatively low Q microresonator structures, mostly as a result of the lack of suitable UHQ cavities. However, some conclusions can be drawn on the potential applicability of these coupling techniques for fully integrated high-Q microcavities.

Firstly, the fabrication of a truly planar waveguide coupler to excite silica-based UHQ structures is not straightforward. All UHQ structures to date are based on silica or silica glass-like structures which possess refractive indices near 1.45. Given this constraint, coupled with the fact that the external index is near unity (to keep the radiation loss sufficiently low for moderate cavity diameters), means that in order to phase-match the resonator, the waveguide needs to be made with a similar material system for a conventional rectangular/ridge waveguide design. This results in difficulty creating a sufficiently low cladding index. One possible solution is to use a small index contrast waveguide, however, spatial mode matching is dramatically lessened. A potential way to overcome this limitation is to use a type of waveguide known as a stripline-pedestal anti-resonant reflecting optical waveguide (SPARROW) [60].

A SPARROW solves the index contrast problem between the waveguide core and substrate by designing a reflecting layer between the core and substrate cladding. This layer is designed as a dielectric Bragg mirror which reflects a large portion of the waveguide fundamental mode. Research using this waveguide system at MIT has shown promise for coupling to UHQ silica microspheres [61], and additionally has demonstrated relatively low waveguide propagation loss. However, the frequency-dependent loss of the Bragg mirror may cause complications when investigating nonlinear optic effects or lasing, where the emitted energy differs in frequency from that of the excitation wave.

A common drawback to all current planar waveguide couplers is a relatively large propagation loss compared with optical fiber. While this loss can be made relatively low, below

1 dB/cm, when studying optical microcavity effects where typically the optical powers are small, any excess loss is detrimental. This is especially true when investigating quantum optic effects, such as optical squeezing, that are critically sensitive to any system loss. Additionally, all lithographically-created structures possess surface roughness which can induce scattering at the waveguide/resonator interface. While this scattering can be neglected for low Q resonators, this loss can dominate for UHQ devices.

3.1.3 Tapered fibers

Optical fiber technology solves many of the problems of previous coupling methods. Optical fibers are extremely low loss (<0.2dB/km at a wavelength of 1550 nm), compact, relatively robust, and a natural transport medium for optical energy. The use of optical fiber for a coupler means that both the incident wave and any wave that interacts with or is generated from a cavity can be manipulated in an all-fiber system using standard components. The advantage of this fact cannot be overstated, as the ease of alignment/integration is readily apparent when comparing the experimental complexity of fiber-based couplers with their non-fiber counterparts. Furthermore, the extremely low loss of this transport medium is ideally suited to potential applications of optical microcavities, in particular the generation and transport of quantum states of light [34].

There are a number of types of fiber-couplers, including side-polished and half-block couplers [18], in addition to the angle-polished fiber tip mentioned briefly in section 3.1.1. The side-polished and half-block couplers, while fiber-based, possess relatively low efficiencies for coupling both into and out of a resonator, in addition to a high optical loss for energy which does not interact with the cavity. However, another type of fiber-coupler, the tapered optical fiber [19], can retain the ultra-low loss inherent to optical fiber while possessing very high coupling efficiencies to an optical microresonator.

3.1.3.1 Fabrication

Tapered optical fiber consists of a standard optical fiber with a region reduced in size such that the optical field in the fiber now extends into the external environment, where it can interact with, in this work, an optical microresonator. While this tapering process can be

done many ways (such as etching a section of fiber in HF acid), this work focuses on using flame-drawn tapers, where a section of fiber is heated with a hydrogen flame and drawn apart until the waist is a narrow thread approximately 1 to 3 microns in diameter (figure 3.2), with the diameter chosen in order to optimally couple to a microresonator as discussed in section 3.2.2. By proper control of the heating and stretching profiles, such that the adiabatic tapering condition [62] is satisfied[3], the loss of the fiber can in principle be made arbitrarily low, with values below 0.1 dB (2%) commonly realized in the process of this work. The final structures typically consist of a tapered region approximately 1 to 2 inches in length, with the core of the initial optical fiber disappearing and the taper becoming effectively a dielectric cylinder with optical energy guided by the cladding/air interface. The fact that there is now a large dielectric step between core and cladding (in contrast to the weak confinement of single-mode fiber) has profound implications on the modal behavior of these structures, as will be discussed below.

[3]The adiabatic condition states that the rate of change of the fiber properties is sufficiently slow that there is no coupling to higher-order fiber modes or scattering into radiation modes, which in practice means that the rate of tapering of the fiber size must be slower than the propagation constant of the fundamental fiber mode.

a.

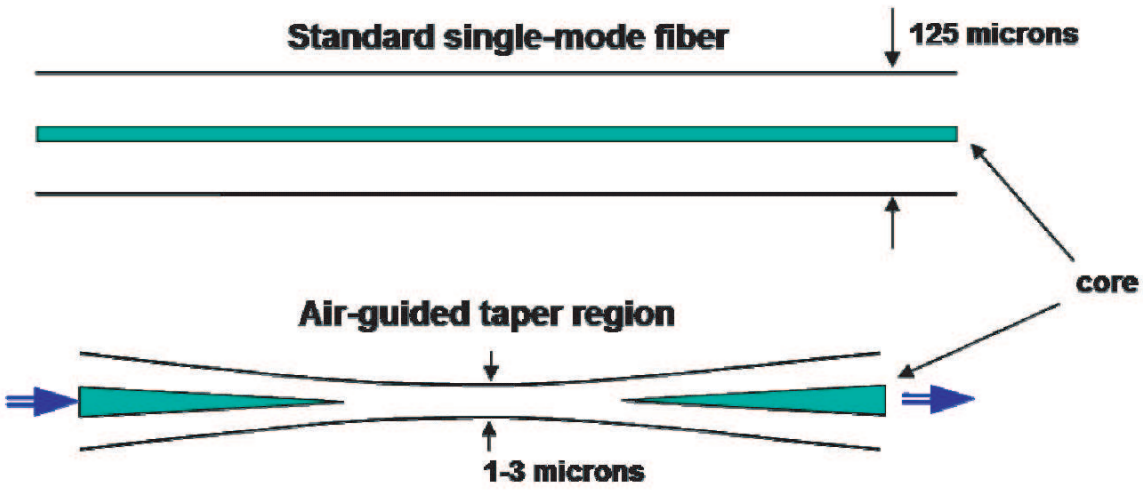

b.

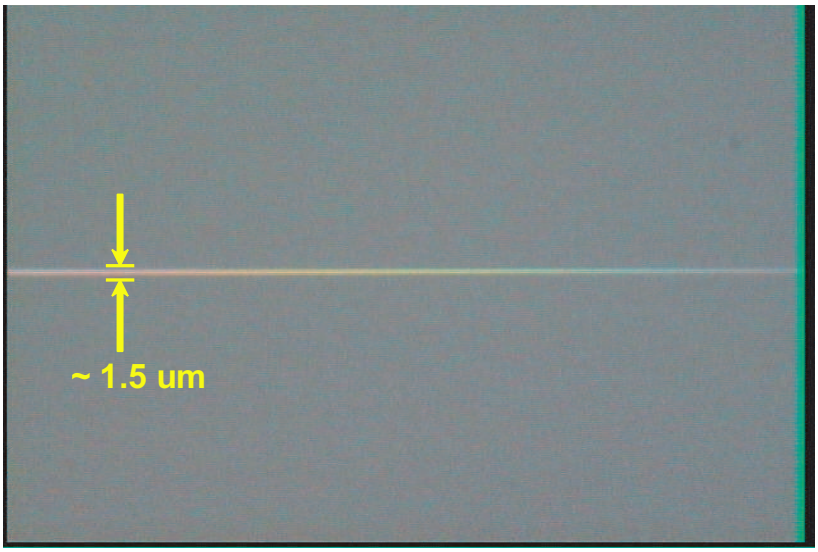

Figure 3.2: Fabrication of a tapered optical fiber. An illustration of the before and after process is shown in a, with an optical micrograph of the tapered region shown in b. The coloring is due to the optical filtering effect of a thin dielectric cylinder on the incident white light source.

3.1.3.2 Modal properties

As a tapered optical fiber consists of a circularly symmetric shape composed primarily from the fiber cladding of the untapered optical fiber (only 0.4% of the taper consists of the core material in a typical SMF at 1550 nm wavelengths), it can be treated as a simple step-index fiber with a refractive index difference of ∼0.45. Furthermore, even though the taper is nonuniform along the fiber length, the interaction with an optical resonator occurs only over a region of ∼5 to 10 microns, where it is uniform. Thus, when considering the interaction between the taper and an optical microresonator, the taper may be thought of as a dielectric rod of constant diameter with a step index profile. The large index difference suggests that this local taper environment does not necessarily retain the single-mode character of the initial fiber (whose optical modes can be expressed as linearly polarized LP modes), and the optical fields must now be accounted for by using the exact relations for a step-index fiber.

The optical modes of a step-index cylindrical fiber, described by a core radius a, core refractive index n_{core}, and cladding index n_{clad}, are well known, with the z components of the electric and magnetic fields given in cylindrical coordinates by the expressions [63]:

$$\begin{aligned}
E_z(r,\phi,z) &= J_l(hr)\cdot exp(i(\omega t + l\phi - \beta z)) && \text{inside core } (r<a)\\
E_z(r,\phi,z) &= J_l(ha)\cdot K_l(qr)/K_l(qa)\cdot exp(i(\omega t + l\phi - \beta z)) && \text{outside core } (r>a)\\
H_z(r,\phi,z) &= B\cdot J_l(hr)\cdot exp(i(\omega t + l\phi - \beta z)) && \text{inside core } (r<a)\\
H_z(r,\phi,z) &= B\cdot J_l(ha)\cdot K_l(qr)/K_l(qa)\cdot exp(i(\omega t + l\phi - \beta z)) && \text{outside core } (r>a)
\end{aligned} \tag{3.1}$$

where

$$B = \frac{i\beta l}{(\omega\mu)}\left((qa)^{-2}+(ha)^{-2}\right)\left(\frac{J_l'(ha)}{haJ_l(ha)}+\frac{K_l'(qa)}{qaK_l(qa)}\right)^{-1}$$

$$q^2 = \beta^2 - n_{clad}^2 k^2$$

$$h^2 = n_{core}^2 k^2 - \beta^2$$

The modes are described by a set of three quantum numbers (l,m,p), where l is equivalent to an angular quantum number, m is a radial quantum number, and p is a polarization (TE/EH

or TM/HE). The additional E and H field components can be written in terms of E_z and H_z:

$$\begin{aligned} E_r(r,\phi,z) &= \frac{-i\beta}{\omega^2\mu\epsilon-\beta^2}\left(\frac{\partial E_z}{\partial r}+\frac{\omega\mu}{\beta}\frac{\partial H_z}{r\partial\phi}\right) \\ E_\phi(r,\phi,z) &= \frac{-i\beta}{\omega^2\mu\epsilon-\beta^2}\left(\frac{\partial E_z}{r\partial\phi}-\frac{\omega\mu}{\beta}\frac{\partial H_z}{\partial r}\right) \\ H_r(r,\phi,z) &= \frac{-i\beta}{\omega^2\mu\epsilon-\beta^2}\left(\frac{\partial H_z}{\partial r}-\frac{\omega\mu}{\beta}\frac{\partial E_z}{r\partial\phi}\right) \\ H_\phi(r,\phi,z) &= \frac{-i\beta}{\omega^2\mu\epsilon-\beta^2}\left(\frac{\partial H_z}{r\partial\phi}+\frac{\omega\mu}{\beta}\frac{\partial E_z}{\partial r}\right) \end{aligned} \tag{3.2}$$

The propagation constant of each optical mode is given by β, where β is determined from the transcendental equation,

$$\begin{aligned} \left(\frac{J_l'(ha)}{haJ_l(ha)}+\frac{K_l'(qa)}{qaK_l(qa)}\right)\left(\frac{n_{core}^2J_l'(ha)}{haJ_l(ha)}+\frac{n_{clad}^2K_l'(qa)}{qaK_l(qa)}\right) \\ = (l\beta/k)^2\left((qa)^{-2}+(ha)^{-2}\right)^2 \end{aligned} \tag{3.3}$$

Solution of this equation results in a set of discrete propagation constants for the guided modes of the waveguide for each fixed waveguide diameter and excitation wavelength. The lowest order fiber mode (which is always supported) is the HE_{11} mode. A graph of the effective index (propagation constant normalized to the free-space wavenumber) for each guided mode in a step-index fiber versus the normalized waveguide parameter ka is given later in figure 3.6. The refractive index is assumed to be that of silica at a wavelength of 1550 nm (n=1.45), with the waveguide parameter chosen to lie within the sizes required to optimally couple to the optical microresonators studied in this work. In a physical sense, this propagation constant determines the spatial period of the electric field oscillation along the waveguide length.

3.2 Analytic model of coupling to and from a microcavity

3.2.1 Single-mode model

The optical transfer of energy between a single mode of the waveguide and a single-cavity mode can be described through a simple model [38], as illustrated in figure 3.3. The internal

cavity field is determined by accounting for all sources of cavity loss and excitation, and is given for resonant excitation by the following equation:

$$\frac{da}{dt} = -\frac{1}{2}\left(\kappa_0^2 + \sigma_0^2\right) a + i\kappa_0 s \tag{3.4}$$

where a represents the energy amplitude in the cavity. The first term represents the total energy amplitude loss rate of the cavity[4], due to contributions from the intrinsic resonator loss σ_0, and external coupling κ_0. The last term gives the excitation of the resonator by the waveguide with coupling coefficient κ_0 [5], with s denoting the power normalized waveguide field. The phase of this term is representative of the fact that the wave undergoes a $\pi/2$ phase shift upon coupling between the cavity and waveguide. This equation holds if the internal losses and external coupling are small enough such that their effect on the internal field can be treated independently. This condition, while not generally satisfied for optical coupling to resonators, holds for the extremely low loss resonators investigated in this thesis, which is analogous to the behavior of the total resonator Q in terms of each individual loss contribution as discussed in section 2.1. The transmission through the waveguide consists of an interference between the amount of optical power not coupled into the resonator $t_0 \simeq s$ plus the amount coupled out of the cavity, given by the expression,

$$T = |t_0/s + i\kappa_0 a/s|^2 \tag{3.5}$$

Under the assumption of steady-state excitation[6], the differential equation for the internal cavity field reduces to an algebraic expression,

$$a = \frac{i2\kappa_0 s}{\kappa_0^2 + \sigma_0^2} \tag{3.6}$$

[4]In this expression the coupling coefficient $\kappa^2 \equiv 1/\tau_0$ has units of $\sec^{-1}$, resulting from the different normalizations of "a" (energy) and "s" (power), which are related by the cavity round-trip time.

[5]The equivalence of the coupling amplitudes both into and out of the resonator is true only when time-reversal symmetry and power conservation applies, however as will be shown later the coupling junction is nearly lossless so this approximation is justified.

[6]For most of the experiments in this thesis the input optical field frequency was scanned in time over a range much larger than the cavity linewidth. This scanning was done slowly (<100 Hz) such that the excitation is quasi-continuous and the steady-state solution still holds. Also, I might point out that the excitation frequency is assumed to be perfectly monochromatic, which becomes problematic for very high-Q resonances (Q ≃500 million), where the linewidth of the cavity resonance is actually comparable to or smaller than the excitation laser used (<300 kHz).

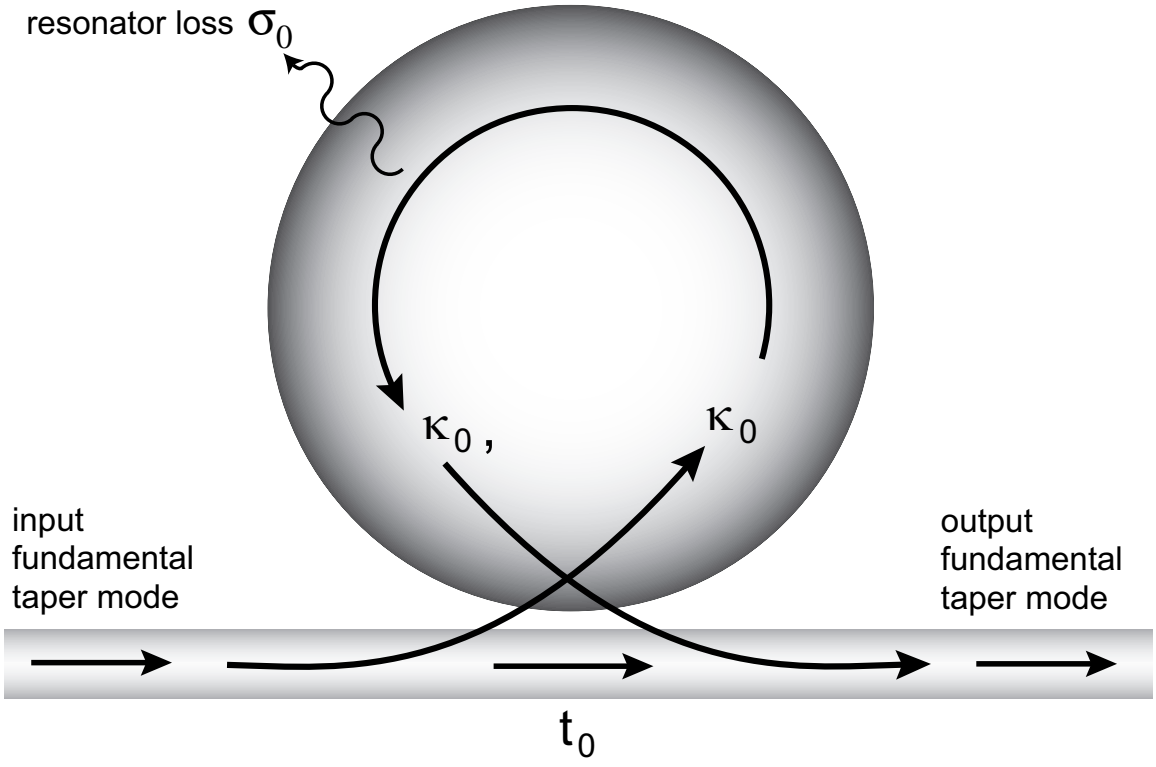

Figure 3.3: Illustration of coupling between a single-mode waveguide and a single mode of the cavity. The input waveguide field couples both into and out of the cavity with amplitude κ_0, and has a transmitted amplitude t_0. The internal resonator mode has a loss amplitude σ_0.

with the resultant waveguide transmission of

$$T = \left(\frac{1-K}{1+K}\right)^2 \text{ with } K \equiv \kappa_0^2/\sigma_0^2 \tag{3.7}$$

In this expression, I have introduced the coupling parameter K, defined as the ratio of coupling between waveguide and resonator to intrinsic resonator loss. This dimensionless parameter allows a simple way to investigate the coupling regimes and properties of this system. Figure 3.4 shows a plot of the waveguide transmission and phase as a function of normalized coupling parameter K. Also shown for comparison are both the overall cavity loss (as given by the total quality factor $Q_{total} = 2\pi c/(\lambda(\sigma_0^2 + \kappa_0^2))$) and the circulating power inside the cavity for an intrinsic quality factor of 100 million ($Q_0 = 2\pi c/(\lambda\sigma_0^2)$) at a resonance wavelength of 1550 nm. The plot shows that there are clearly different regimes of operation of this system, which can be described in analogy to that of a driven harmonic oscillator. For $K << 1$ the transmission through the waveguide approaches unity, as expected, since this means that the coupling into the cavity is negligible. For larger amounts of coupling, still such that $K < 1$, there is a transmission drop as power is coupled into the cavity, as shown by the increase in the cavity circulating power. This regime is denoted undercoupled, as coupling is less than the cavity loss. As coupling is increased to the point where input coupling just balances the cavity loss ($K = 1$), the transmission vanishes. This is known as critical-coupling. This point is of tremendous significance and importance for both active and passive optical devices. The fact that the waveguide transmission can be negligible suggests that this system is of use for removing a very specific optical frequency from the waveguide. When modified to incorporate a second waveguide, this can lead to optical add/drop devices. Furthermore, as at the critical coupling point there is no waveguide transmission, all the incident power is coupled into the microcavity. This is illustrated by a maximum of the circulating power inside the cavity. The ability to obtain complete power transfer into the microcavity is of primary importance for lasing and nonlinear devices, where the ultra-high-quality factors of certain cavities can result in massive circulating powers and dramatically lower thresholds for lasing and nonlinear effects to modest input powers, as discussed in more detail in chapter 4. When coupling is further increased ($K > 1$), the transmission rises, with a corresponding drop of circulating power. This point is known as overcoupled. Although the behavior of the waveguide

transmission and circulating power is identical to that of the undercoupled regime, there is a fundamental difference between overcoupled and undercoupled. Observing the phase-response of the waveguide field, we see that the phase undergoes a π phase-shift. Furthermore, the fact that in the overcoupled regime the output coupling dominates the cavity loss is advantageous to creating practical devices, where maximal extraction of power from the resonator is desired.

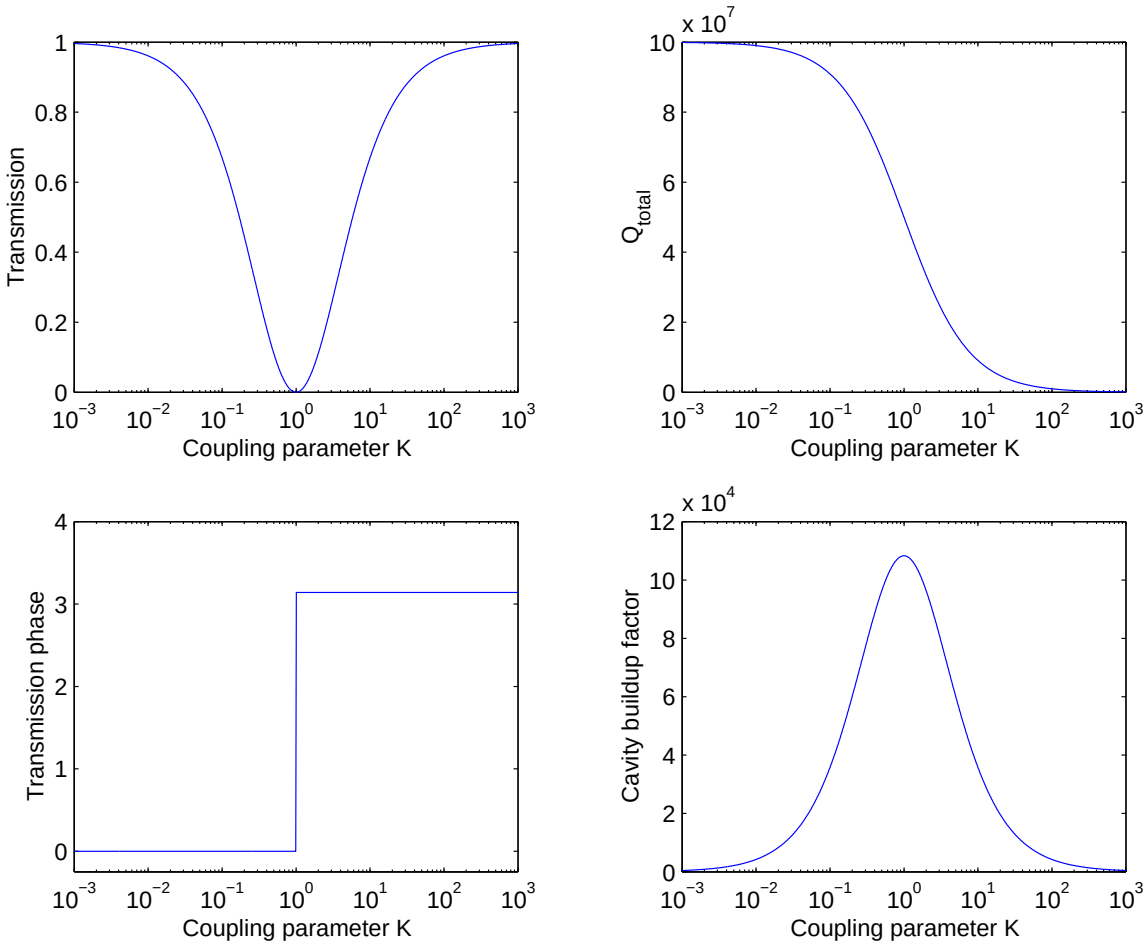

Figure 3.4: Plot of waveguide transmission, phase, cavity build-up factor, and cavity total quality factor as a function of coupling parameter K for a 50-micron-diameter resonator with an intrinsic quality factor of 100 million at a resonance wavelength of 1550 nm. The regimes of operation are indicated. At the critical point the waveguide transmission vanishes with a corresponding peak in circulating power.

3.2.2 Phase-matching

While the previous section discussed the theory of coupling between a cavity and waveguide, the specific conditions under which efficient coupling occurs were not specified. This is manifested in the coupling parameter K through the waveguide-resonator coupling amplitude κ. In practice, the requirement to access the beneficial properties of a waveguide-cavity system depends critically on the ability to efficiently excite the cavity, such that the coupling amplitude can be at least comparable to the intrinsic cavity loss. Otherwise, no matter how hard one tries, the system will permanently be undercoupled, which severely decreases the utility and ability of resonant structures for practical applications. This section will discuss the determination of the waveguide-cavity coupling amplitude κ.

The determination of the coupling between two waveguides can be calculated either exactly (through the use of supermodes) or approximately (using coupled mode theory). As the coupling between the waveguide and cavity is weak (i.e., $\kappa << 1$) for excitation of UHQ resonators, the optical modes in both the waveguide and cavity are essentially those of the isolated waveguide and cavity. Thus, the optical coupled mode approach [64] is suitable to investigate this problem. Under this approximation, the coupling coefficient between the waveguide and cavity (and cavity to waveguide) is given by the following expression,

$$\kappa_{i,j} = \frac{\omega\epsilon_0}{4}\int_A (n_i^2 - n^2(\vec{r}))\vec{E}_i \cdot \vec{E}_j dA \tag{3.8}$$

where $\vec{E}_{i,j}$ represents the unperturbed optical modes of the waveguide and cavity, and $n^2(\vec{r})$ denotes the refactive index profile of the composite system. While the integration is over the cross-sectional area of the structure, the first factor in the integral is only nonzero over the core of the waveguide or resonator, depending on which coupling coefficient (waveguide to resonator, or vice versa) is desired. While this expression is simple for the case of two waveguides such that the cross-sectional geometry is invariant over the entire coupling region, the case of a curved waveguide (such as is present for the resonators in this work) is more difficult. In this case the coupling coefficient κ is a function of the distance along the waveguide with respect to the point of minimum waveguide/resonator separation. This case has been investigated in the literature [65], and a modified coupled mode theory which accounts for the

presence of curved waveguides was developed [66]. By using a geometrical transformation to a coordinate system such that the transformed waveguides are parallel, the standard coupled mode theory can be used. Under this approach, the coupling amplitude only needs to be determined for the minimum separation between waveguide and cavity, using equation 3.8, with the dependence of coupling amplitude on position along the waveguide now Gaussian,

$$\kappa(z) \simeq \kappa_{0,\perp} exp(-wz^2/D) \tag{3.9}$$

with

$$\kappa_{0,\perp} = \sqrt{\kappa_{ij}\kappa_{ji}}$$
$$w = (w_1 + w_2)/2$$
$$w_i = \sqrt{\beta_i^2 - k^2 n_{clad}^2}$$

Here, $\kappa_{0,\perp}$ denotes the geometric mean of the coupling amplitude between the waveguide/resonator and resonator/waveguide at minimum separation. D denotes the cavity diameter, with β_i representing the propagation constant of the respective waveguide or resonator mode. This equation uses the fact that the coupling strength between two parallel waveguides is exponential with separation between the two waveguides (because of the exponential decay of the external evanescent fields) and by assuming the interaction region is approximated by a parabolic surface.

The propagation constant of the resonator as seen by the waveguide decreases with distance from the minimum waveguide/cavity separation according to,

$$\beta_{sphere,eff} \simeq \beta_{sphere}\left(1 - d_{sep}/D - (z/D)^2\right) \tag{3.10}$$

where $\beta_{sphere} = m/(D/2)$ is the intrinsic propagation constant of the resonator mode, and d_{sep} gives the separation between the center of the resonator mode and the center of the waveguide mode. This equation defines an effective propagation constant $\beta_{sphere,eff}$ which is more accurate when determining the overall coupling. Now, the total coupling amplitude is given by the integration of $\kappa(z)$ over the entire length of the region where there is appreciable

coupling, by solving the system,

$$\begin{aligned} \frac{da_{fiber}}{dz} &= i\beta_{fiber}a_{fiber} + i\kappa(z)a_{resonator} \\ \frac{da_{resonator}}{dz} &= i\beta_{sphere,eff}a_{resonator} + i\kappa(z)a_{fiber} \end{aligned} \tag{3.11}$$

While the determination of the total coupling coefficient must be done numerically, considerable insight can be gained by studying the coefficient at the minimum separation. For coupling between two parallel waveguides, the overall coupling is an oscillatory *sinc* function of the term $\Delta\beta = \beta_f - \beta_s$. This factor, which strongly affects the coupling amplitude, is the phase-mismatch between both fields. Maximal coupling occurs when $\Delta\beta = 0$, a condition known as phase-matching. By analogy, the overall coupling strength between a straight waveguide and a curved resonator is expected to be maximum when the phase-mismatch at the point of strongest coupling (the minimum separation point) vanishes. Figure 3.5 illustrates physically how phase-matching works for a waveguide/resonator system. In simple terms, to obtain optimal coupling the spatial period of the optical waves in both the waveguide and resonator must match, leading to constructive interference. If the periods are different, there is imperfect interference, leading to a reduced power transfer. For the case of a curved waveguide (i.e. resonator) coupled to a straight waveguide, the optical field of the resonator must be projected onto the same coordinate system as the waveguide. Using the known forms of the fields for a circularly symmetric resonator (projected onto same direction as the waveguide) and a straight waveguide,

$$\begin{aligned} \vec{E}_{resonator}(\vec{r}) &= \vec{E}_{T,res}exp(im\phi) \simeq \vec{E}_{T,res}exp(i(m/R)(R\phi)) = \vec{E}_{T,res}exp(i\beta_{resonator}z) \\ \vec{E}_{fiber}(\vec{r}) &= \vec{E}_{T,fiber}exp(i\beta_{fiber}z) \end{aligned} \tag{3.12}$$

we see that a simple condition for phase-matching is

$$\begin{aligned} \Delta\beta = \beta_{resonator} - \beta_{fiber} = m/R - \beta_{fiber} = 0 \\ \Rightarrow \beta_{fiber} = m/R \end{aligned} \tag{3.13}$$

This equation is typically what is considered in the literature when describing coupling between a resonator and a waveguide. However, this equation does not truly give the condition under which the fields are completely phase-matched, as an account of both the transformation

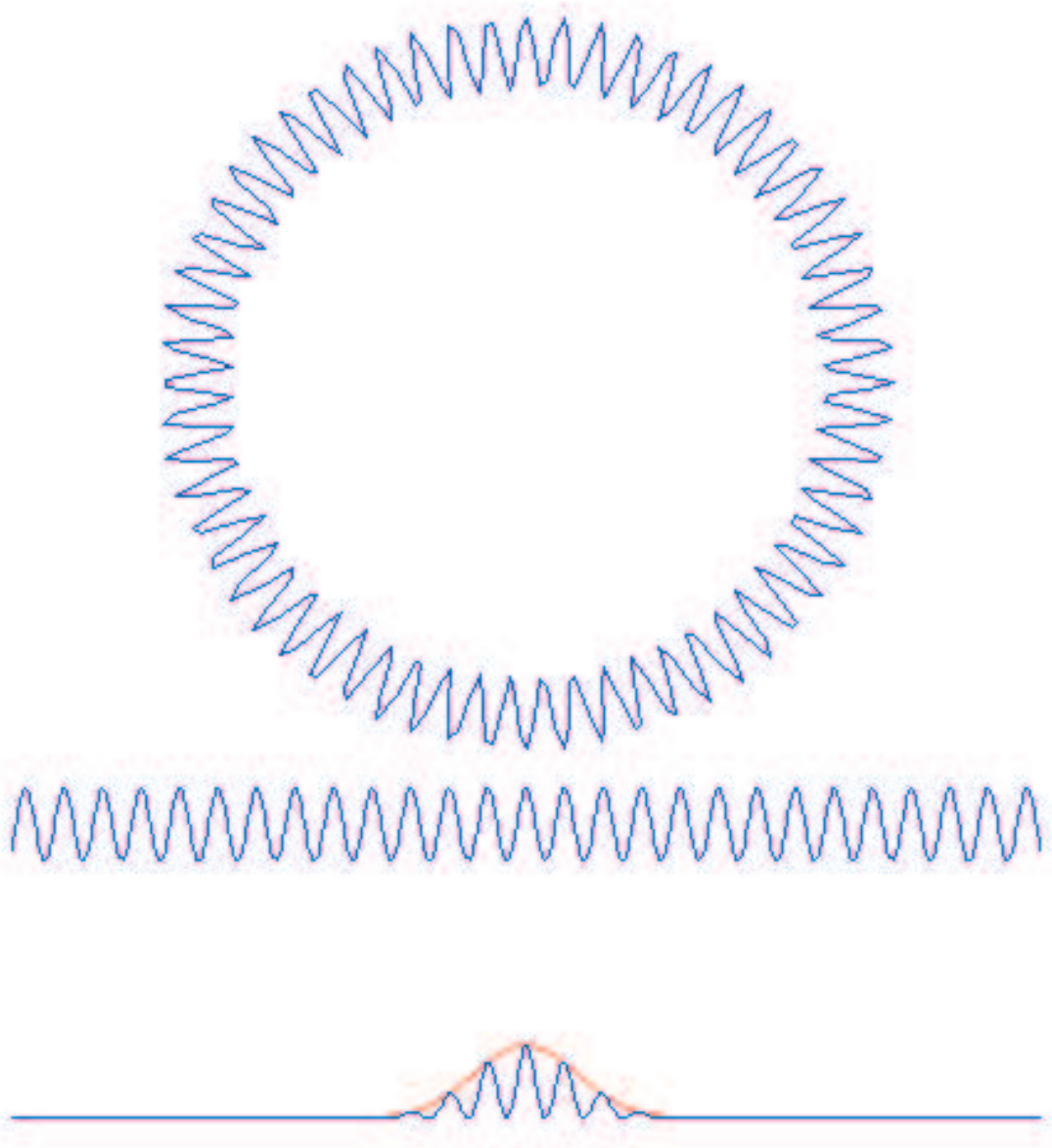

Figure 3.5: Illustration of phase-matching process. The spatial variations of the optical field in both the resonator and waveguide are shown, with the projection of the resonator field onto the waveguide coordinate system. The Gaussian envelope represents the effect of the resonator curvature on the coupling coefficient as a function of separation between the resonator and waveguide.

process and the fact that there is a spatial separation of the waveguide and resonator. In this case the true phase-matching condition (assuming the fiber is in contact with the sphere) is given by

$$\beta_{fiber} = \beta_{sphere}\,(1 - d/(4D)) \tag{3.14}$$

where d denotes the fiber diameter. In order to delineate these two conditions I will call the simple intuitive approach the simple phase-matching condition and the rigorous model the exact phase-matching condition[7].

In practice, the use of the simple phase-matching relation gives an easy way to determine the suitable waveguide and resonator parameters to obtain efficient coupling. For example, figure 3.6 demonstrates this process for phase-matched coupling to a silica microsphere. Both the dispersion relation for a silica microsphere (fundamental mode with both TE and TM polarizations) and a tapered optical fiber are shown overlaid on the same graph. The propagation constants are given in terms of the effective modal index, which is simply the propagation constant normalized by the free-space wavenumber. By matching the effective index of the desired microsphere mode (given by choosing the appropriate polarization and physical size R/λ) to that of the fundamental HE_{11} fiber taper mode, the requisite value of a/λ can be determined. The data indicates that for a 75-micron-diameter microsphere with excitation of the fundamental TE WGM at a wavelength of 1550 nm, the necessary taper diameter is 2.3 microns. Figure 3.7 shows the calculated tapered-fiber diameter needed to phase-match the fundamental TM mode of a silica microsphere at a wavelength of 1550 nm. Both the simple expression and the exact expression are shown. The data indicate that the exact phase-matching expression requires a uniformly smaller fiber diameter for a fixed microsphere diameter. This is a consequence of the fact that as the waveguide is located outside the resonator the local resonator propagation constant is smaller than given by the simple relation, thus requiring a smaller waveguide propagation constant as well.

While the choice of the proper phase-matching relation is necessary to obtain optimal power transfer between a waveguide and resonator [67], there is another effect in this system which has the potential to dramatically decrease the amount of coupling in this system. This

[7]To be completely rigorous this expression should also include the fact that the resonator mode center lies slightly below the resonator outer boundary. This has not been accounted for as it requires knowledge of the resonator field profiles.

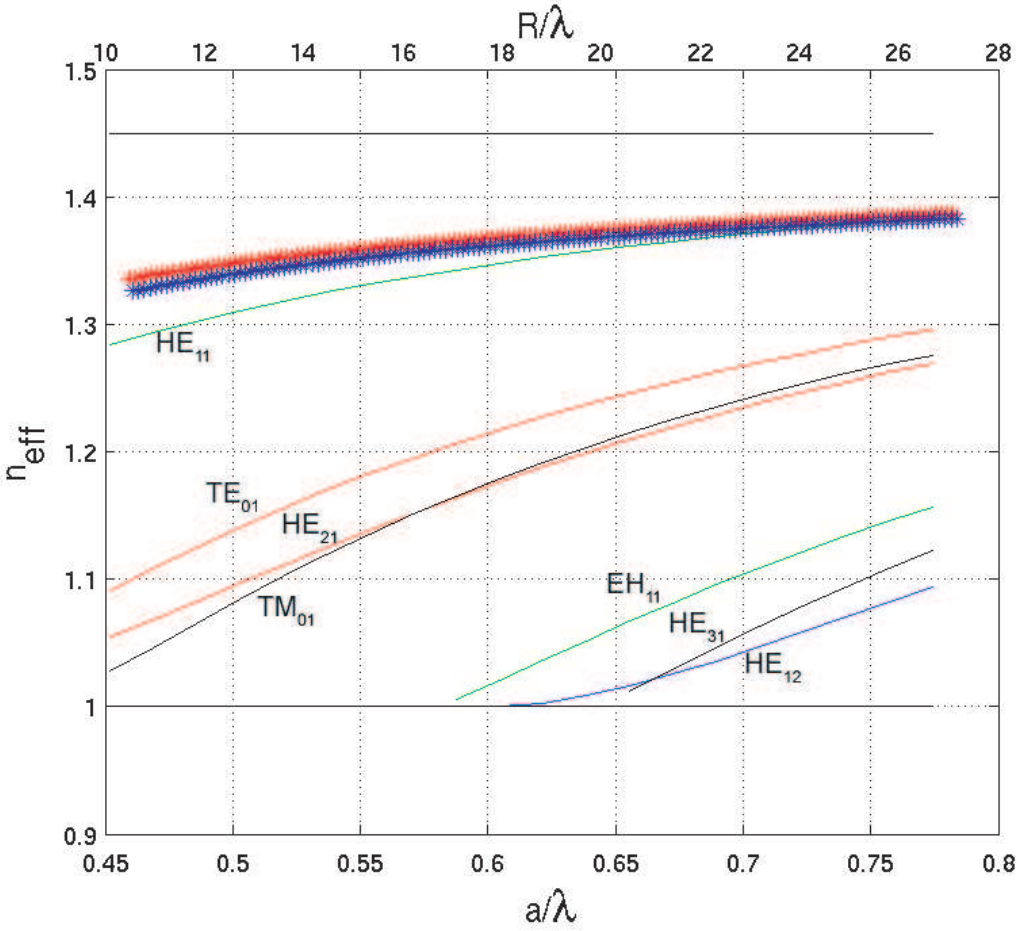

Figure 3.6: Phase-matching a silica microsphere to a fiber taper. Both the microsphere dispersion (fundamental TE (blue stars) and TM (red stars) WGM's) and the fiber dispersion are shown. Matching of the effective index indicates that a 75-micron-diameter microsphere requires a 2.3 micron diameter taper to phase-match.

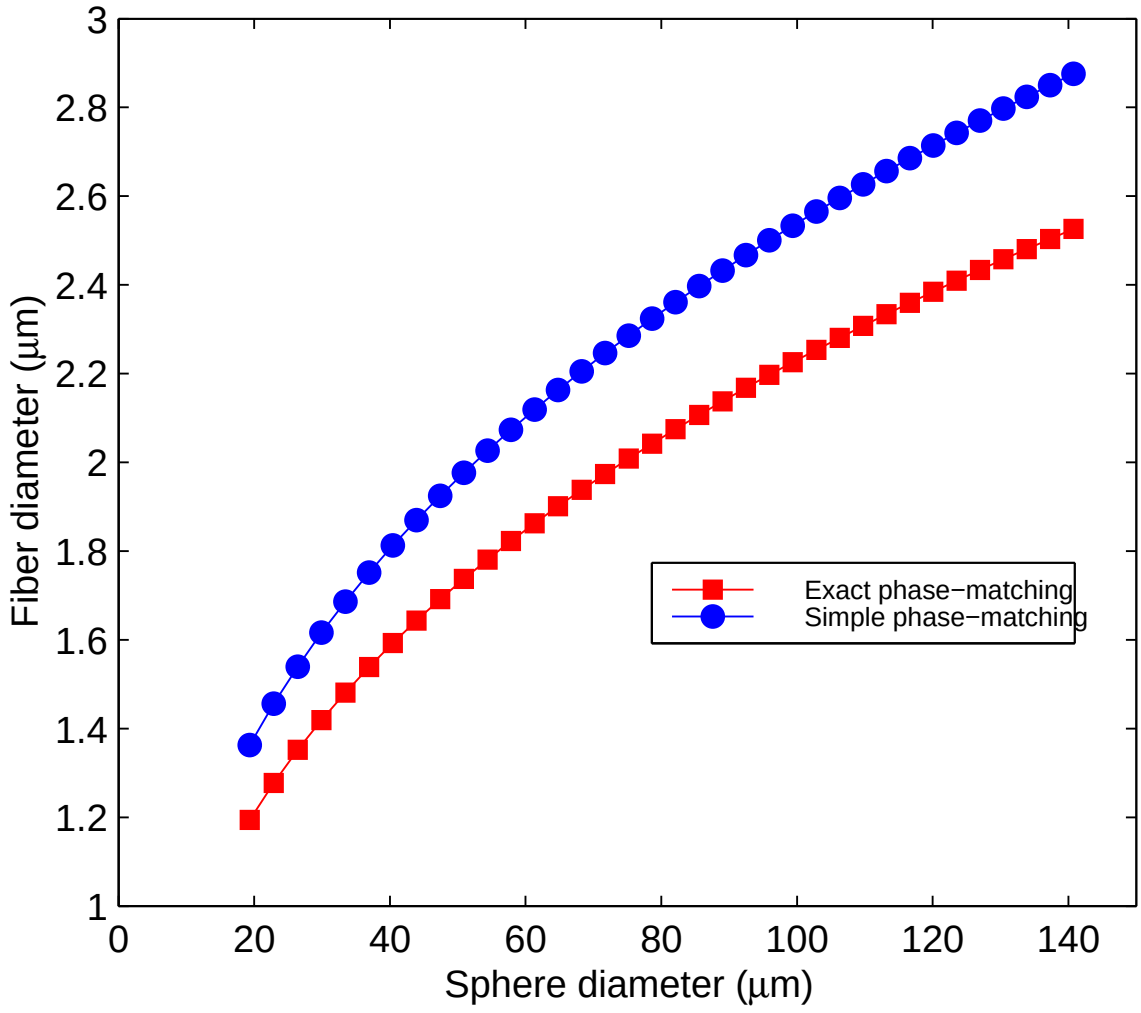

Figure 3.7: Fiber-taper diameter required to phase-match a silica microsphere. The silica microsphere mode excited is a fundamental TM mode near 1550 nm. The data indicate that the exact phase-matching relation requires a smaller fiber diameter for a given microsphere diameter.

arises from the observation in figure 3.6 that for the optimal phase-matching point (for either the simple or exact relations), the requisite fiber supports multiple guided modes. This can have profound consequences in the overall behavior of a resonator/waveguide system.

3.3 Multimode model

In general, when coupling between two multimode waveguides (or resonators) there will be cross-coupling between all of the available optical guided and radiation modes. Thus, the coupling between a multimode fiber taper and a multimode resonator is more complicated than the simple single-mode coupling model typically used. The effects of a multimode resonator and a multimode waveguide are manifested in two ways: coupling into a different resonator mode from the input fiber mode, and coupling from each resonator mode into all supported fiber modes (plus radiation modes). By using an adiabatic taper it is always possible to launch the fundamental HE_{11} taper mode. Likewise, excitation of a single resonator mode is possible through a combination of phase-matching and modal frequency selection. For example, in the resonators considered in this thesis the power coupling coefficient to the next closest resonator mode is on the order of 10^{-8} (assuming a mode linewidth of 1 MHz and a mode spacing of 10 GHz). However, a resonator mode, once excited, can transfer power back to many taper modes (as illustrated in figure 3.8), with reasonable efficiency due to the lack of modal frequency selection in a waveguide. Additionally, the presence of the taper waveguide can cause the resonator to couple power into the continuum of radiation modes (and induce scattering at the resonator-waveguide junction).

The effect of output coupling to additional optical modes can be simply accounted for by modification of the approach described in section 3.2.1, by adding additional loss terms to the equation for the internal energy amplitude decay rate representing the effect of higher-order waveguide modes ($\kappa_{i>0}$) and of radiation modes (κ_{rad}):

$$\frac{da}{dt} = -\frac{1}{2}\left(\sum_{i=0} \kappa_i^2 + \kappa_{rad}^2 + \sigma_0^2\right) a + i\kappa_0 s \tag{3.15}$$

with the terms defined in section 3.2.1. Assuming the power coupled into higher-order taper modes is lost upon transition to single-mode fiber, equation 3.5 holds for the waveguide

transmission, resulting in steady-state:

$$T = \left(\frac{1-K}{1+K}\right)^2 \tag{3.16}$$

where the coupling parameter K is now defined by

$$K \equiv \frac{\kappa_0^2}{\sum\limits_{i\neq 0} \kappa_i^2 + \kappa_{rad}^2 + \sigma_0^2} \tag{3.17}$$

K is defined as the ratio of the desired waveguide-mode power coupling to the *total* system power loss. This is a more general definition of K, not restricted to a single-mode coupler.

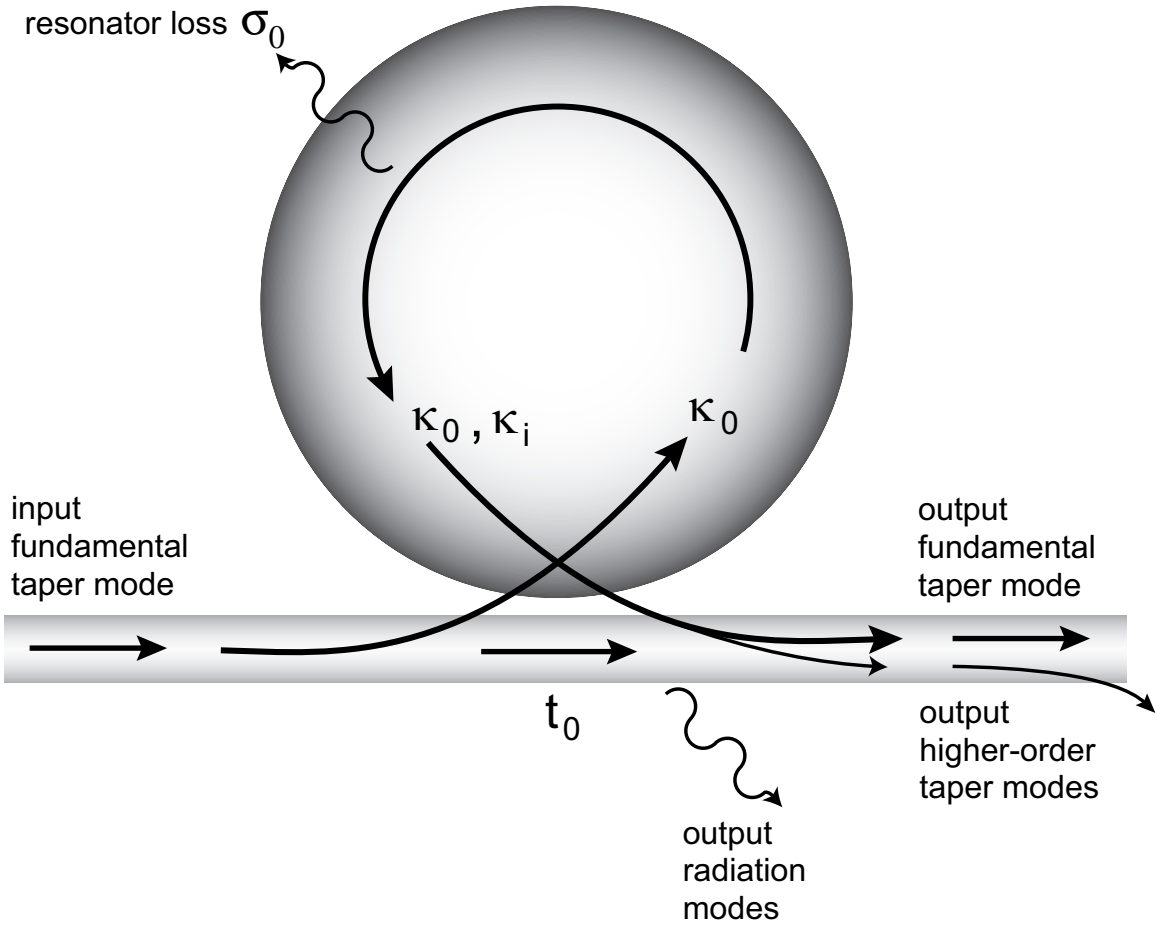

Figure 3.8: Coupling and loss parameters in a taper-microresonator system. The input field is a fundamental taper mode which couples into the resonator with amplitude κ_0 (transmission amplitude t_0). The output field couples into the fundamental taper mode and higher-order taper modes with coupling constants κ_0 and κ_i, respectively [68]. The presence of the waveguide can also result in a radiated field. The higher-order taper modes are radiated or coupled to cladding modes upon transition of the taper back to single-mode fiber. The round-trip resonator intrinsic power loss is given by σ_0^2.

3.3.1 Ideality

The previous subsection described how the presence of coupling to additional optical modes modifies the transmission of the waveguide, by increasing the effective resonator loss. It is of course important to investigate the conditions under which this extra coupling causes problems with assuming a single-mode to single-mode model (which obviously is desirable from a simplicity standpoint). As such, the coupling factor K can be decomposed into two factors which give the relative importance of these extra coupling channels; an intrinsic contribution

$$K_I \equiv \kappa_0^2/\sigma_0^2 \tag{3.18}$$

and a parasitic contribution

$$K_P \equiv \kappa_0^2/(\sum_{i\neq 0} \kappa_i^2 + \kappa_{rad}^2) \tag{3.19}$$

such that

$$K^{-1} = K_I^{-1} + K_P^{-1} \tag{3.20}$$

In order to characterize the degree to which a coupler behaves as a single-mode to single-mode coupler, a figure of merit called ideality is used. Ideality is defined as the ratio of power coupled into the desired mode (in this case the fundamental HE_{11} mode) to the amount of power coupled into all modes, and is given by

$$I \equiv \frac{\kappa_0^2}{\sum_{i=0} \kappa_i^2 + \kappa_{rad,T}^2} = \frac{1}{1 + K_P^{-1}} \tag{3.21}$$

An ideal waveguide coupler ($I = 1$) is characterized by coupling only between the intended resonator and waveguide modes. The degree of ideality is determined by the parasitic coupling factor K_P. K_P is, in general, a function of the relative position between the waveguide and the resonator, and, as such, the deviation of K ($K^{-1} = K_I^{-1} + K_P^{-1}$) from ideal behavior ($K = K_I$) determines I.

The experimental determination of ideality can be done very accurately by probing the waveguide transmission as a function of K (by measuring the dependence of coupling on

waveguide-resonator separation) and inverting equation 3.16 as follows:

$$\left(\frac{1 \pm \sqrt{T}}{1 \mp \sqrt{T}}\right) = K = \frac{\bar{\kappa}_0^2 e^{-\gamma_0 x}}{\bar{\kappa}_i^2 e^{-\gamma_i x} + \sigma_0^2} \tag{3.22}$$

where the upper signs are taken for transmission values in the over-coupled regime, and the lower signs for the under-coupled regime. The second equality follows from equation 3.17 by noting that the coupling amplitudes κ_0 and κ_i decrease exponentially with resonator/waveguide separation and by assuming that K_P is dominated by a single higher-order taper-waveguide mode (as shown below this assumption is valid for the data in this work). γ_0 (γ_i) are spatial decay rates (versus gap x) such that $\kappa_{0,i}^2 \equiv \bar{\kappa}_{0,i}^2 exp(-\gamma_{0,i} x)$ with $x = 0$ corresponding to zero separation. As demonstrated experimentally in section 3.4, upon plotting K vs. separation on a logarithmic scale, K_I and K_P can often be identified, as K_P (for higher-order taper mode parasitic coupling) is a line with slope less than that of K_I. In particular, if $\bar{\kappa}_i^2 > \sigma_0^2$ then the relation $K^{-1} = K_I^{-1} + K_P^{-1}$ results in a roll-off of K for small separation distances due to parasitic coupling. In situations where $\bar{\kappa}_i^2 < \sigma_0^2$, the higher-order mode coupling is masked and a lower bound on ideality can be established.

3.3.2 Extension to backscattering

In the previous sections I have described the coupling between a waveguide and a single mode of the resonator, as this system forms the basis for studying optical effects in waveguide-coupled microresonators. This was done because of the ideal traveling-wave behavior of a circular resonator, where the optical wave travels unidirectionally around the cavity periphery. However, the assumption of a true unidirectional traveling-wave mode does not always hold, especially when considering the ultra-high-Q microresonators which are the focus of this thesis. The extremely low loss representative of UHQ cavities has a deleterious effect on this unidirectional behavior: even minute amounts of backscattering from any of a number of scattering mechanisms (surface scattering, intrinsic scattering centers, or material inhomogeneities) can build up appreciable circulating fields in the opposite circulating directions [69]. Not only does this change the cavity behavior to contain a standing-wave component, which reduces the cavity circulating power, but also results in optical power leaking out in the backward direction of

the cavity. As this effect is omnipresent in UHQ resonators, this must also be accounted for when considering the full coupling behavior of a waveguide-coupled system.

The analysis of the coupling between a waveguide and a resonator can still be modeled with a harmonic oscillator approach, with now the clockwise and counterclockwise resonator fields coupled through a scattering rate amplitude γ (see figure 3.9), as described by the equations:

$$\begin{aligned}\frac{da_{ccw}}{dt} &= -\frac{1}{2}\left(\frac{1}{\tau_0}+\frac{1}{\tau_{ex}^{o}}+\frac{1}{\tau_{ex}^{i}}+\frac{1}{\tau_{ex}^{rad}}\right)a_{ccw}+i\kappa_0 s_{in}^{+}+i\frac{\gamma^2}{2}a_{cw}\\ \frac{da_{cw}}{dt} &= -\frac{1}{2}\left(\frac{1}{\tau_0}+\frac{1}{\tau_{ex}^{o}}+\frac{1}{\tau_{ex}^{i}}+\frac{1}{\tau_{ex}^{rad}}\right)a_{cw}+i\frac{\gamma^2}{2}a_{ccw}\end{aligned} \tag{3.23}$$

The transmission can be determined through the same approach as in the previous sections, with the reflection also given by $R = |\kappa_0 a_{cw}/s|^2$, with the final expressions:

$$\begin{aligned}T &= \left(\frac{(1+K)(1-K)+\Gamma^2}{(1+K)^2+\Gamma^2}\right)^2\\ R &= \left(\frac{2\Gamma K}{(1+K)^2+\Gamma^2}\right)^2\\ K &= \frac{\kappa_0^2}{\sigma_{eff}^2}\ , \qquad \Gamma = \frac{\gamma^2}{\sigma_{eff}^2}\end{aligned} \tag{3.24}$$

with

$$\sigma_{eff}^2 \equiv \sigma_0^2 + \kappa_i^2 + \kappa_{rad}^2$$

with K defined identically to the previous sections, and Γ representing a normalized mode-splitting parameter, which describes the ratio of scattering to intrinsic resonator loss (including coupling to higher-order waveguide and scattering modes). Observation of the coupling behavior of this system indicates that a significant modification from traveling wave behavior occurs, as described more extensively in reference [70].

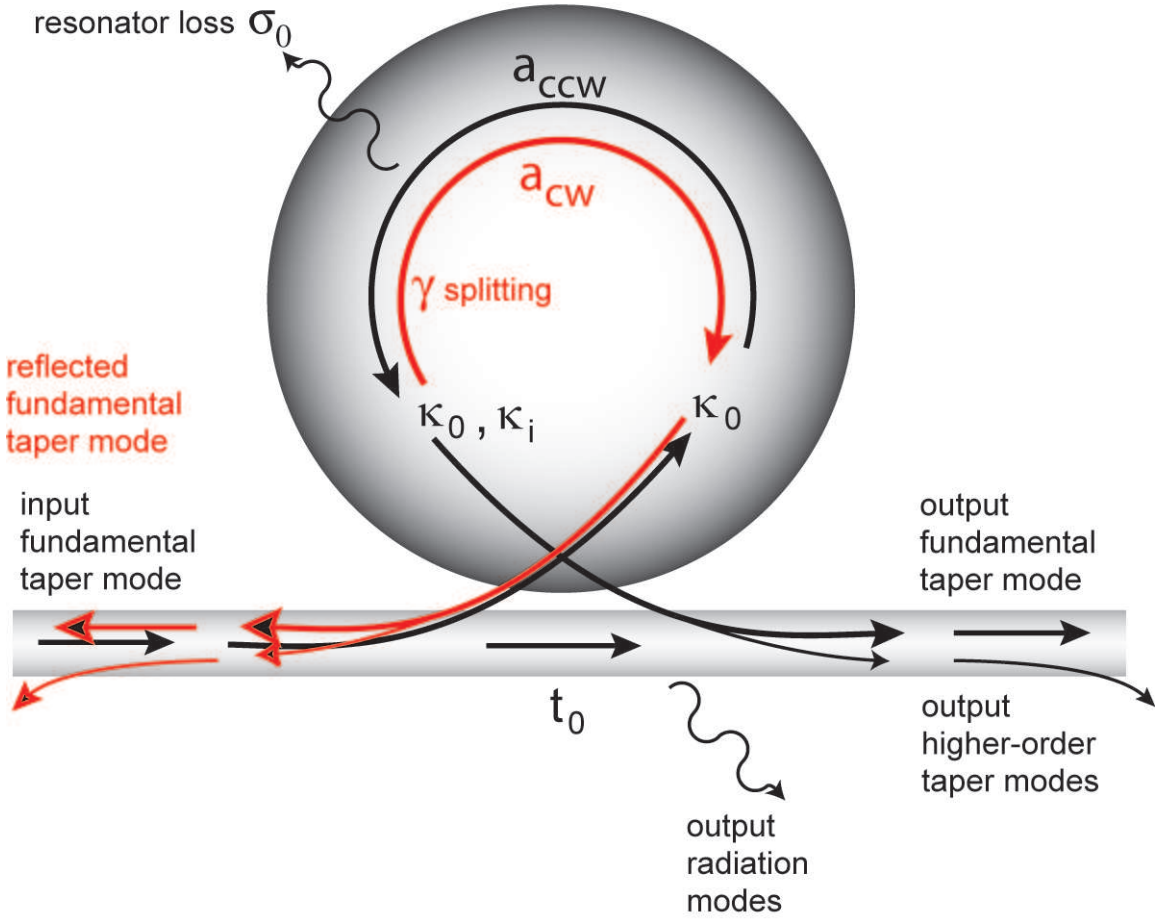

Figure 3.9: Illustration of coupling between a multimode waveguide and a resonator that has intrinsic coupling between cw and ccw circulating modes. In addition to the optical power output through the forward waveguide direction, there is a reflected field (indicated in red) due to cross-coupling amplitude γ.

3.4 Experimental observation of coupling

A major part of this thesis has focused on the understanding of the necessary conditions and the experimental realization of ultra-efficient coupling between a tapered-fiber waveguide system and ultra-high-Q microresonators (first, microspheres and later microtoroids). In the past there has been much work on efficiently coupling to silica microspheres, ranging from utilizing prism couplers to many varieties of fiber waveguides. However, the most promising results were obtained with fiber-taper-coupled microresonators in the Vahala group, with the first realization of critical coupling in the optical domain [20]. This important step now opened the door to investigation of optical phenomena which requires ultra-efficient transfer of energy into the cavity. Nevertheless, this previous work not only failed to investigate the opposite process (ultra-efficient *extraction* of optical energy from the resonator), but used an experimental setup which obtained critical coupling by introducing artificial loss, such that a system initially biased into the overcoupled regime is brought backwards to critical coupling. In order to truly realize the full potential of UHQ resonators for fundamental studies, not only must we avoid the technique of introducing artificial loss, but must demonstrate conclusively the coupling behavior of such a system.

Thus, a new experimental apparatus was constructed in order to overcome the limitations of previous experimental work and to provide a high-resolution platform for further investigations into the suitability of fiber-coupled microresonators for nonlinear and quantum optics. This setup consists of a silica microresonator (either a microsphere or a microtoroid) mounted onto a z-axis piezo positioner (Burleigh inchworm) with a tapered optical fiber mounted to a custom fiber holder on a xy-axis inchworm positioner. Each positioner has a closed-loop resolution of 20 nm. In particular, this new positioner capability allowed both maintaining of an air gap between the fiber and resonator and nanometer level control of the coupling strength. The optical fiber was excited by a tunable external-cavity New Focus Velocity Laser with a short-term linewidth of $<$300 kHz at a wavelength in the 1550 nm telecommunications band.

The coupling between a fiber-taper and microsphere was investigated by varying the coupling strength through modification of the resonator-waveguide gap and monitoring the waveguide transmission and reflection. The transmission data are obtained by normalizing the on-resonance power transmission with the power transmitted by the taper alone (i.e., infinite

gap).

Figure 3.10 shows the transmission through the fiber-taper as a function of the separation between the fiber and a silica microsphere. The figure shows that it is possible to operate this system in all three coupling regimes. The data show that critical coupling is readily achievable with a relatively large fiber-resonator separation (0.9 micron), with high extinction[8]. Furthermore, it was possible to obtain near complete recovery of the optical transmission, with an overcoupled transmission of 99.95%. This value was only limited by the intrinsic loss of the resonator used. Additionally, even though the fiber used was multimode, the ideality was still high, such that the simple single-mode coupling model accurately predicts the optical transmission (as shown by the fitted red line). Comparison of this data to that obtained with other coupling techniques shows that not only are record high extinctions obtained (believed to be limited by our control of input polarization), but also we have the ability to obtain overcoupled transmissions far exceeding other couplers.

The degree to which the multimode behavior of a fiber-taper waveguide impacts the coupling properties was investigated by changing the modal spectrum of the fiber coupler by varying the position along the taper where the resonator was located. As the tapered fibers have a varying diameter, this technique allows probing of the effect of the local waveguide geometry using the same resonator and optical mode, without any complications resulting from realignment or resonator degradation (the measurements were done quickly enough such that the reduction of quality factor was negligible). Figure 3.11 shows the resulting data, plotted in terms of coupling parameter K versus waveguide/resonator separation according to section 3.3.1. Figure 3.11 shows K versus gap curves for multiple fiber-taper diameters. The taper diameters, measured by a scanning electron microscope (SEM), are approximately 1.2 micron (circles), 1.35 micron (stars), and 1.65 micron (triangles). For the smallest taper diameter measured, three waveguide modes are supported, the HE_{11}, TE_{01}, and TM_{01} modes, although both higher-order modes are near cutoff. There are 4 modes supported (adding the HE_{21} mode) for the two larger taper diameters. The data show that for increasing taper diameter there is a deviation of K from the single-mode coupling regime (dashed lines) due to higher-order mode coupling. A fit using equation 3.22 shows excellent agreement (solid

[8]For this measurement, the critical coupling extinction was not characterized, but subsequent work has demonstrated that values exceeding 30dB are possible.

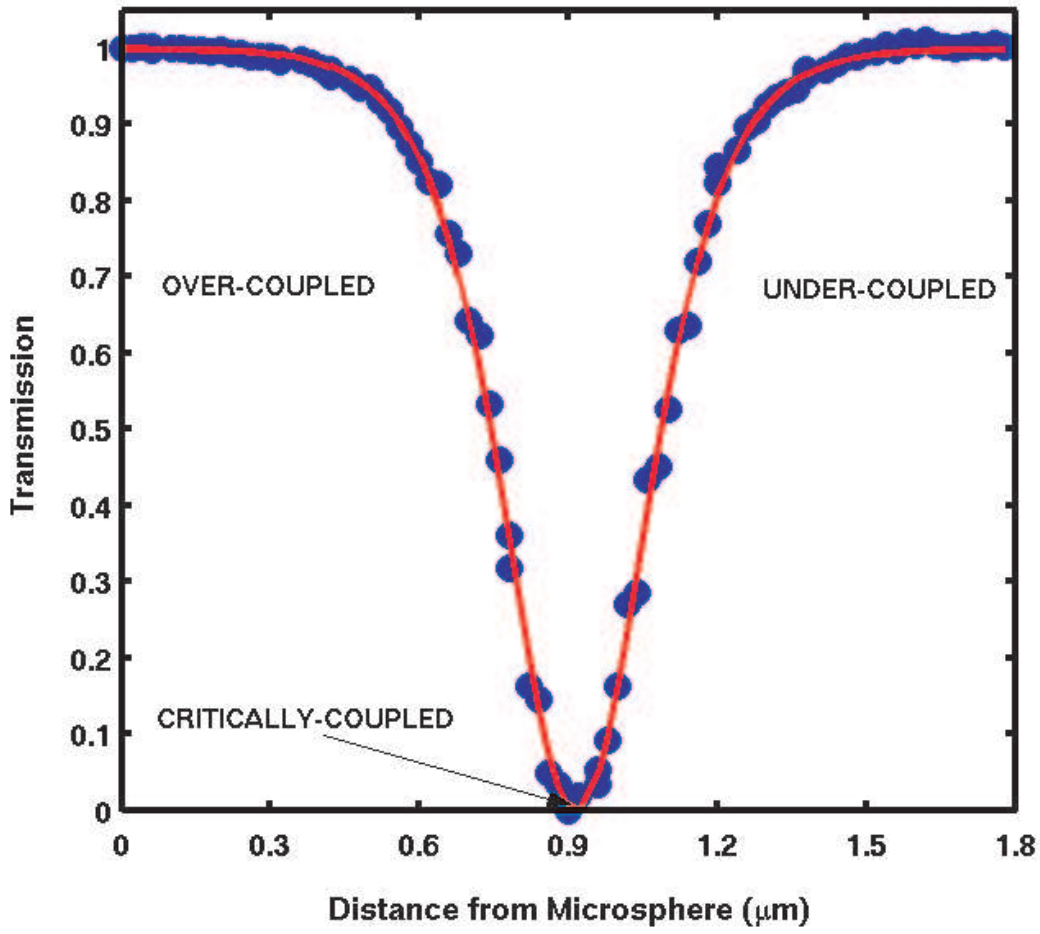

Figure 3.10: Transmission through a fiber-taper as a function of the separation between the fiber and a silica microsphere. The red line represents ideal single-mode behavior. The data shows that it is possible to obtain both critical coupling and strong overcoupling ($T > 99\%$).

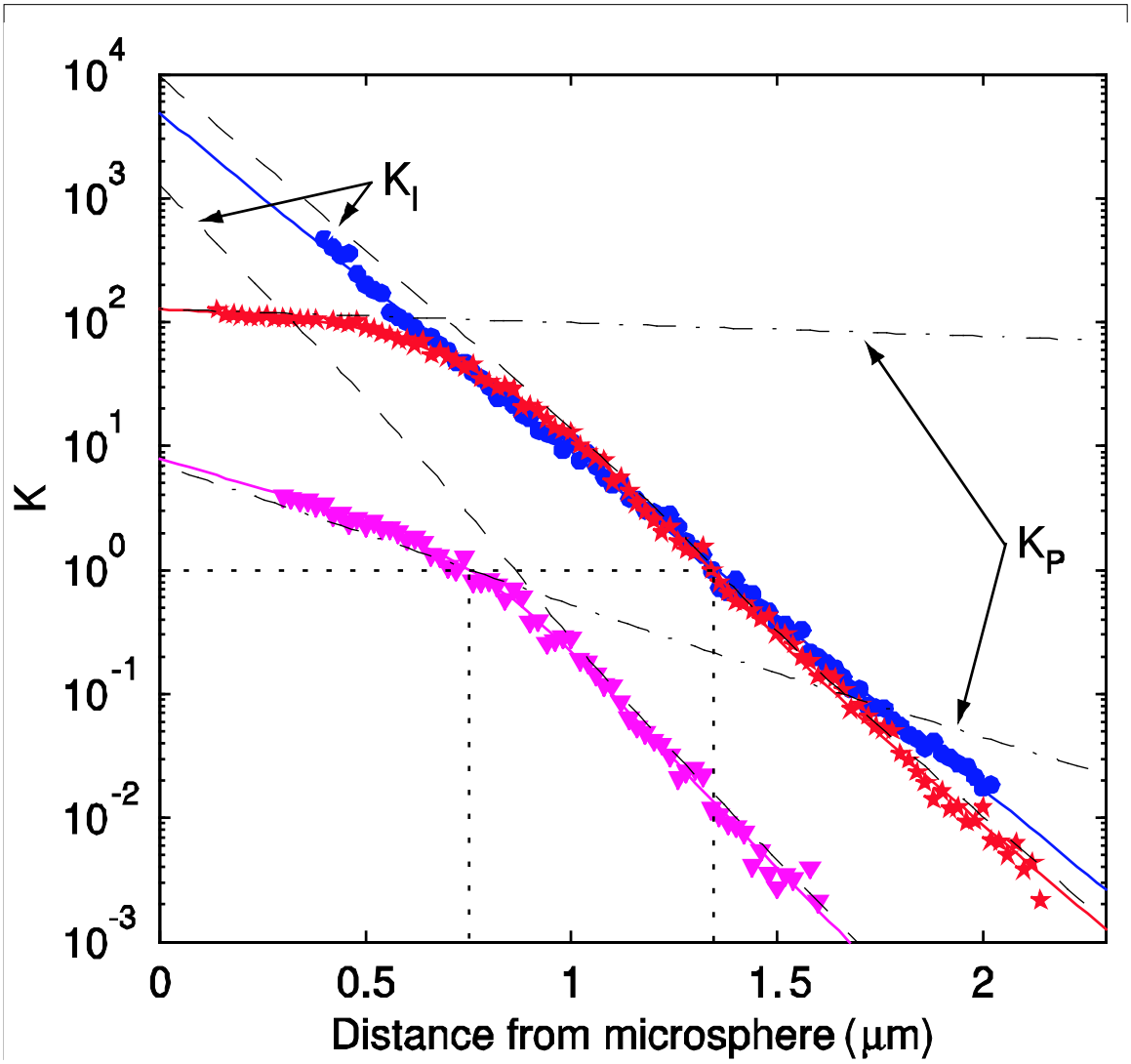

Figure 3.11: K versus position for various taper diameters for a 67-micron-diameter microsphere. The data represent taper diameters of approximately 1.2 micron (circles), 1.35 micron (stars), and 1.65 micron (triangles). Solid curves are fits using equation 3.22. The ideality at contact in the data (extrapolating fits to zero gap) is $> 99.98\%$, 99%, and 88%, respectively. Data show that for increased taper diameter higher-order-mode coupling causes a deviation from the ideal case (dashed line). The dash-dotted line represents K_P, which is related to ideality through equation 3.21. Dotted lines mark the critical coupling point.

lines), suggesting that a single higher-order mode is responsible for the observed roll-off of K with decreasing gap distance. As the number of modes supported for the two largest taper sizes is identical, the strong variation of the coupling data suggests that phase-matching is playing a significant role in determining the coupling behavior, resulting from the change of the taper-waveguide modes' propagation constant as taper diameter is varied.

The ideality of the coupler is determined by K_P through equation 3.21. Assuming the validity of the two-mode model, the dashed and dash-dotted lines in the figure give the K_I and K_P contributions to K, respectively. The 1.65 micron coupling data (triangles) show significant deviations from ideal coupling, with ideality ranging from 88% at microsphere-taper contact to 13% at a 1.5 micron gap. The 1.35 micron data (stars) exhibit less deviation, with ideality ranging from 99% at contact to 98% at a 2 micron gap. Finally, the data corresponding to the 1.2 micron taper diameter (circles) represent apparent ideal behavior over the range of separation gaps measured. The ideality at contact for this taper size is $> 99.98\%$ and it is not possible to infer a dependence with gap from the data. The influence of nonideality is clearly illustrated at the critical point (dotted lines). For high ideality the critical point in the data (given by the gap distance where $K = 1$) is identical to the gap separation where $K_I = 1$. The data show that this condition holds for the two smaller taper diameters. However, the critical point for the 1.65 micron taper diameter data is shifted towards a lower separation than K_I (0.1 micron shift of data from dashed line), as a result of the lower ideality (the large shift of 0.5 micron for K_I is mainly a result of phase-matching).

The data in figure 3.11 demonstrate that coupling (and ideality) vs. position behavior is very sensitive to the size of the waveguide. In order to further investigate the influence of taper waveguide diameter on the coupling behavior and ideality of the system, numerical calculations based on a modified coupled-mode theory [66] were performed. This model calculated the ideality based on coupling to the supported waveguide modes (i.e., it did not include radiation mode coupling). The results were in good agreement with the experimental data in figure 3.11 (values of K at contact and fundamental mode decay rates, i.e., slope of K_I, were within 10% of measured values). Finally, the degradation of ideality with increasing gap distance is a result of slower evanescent decay for higher-order taper modes.

Finally, by maximizing the value of K for near-contact gaps with a 2-micron-diameter

taper and using higher Q-factor microspheres ($Q > 10^8$ by measurement of linewidth in a 65-micron-diameter microsphere), it was possible to obtain even higher values for ideality in near-contact conditions (figure 3.12). The inset shows the transmission vs. separation data for this system, with a maximum over-coupled transmission of 99.95% (determined by using the exponential fit to K at zero gap). Numerical calculations (described above) show that the data slope is consistent with K_I. This agreement, combined with a very low radiation mode coupling power loss $< 0.05\%$ (using the fact that the overcoupled transmission drop from unity is due to intrinsic resonator loss and all other coupling-induced losses), demonstrates that the taper behaves as a nearly ideal coupler (higher-order mode coupling is not observable over the range of gaps measured). A lower bound of ideality of 99.97% is obtained if the lowest data point at contact is used. However, using a fit to the entire coupling data set (solid line) establishes a lower bound on ideality at contact of 99.99%.

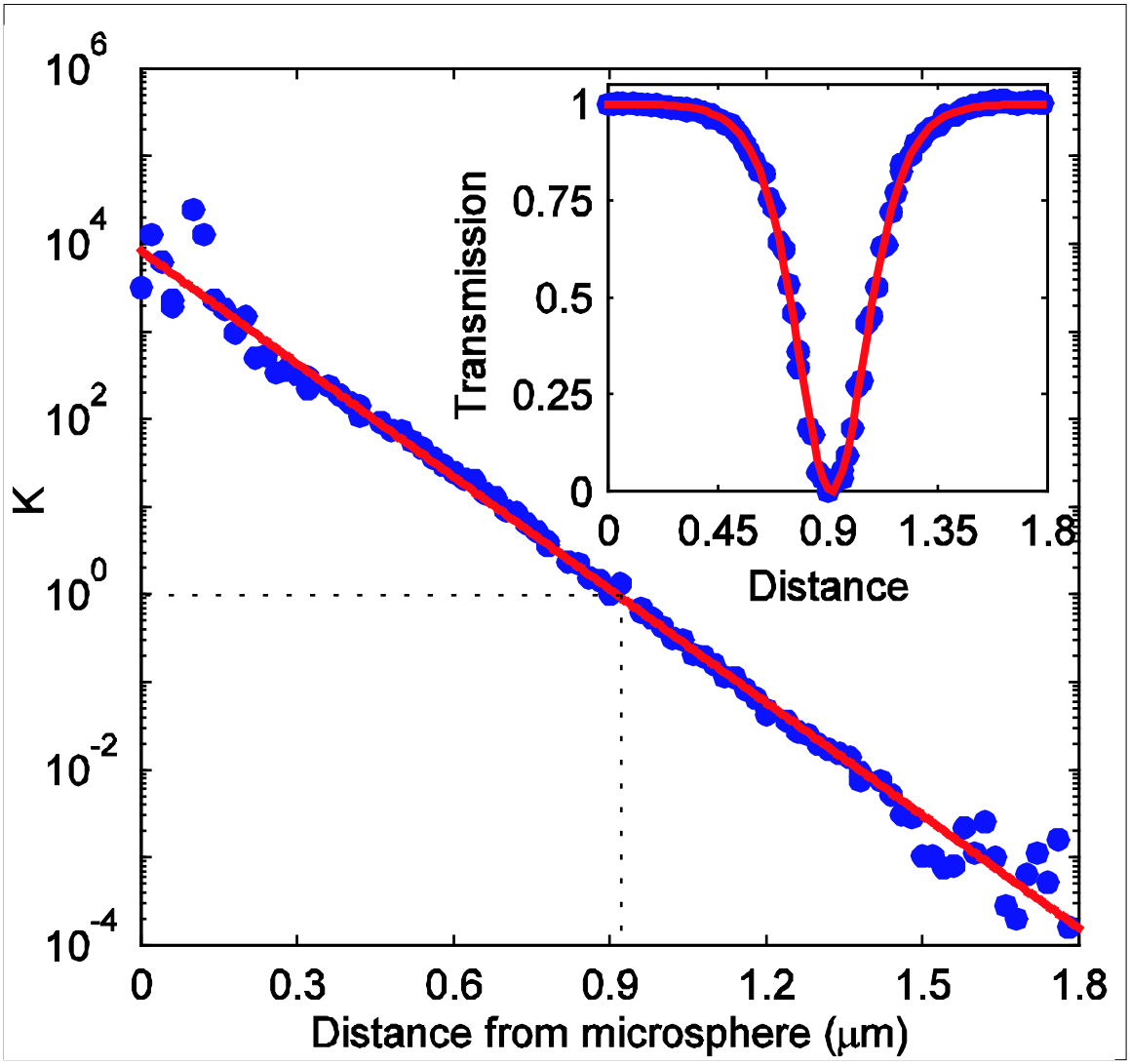

Figure 3.12: Coupling parameter K versus taper-sphere separation for a 65-micron-diameter microsphere. The data show a linear relation between $\ln K$ and x, with a least squares fit (solid line). Ideality inferred at contact is greater than 99.99%. The dotted line marks the critical coupling point ($K = 1$ at $x = 0.91$ micron). The inset shows transmission versus position data.

3.5 Numerical investigations of ideality

The previous section has shown that it is possible to obtain extremely efficient coupling between a fiber-taper and a high-Q resonator [21], such that any influence of higher-order mode coupling and radiation mode coupling can be ignored. However, the experimental data has also shown that this is more the exception, as most choices of waveguide geometry introduce parasitic mode coupling. In order to obtain further insight into the conditions required for high ideality coupling, numerical calculations based on the modified coupled mode theory presented in section 3.2.2 were performed.

As discussed previously, optimal coupling occurs when the waveguide and resonator are phase-matched [67]. Thus, it is important to investigate the ideality possible with optimal coupling. Figure 3.13 shows the expected ideality at waveguide/resonator contact for phase-matched coupling between a fiber-taper and the fundamental TM polarized modes of a silica microsphere. The data indicate that the ideality is dramatically higher when using the exact phase-matching condition, as a result of the smaller fiber diameter required. This results in a larger propagation constant separation between the fundamental and next higher-order fiber mode, leading to the enhanced coupling fidelity. Furthermore, as this calculation only corresponds to the ideality at fiber-sphere contact, this is a best-case scenario. Not only does this mean that the ideality is extremely dependent on the choice of phase-matching condition, but that even if optimally phase-matched, larger diameter resonators inherently have lower ideality. This strong dependence on ideality with proper choice of phase-matching condition holds for all cases. As such, in the rest of this section I will consider only cases where the microsphere and fiber are phase-matched using the exact condition given by equation 3.14. Now, the data in figure 3.13 indicate that even if optimally phase-matched, ideality is not necessary high, at least for TM polarized modes of larger diameter spheres. Figure 3.14 shows the ideality expected for both TM and TE fundamental microsphere modes optimally phase-matched near 1550 nm. The figure shows that the TE modes possess a significantly lower ideality for a given resonator diameter. As often TE polarized modes are desirable for practical applications (they possess higher quality factors and smaller modal volumes) such as lasing and nonlinear optics, this result means that careful consideration must be given to the proper operating point. This figure indicates that no matter which polarization is chosen,

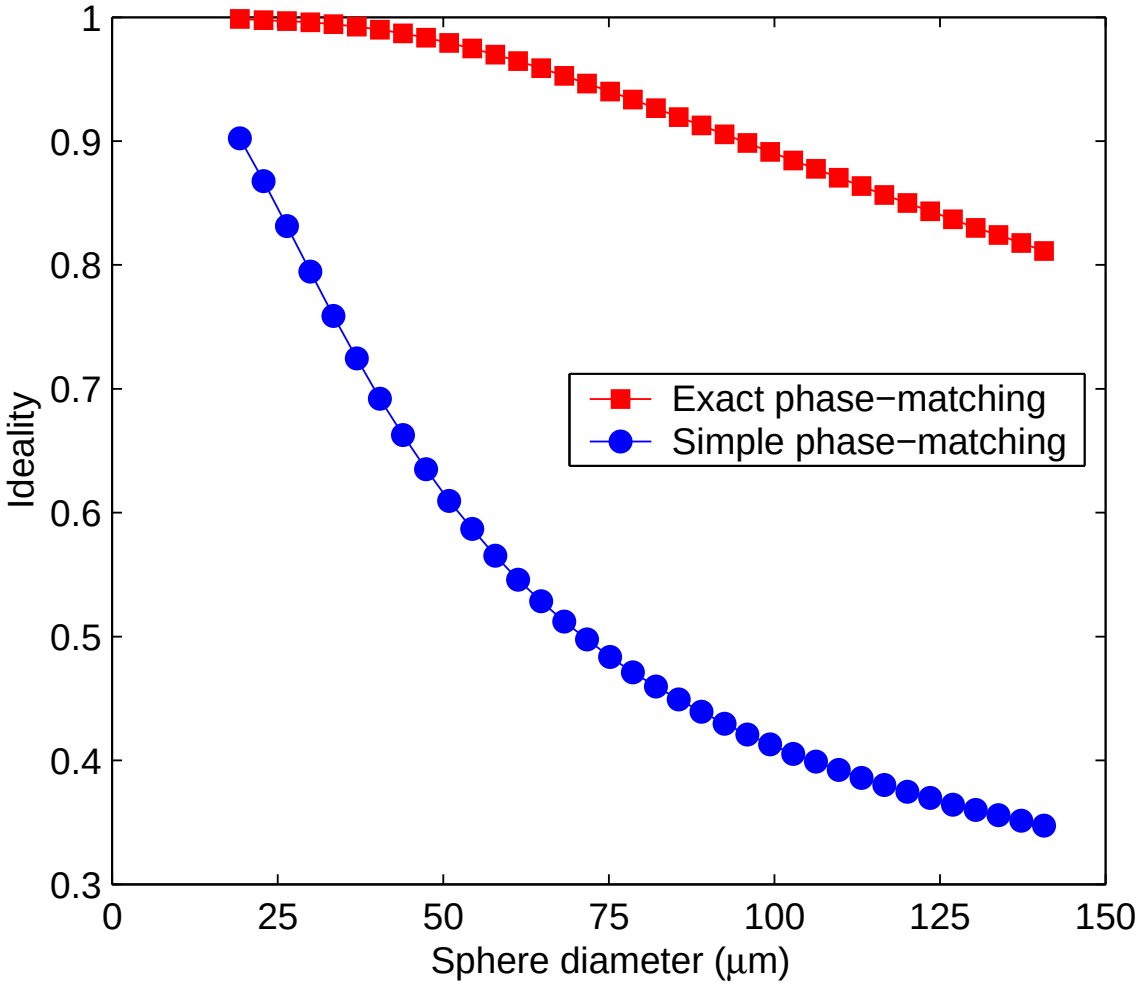

Figure 3.13: Comparison of the simple and exact phase-matched ideality for a fiber-taper microsphere system. The 60-micron-diameter microsphere with a TM polarized fundamental mode at 1550 nm was used. The data show that clearly the use of the correct phase-matching relation is essential for high ideality, especially for larger diameter resonators.

for phase-matched excitation ideality is at best modest. As this is the maximum obtainable value, operation at a more useful point such as critical coupling will by necessity result in a large loss of optical energy into higher-order fiber modes.

However, choice of a higher-order radial WGM may be able to overcome this drawback, as a result of the lower propagation constants of $n > 1$ modes and the corresponding smaller fiber diameters needed for phase-matching. Figure 3.15 shows the calculated ideality for both the fundamental $n = 1$ and the next higher order radial WGM ($n = 2$). The data indicate that there is a significant increase of ideality for nonfundamental WGM's, such that for all intensive purposes the parasitic coupling is negligible. This fact is reflected in the experimental results where for nearly phase-matched excitation complete overcoupling was obtained only for higher-order radial modes, such as presented previously (which corresponded to a $n = 3$ WGM).

Lastly, I might mention that while the experimental and numerical results presented in this chapter were specific to silica microspheres, toroidal resonators can also be studied. Due to the fact that for high aspect ratio structures the azimuthal mode number of the optical mode is reduced for a fixed wavelength (see section 2.3.2), the propagation constant is also reduced relative to a sphere. This means that the optimal phase-matching point occurs for a smaller fiber diameter, which directly correlates to a much higher ideality. Thus these structures have the potential to obtain high idealities and high coupling efficiencies to the fundamental cavity mode, which is very exciting for investigation of nonlinear and quantum optic effects. These topics will be discussed in Chapters 4 and 5.

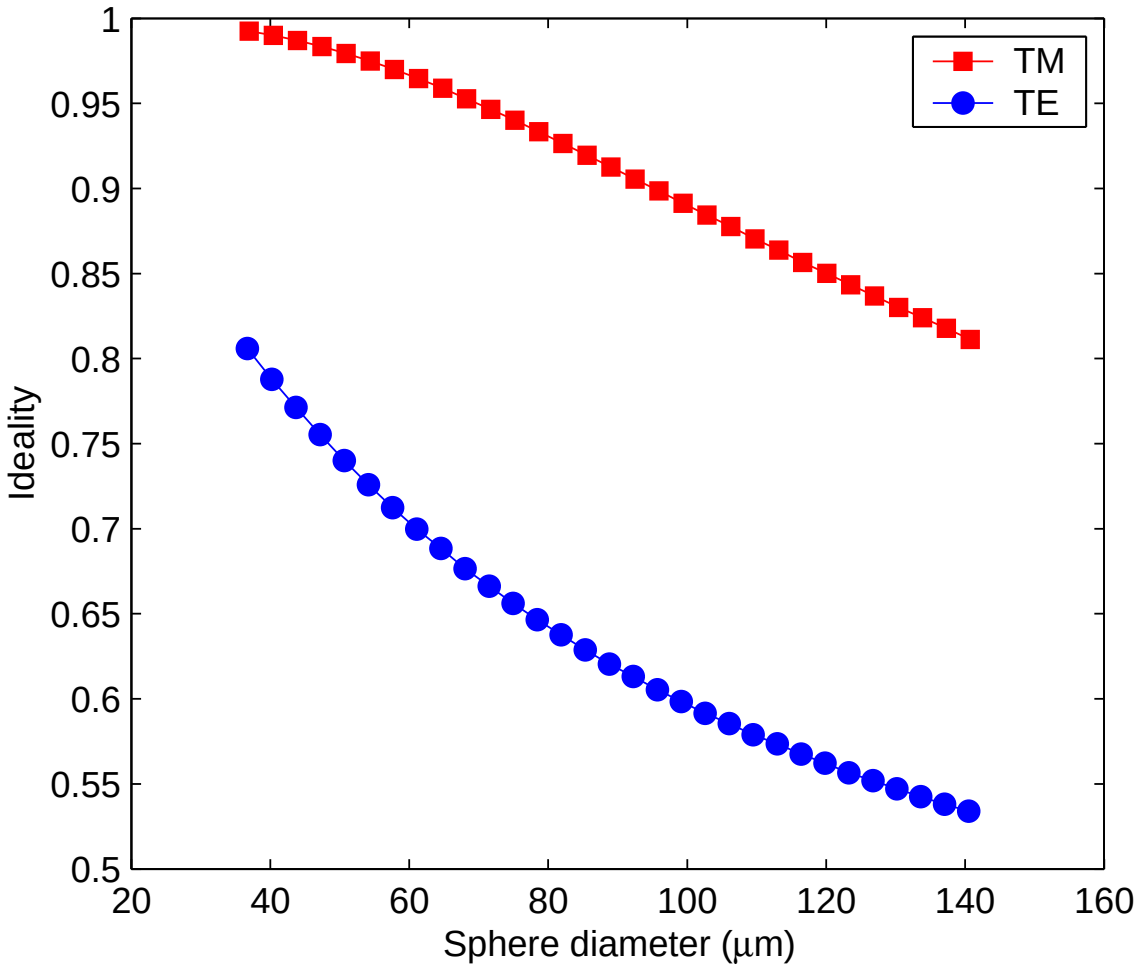

Figure 3.14: Ideality versus polarization for a fiber-taper optimally phase-matched to a silica microsphere. The data indicate that TE modes possess significantly reduced ideality, especially for larger diameter microspheres.

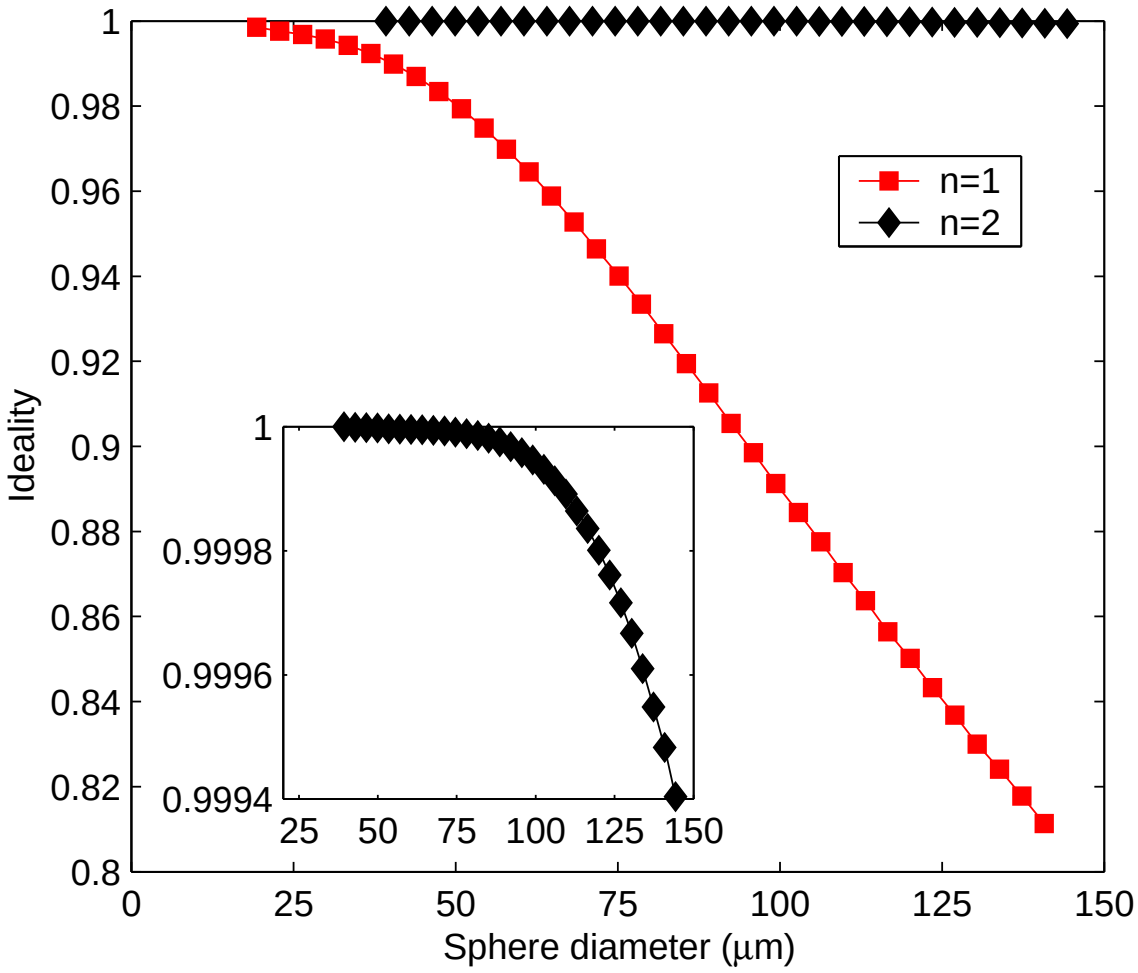

Figure 3.15: Calculated ideality versus microsphere diameter for both the fundamental and first higher-order radial WGM. The data show that by moving to a higher-order WGM the ideality is dramatically increased, as a result of the much smaller fiber diameters necessary for phase-matching.

Chapter 4

Nonlinear optics in high-Q microcavities

One of the great promises of extremely low loss micro-scale optical resonators is to create compact laser sources. While much work has investigated lasing in such structures, with both experimental [71, 72] and theoretical studies [14, 73, 74], the realization of nonlinear effects has been much more scarce. Up until the work in this thesis, nonlinear wave generation has only been observed in highly nonlinear liquid microdroplets [8, 9]. As explained earlier, UHQ microresonators can build up extremely large circulating intensities with modest continuous-wave pump powers, thus creating the possibility of nonlinear wave generation in a weakly-nonlinear material such as silica at threshold power levels many times lower than other techniques. In this chapter, I will present a simple model for third-order nonlinear effects [11] in a microresonator and show that low-threshold stimulated Raman scattering and Parametric oscillation are possible. Lastly, experimental confirmation will be presented. This chapter will not consider simulated Brillouin scattering (SBS), as the narrow gain bandwidth (100 MHz) makes the overlap of high-Q microcavity modes with the Brillouin gain spectrum unlikely [10].

4.1 Theory of stimulated Raman scattering in microcavities

Stimulated Raman scattering (SRS) in a nonlinear cavity can be analyzed by using a simple harmonic oscillator model analogous to that done for the passive cavity in Chapter 3 by accounting for all sources of excitation (now including the pump intensity-dependent Raman gain) and loss for both the pump and nonlinearly generated Raman waves. Thus, the new

differential equations for the coupled pump and Raman modes amplitudes are given by

$$\begin{aligned}\frac{dE_P}{dt} &= -\frac{1}{2}\left(\frac{1}{\tau_{ex}}+\frac{1}{\tau_0}\right)_p E_P - \frac{\lambda_R}{\lambda_P} g_R^c(\lambda_P,\lambda_R)\cdot|E_R|^2 E_P + \kappa_{ex,P} s \\ \frac{dE_R}{dt} &= -\frac{1}{2}\left(\frac{1}{\tau_{ex}}+\frac{1}{\tau_0}\right)_R E_R + g_R^c(\lambda_P,\lambda_R)\cdot|E_P|^2 E_R\end{aligned} \tag{4.1}$$

In these expressions both the excitation and emitted wave are assumed to be on resonance. E_P and E_R represents the amplitude of the pump and Raman waves with wavelengths λ_P and λ_R, respectively. The Raman generated wave is created from the power in the pump mode by the second term in the first equation, where $g_R^c(\lambda_P,\lambda_R)$ denotes the Raman gain coefficient in the cavity. The pump mode is excited by an input wave s with coupling amplitude $\kappa_{ex,P}$, and loses energy to the Raman wave such that the total cavity energy is conserved. The excitation wave coupling coefficient $\kappa_{ex,P}$ is related to the external coupling lifetime of the cavity by $\kappa_{ex,P} = \sqrt{\frac{1}{\tau_{ex}^P}}$, such that the total cavity lifetime is given by $\frac{1}{\tau} = \frac{1}{\tau_{ex}} + \frac{1}{\tau_0}$.

The internal cavity Raman gain coefficient g_R^c is given in terms of the bulk Raman gain coefficient g_R (maximum Raman gain for silica is $\approx 6.5\times10^{-14}$ m/W at a wavelength of 1550 nm, with the gain scaling inversely with wavelength) through the relation,

$$g_r^c(\lambda_P,\lambda_R) \equiv \frac{c^2}{2n_R n_P}\frac{f}{V_{eff}^{NL}} g_R(\lambda_P,\lambda_R) \text{ and } f = \frac{\int|E_P|^4|E_R|^4 dA}{\int|E_P|^4 dA\int|E_R|^4 dA} \tag{4.2}$$

where V_{eff}^{NL} defines an effective nonlinear modal volume of the pump mode, f gives the spatial overlap between the pump and Raman mode, and n_P (n_R) are the effective indices of the pump (Raman) modes.

The Raman threshold is obtained by solving equation 4.1 assuming steady-state behavior (this holds for the experiments in this thesis, which are quasi-continuous wave), which gives

$$P_{threshold} = C(\Gamma)\frac{\pi^2 n_P n_R}{\lambda_P\lambda_R f g_R} V_{eff}^{NL}\left(\frac{1}{Q_0}\right)_P\left(\frac{1}{Q_0}\right)_R \frac{(1+K_P)^2}{K_P}(1+K_R) \tag{4.3}$$

Q_0 denotes the intrinsic quality factor of the pump and Raman modes, with the associated coupling parameter K [1]. The reduction of circulating power due to backscattering is also accounted for in this equation through the parameter $C(\Gamma)$, which takes a value in the range

[1] The pump mode total coupling parameter is denoted as K_P, which is not the parasitic coupling parameter discussed in Chapter 3.

1 to 2 (unity for no backscattering and two for a full standing wave).

The Raman threshold scales approximately as V_{eff}^{NL}/Q_0^2, which clearly demonstrates the crucial need for UHQ resonators to obtain ultra-low threshold Raman oscillation. This strong dependence on quality factor is why nonlinear optics in UHQ microcavity sources is so promising.

Figure 4.1 shows the dependence of the Raman threshold as a function of the coupling parameter K for a 50-micron-diameter resonator with an intrinsic quality factor of $Q_0 = 10^8$. Threshold values below 100 microwatts are possible, provided the resonator system is operated in the proper coupling regime. Investigation of the minimum Raman threshold under the assumption of equal coupling parameters for the pump and Raman modes (which is close in practice), shows that it occurs for a coupling parameter $K = 1/2$, which corresponds to a waveguide pump transmission of $T = 1/9$ ($\sim$11%) in the undercoupled regime. This point does not occur at the maximum gain (which is at critical-coupling) due to the interplay between the pump Raman gain and the Raman mode cavity loss. Because the Raman gain peaks at the critical point but the cavity loss is a monotonically increasing function of coupling, the optimal point must occur undercoupled. At this point, the Raman threshold is given by

$$P_{threshold}^{min} = \frac{27}{4} \cdot C(\Gamma) \frac{\pi^2 n_P n_R}{f g_R \lambda_p \lambda_R} V_{eff}^{NL} \left(\frac{1}{Q_0} \right)^2 \tag{4.4}$$

Upon the onset of stimulated emission, the cavity pump field is clamped at its threshold value. Thus, the Raman field inside the cavity can be determined by solving equation 4.1 for the term $|E_R|^2$, using the threshold value for E_P. Relating the intracavity pump field E_P to the threshold incident power P_t through the cavity buildup factor, and using the fact that the Raman output power is given by $P_R = \kappa_R^2 \cdot |E_R|^2$, we obtain

$$P_{Raman} = 4 \frac{\lambda_P}{\lambda_R} (1 + K_R^{-1})^{-1} (1 + K_P^{-1})^{-1} P_{threshold} \left(\sqrt{\frac{P}{P_{threshold}}} - 1 \right) \tag{4.5}$$

This formula illustrates that the Raman output power has a square-root dependence on the input power above threshold. The nonlinear behavior is a result of the dependence of the amount of power coupled into the cavity on the amount of Raman power generated. As the SRS emitted power is increased, the overall resonator loss of the cavity pump mode

increases, which for a given coupling configuration reduces the pump coupling parameter K_P. Hence, the transmission of the pump mode through the waveguide changes in accordance with $T = ((1 - K_P)/(1 + K_P))^2$. For example, a resonator biased such that the pump mode is critically-coupled below threshold will move progressively undercoupled as the pump power is increased past the Raman threshold. Figure 4.2 shows the SRS output power as a function of both coupling parameter and incident waveguide power. In this graph, the numerical results are only shown for regimes where first-order SRS is present. In particular, when the pump power is 4 times the threshold of first-order SRS, second-order SRS occurs and clamps the SRS first-order output. Thus there is a very small range of pump powers where only first order SRS is present and high output power is obtained. The graph shows that the maximum output power appears overcoupled ($T \sim 60\%$), with high input powers much above the minimum threshold value. This is expected as operation in the overcoupled regime not only means the dominant loss is due to output coupling (which is considered useful), but since the initial threshold is higher the amount of power available for output is also higher before second-order SRS occurs.

While the threshold and output power are obviously important, lasers are also characterized on their differential efficiency, which gives the fraction of pump power above threshold converted into the emission band. The external differential efficiency of the Raman output is given by

$$\eta_{ex} \equiv \frac{dP_{Raman}}{dP} = 2\frac{\lambda_P}{\lambda_R}(1 + K_R^{-1})^{-1}(1 + K_P^{-1})^{-1}\sqrt{\frac{P_{threshold}}{P}} \tag{4.6}$$

Inspection of this equation shows a number of things. First, the efficiency decreases as the laser pump is increased past threshold. This is due to the square-root dependence of the Raman output as a consequence of the coupling of absorbed power with Raman output as discussed above. This is somewhat discouraging, as ideally one desires to operate a laser far above threshold in order to increase both output power and stability. While this decrease in efficiency is relatively slow (inverse square root), the presence of ultralow thresholds causes a slight dilemma. With threshold powers of approximately 100 microwatts as commonly obtained in the following sections, the Raman efficiency for an output of only 400 microwatts is half of that at threshold. To further illustrate this point, figure 4.3 shows the theoretical external differential efficiency for a 50 micron diameter resonator operated with an intrinsic

quality factor of $Q_0 = 10^8$. The data indicate that while thresholds below 100 microwatts are readily possible, at this coupling parameter the external differential efficiency is relatively low ($<\sim 0.5$). Operation in the overcoupled regime, on the other hand, allows much higher efficiency (> 1).

The external efficiency behavior also shows that there is a strong dependence on the coupling parameters K for both the pump and Raman modes. At critical coupling the efficiency is 50%, where for completely overcoupled the efficiency approaches 200%. This value is double the value expected upon casual inspection, which is a result of the fact that again the pump absorbance is coupled to the Raman output. A calculation based on the internal cavity differential efficiency gives the expected maximum of 100%.

While maximizing the external differential efficiency is obviously important, the absolute conversion efficiency (Raman power output to incident pump power) is often of interest, as this determines the total light-out to light-in efficiency of a laser source. Figure 4.4 gives a theoretical prediction of the absolute conversion efficiency for a high intrinsic Q ($Q_0 = 10^8$), 50-micron-diameter microcavity as a function of coupling parameter and input power. The calculations indicate that the absolute conversion efficiency for first-order SRS is always relatively low when operating near the point of lowest threshold ($<\sim 50\%$). This is a result of the fact that the low-threshold operation occurs near the critical point, where a large fraction of the circulating power is lost (absorbed and/or scattered) by the cavity itself. Operation in the overcoupled regime allows the dominant loss to be output coupling instead of resonator loss, thus allowing optimal extraction of the SRS generated energy. This behavior is clearly seen in figure 4.4, where absolute efficiencies approaching 75% are possible for overcoupled operation with an incident pump power of 2 mW, even though the SRS threshold of 600 microwatts is significantly higher than that of the absolute minimum (by a factor of 10).

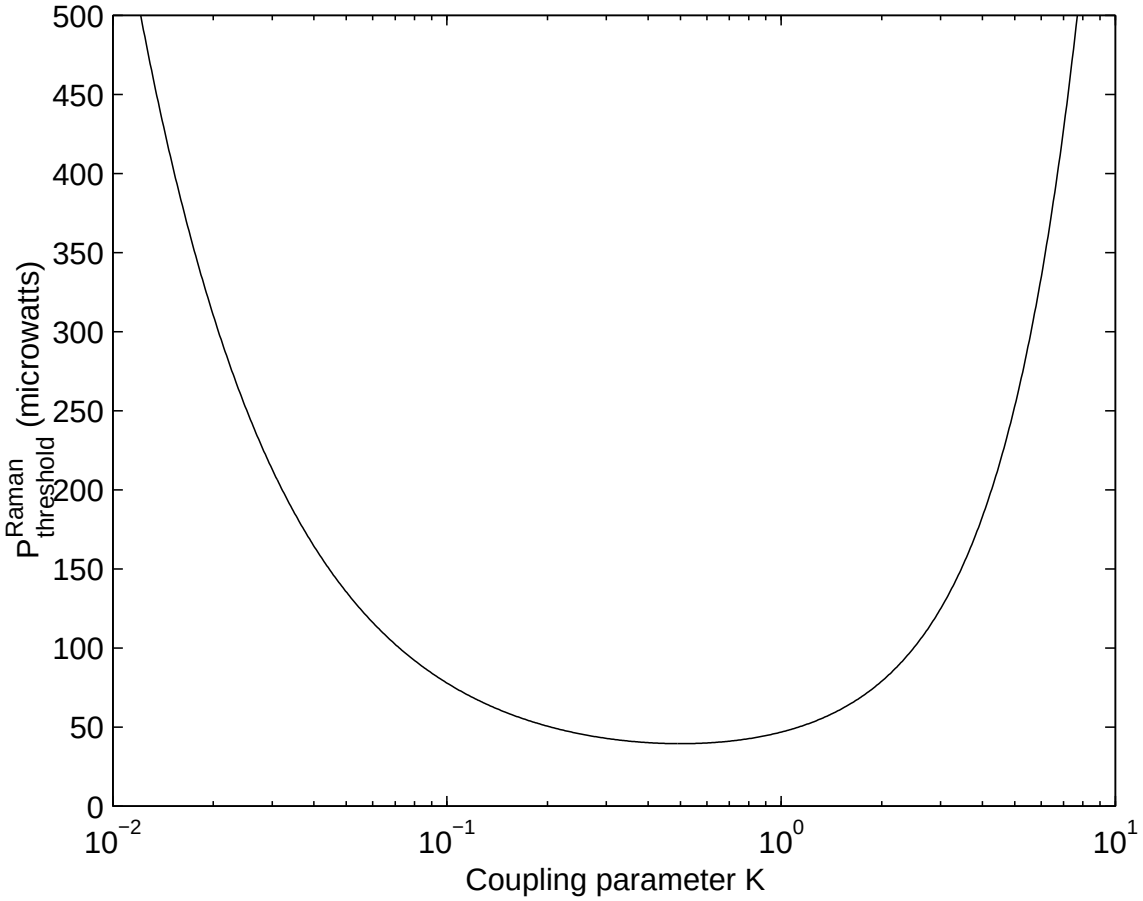

Figure 4.1: Threshold versus coupling parameter for first-order stimulated Raman scattering for a 50-micron-diameter resonator at 1550 nm. The predicted SRS threshold for an intrinsic quality factor of $Q_0 = 10^8$ has a minimum of 45 microwatts at $K = 1/2$ ($T = 11\%$ undercoupled).

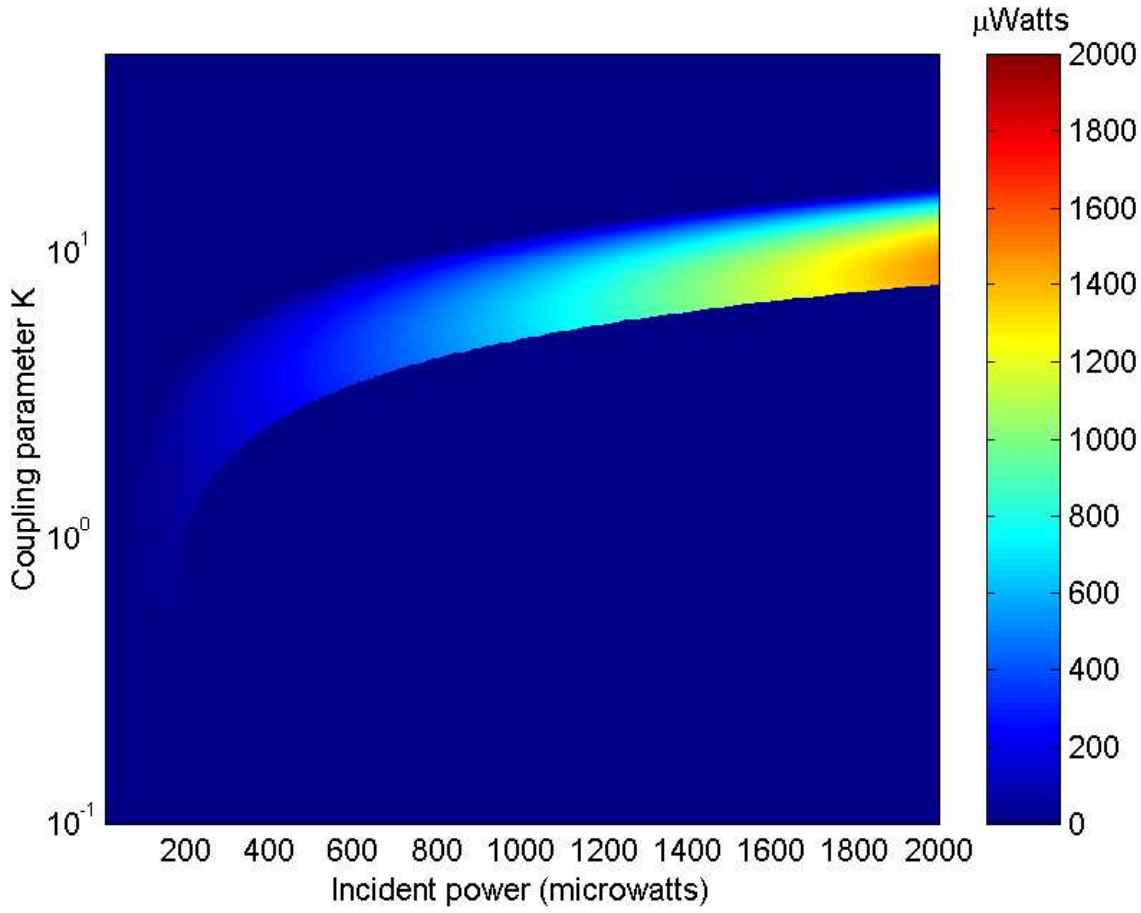

Figure 4.2: SRS output power versus input power and coupling parameter. The calculations correspond to a 50-micron-diameter resonator with an intrinsic quality factor of $Q_0 = 10^8$. The numerical results indicate the output power when first-order SRS is present. The highest output power occurs around $K = 10$ ($T \sim 67\%$ overcoupled).

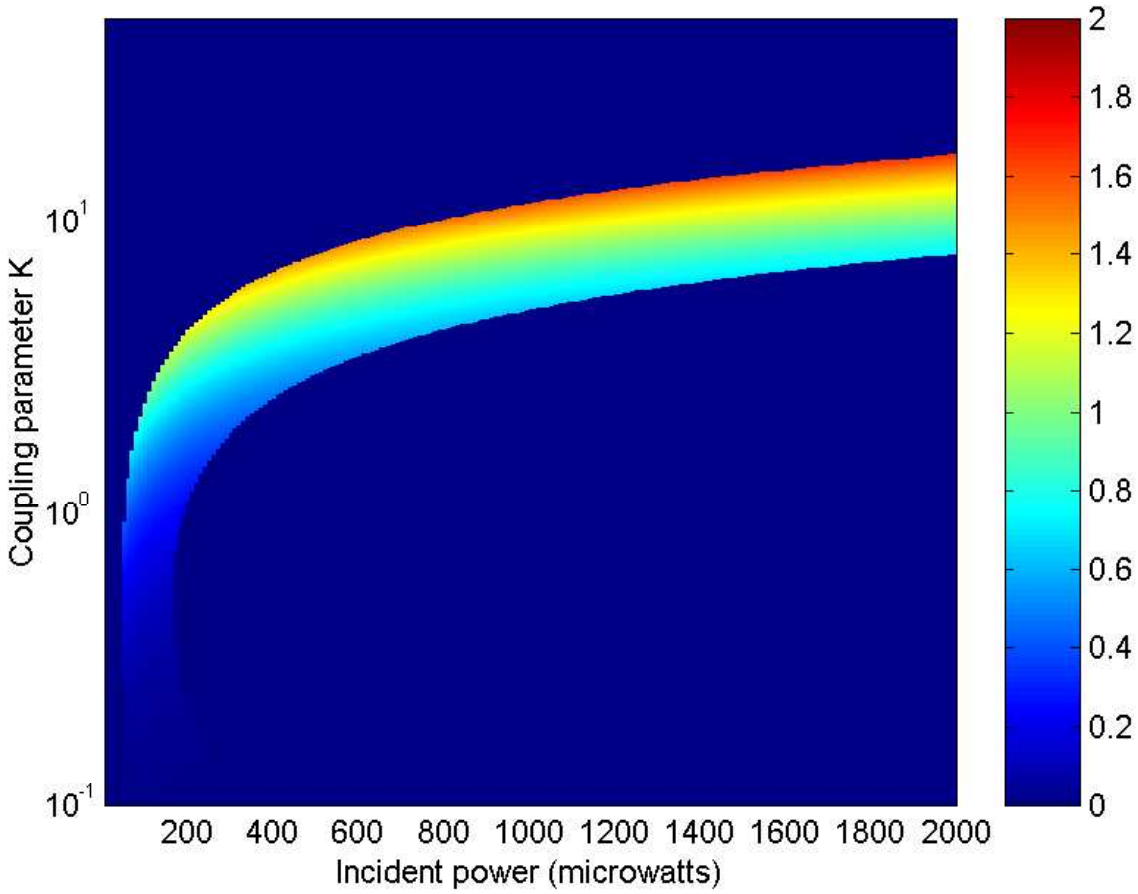

Figure 4.3: SRS external differential efficiency versus input power and coupling parameter. The calculations correspond to a 50-micron-diameter resonator with an intrinsic quality factor of $Q_0 = 10^8$. The numerical results indicate the external differential efficiency when first-order SRS is present. The highest external differential efficiency occurs both near threshold and strongly overcoupled, approaching the limiting value of $2\lambda_P/\lambda_R$.

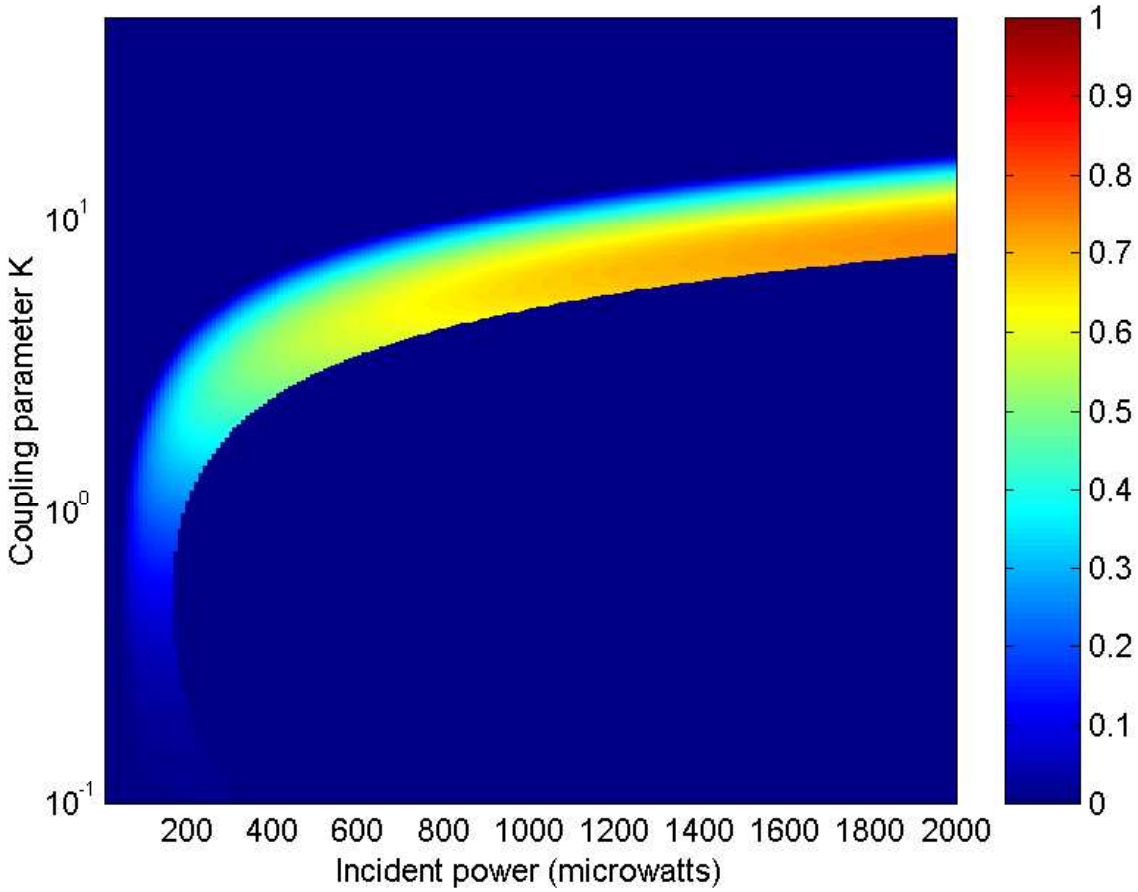

Figure 4.4: SRS absolute conversion efficiency versus input power and coupling parameter. The calculations correspond to a 50-micron-diameter resonator with an intrinsic quality factor of $Q_0 = 10^8$. The numerical results indicate the power conversion efficiency when first-order SRS is present. The highest conversion occurs overcoupled, with an overall efficiency of approximately 75% for an incident power of 2 mW (threshold occurs near 600 microwatts for this coupling parameter).

4.2 Theory of parametric oscillation in microcavities

Parametric oscillation is an energy conserving process which converts two pump photons into a red-shifted signal and a blue-shifted idler photon. In this section, I will investigate the conditions under which parametric oscillation is expected to occur in a microcavity. This analysis will deal only with the degenerate pump case, where a single pump wave is converted into a signal and idler wave located symmetrically around the pump. In this case, the parametric threshold can be obtained in a simple manner, by equating parametric gain with the signal (or idler) loss [11, 75].

The parametric gain is given by

$$g = \sqrt{((\gamma P_{cavity})^2 - (\kappa/2)^2)}$$

with

$$\kappa = n_{eff}\Delta\omega/c + 2\gamma P_{cavity} \text{ and } \Delta\omega = 2\omega_P - \omega_S - \omega_I$$

Here n_{eff} represents the modal effective index (assumed to be identical for each mode), P_{cavity} is the circulating cavity power, and γ represents the nonlinear parameter. The nonlinear coefficient $\gamma = \frac{\omega}{c} \cdot \frac{n_2}{A_{eff}^{NL}}$ is composed of the optical frequency ω, the Kerr nonlinear gain coefficient ($n_2 \approx 2.2 \times 10^{-20} m^2/W$ for silica), and the effective nonlinear cross-sectional area A_{eff}^{NL}. The initial cavity resonance detuning is given by $\Delta\omega$. In this expression κ represents the total detuning of the cavity, composed of both the intrinsic cavity detuning $\Delta\omega$, and the induced detuning through self and cross phase modulation $2\gamma P_{cavity}$.

Inspection shows that parametric gain can only occur for a certain range of intrinsic cavity detunings, which can be shown to be

$$0 < \Delta\omega < \Omega \text{ where } \Omega = 4 \cdot \frac{c}{n}\gamma P_{cavity}$$

Here, Ω represents the parametric gain bandwidth, which indicates the maximum amount of intrinsic cavity detuning that can be overcome by the parametric process.

Equating the parametric gain to the loss $\alpha = n\omega/(cQ)$, we obtain the parametric oscillation

threshold,

$$P_t^{Kerr} = \frac{n_{eff}}{c}\frac{\omega_0^2 Q_0^{-2}(1+K)^2 + (\Delta\omega/2)^2}{\gamma\Delta\omega}\frac{\pi^2 R n_{eff}}{C(\Gamma)\lambda_0}\frac{(K+1)^2}{Q_0 K} \tag{4.7}$$

where all the parameters have been defined previously in this thesis. Here the cavity build-up factor was used to convert the cavity threshold power to the incident waveguide threshold power. In this analysis both the pump and signal/idler waves were assumed to have equal cavity losses and effective indices, and the pump overlap with both the signal and idler waves were taken to be unity. Note that this equation also scales as V_{eff}^{NL}/Q_0^2, due to the dependence of γ on cavity circulating power. Figure 4.5 shows the calculated parametric threshold as a function of coupling parameter and intrinsic cavity frequency detuning for a 50-micron-diameter resonator with an intrinsic quality factor of $Q_0 = 10^8$ for a pump wavelength of 1550 nm. The data indicate that parametric oscillation is possible over a wide range of frequency detunings and coupling parameters, with an absolute global minimum value of 27 microwatts occurring undercoupled with a small frequency detuning. As discussed in the previous section on SRS in microcavities, this optimal point is undercoupled with slight waveguide pump transmission ($T \sim 11\%$).

Comparison of the minimum parametric oscillation threshold with the SRS oscillation threshold shows that parametric oscillation has an approximately 2 times lower threshold than SRS in a cavity. However, the actual parametric threshold value is dependent on the cavity mode frequency detuning, whereas the SRS threshold is not. Thus, for a specific range of frequency detunings, parametric oscillation is present, while for larger values SRS occurs. This implies that pure parametric oscillation is not possible over the wide range of coupling and frequency detunings indicated in figure 4.5, which as will be seen later greatly restricts the experimental observation of pure parametric oscillation in a microcavity. This competition between parametric and Raman oscillation can be accounted for by investigating the conditions under which pure parametric oscillation has a lower threshold than Raman oscillation. Figure 4.6 shows the results of this analysis for the same resonator characteristics discussed previously. The numerical results now indicate a severe reduction of the frequency detunings under which pure parametric oscillation can occur, resulting in a very specific range of detunings around the minimum threshold point (range is less than approximately 10 MHz). This value is very hard to achieve in practice with a true microcavity design, as the longitudinal mode spacing is

typically >10 nm (1.2 THz). The situation is improved somewhat for overcoupled operation, as the frequency range is relaxed.

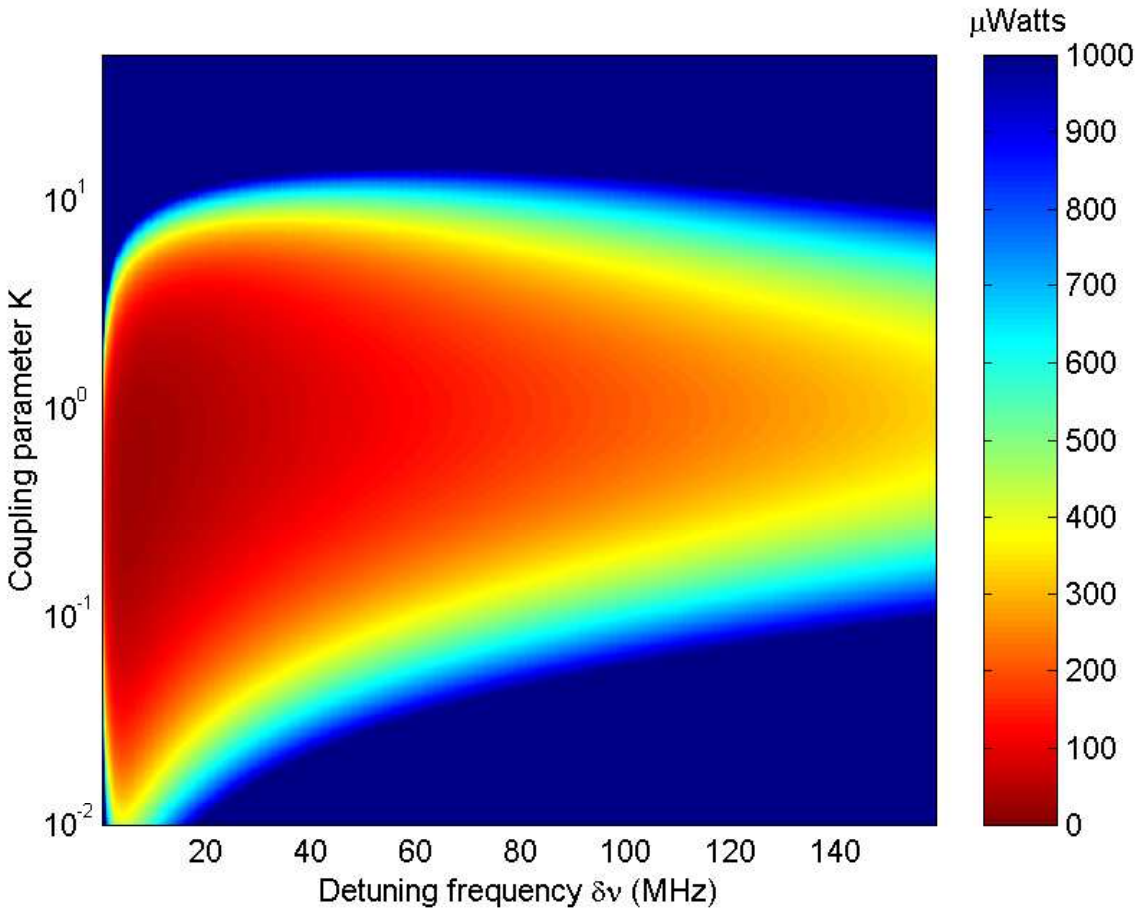

Figure 4.5: Parametric oscillation threshold as a function of frequency detuning and coupling parameter for a 50-micron-diameter resonator with an intrinsic quality factor of $Q_0 = 10^8$. The minimum threshold of 27 microwatts occurs undercoupled ($K = 1/2$) with a frequency detuning of ~ 5 MHz.

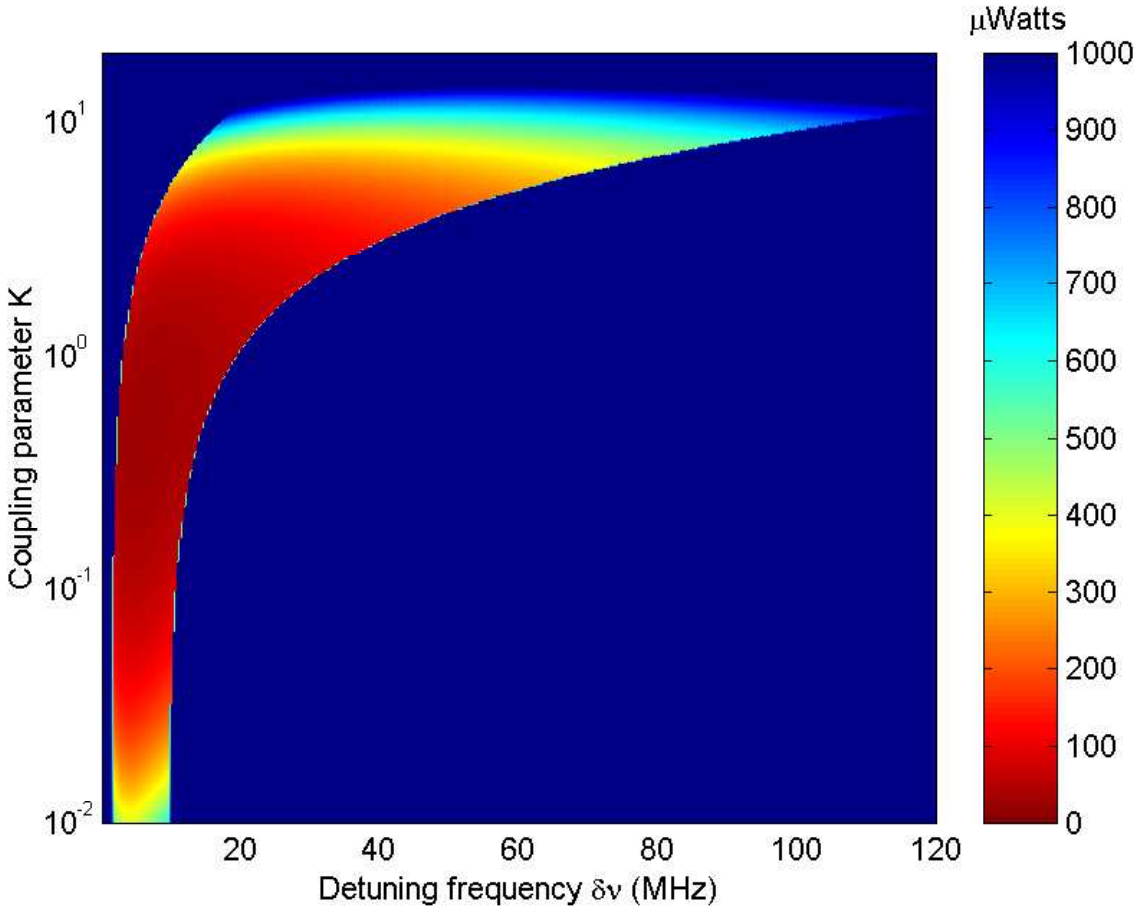

Figure 4.6: Parametric oscillation regime as a function of frequency detuning and coupling parameter for a 50-micron-diameter resonator with an intrinsic quality factor of $Q_0 = 10^8$. Parametric oscillation is possible only for a very specific range of frequency detunings, especially in the low-threshold undercoupled regime. For larger detuning values SRS is present with a higher threshold. The parametric threshold is indicated in microwatts.

4.3 Experimental observations of optical nonlinear effects

The previous section has shown that low-threshold nonlinear optics is theoretically possible in ultra-high-Q microcavities. Predicted thresholds below 100 microwatts can be obtained in silica microcavities with an intrinsic quality factor of 1×10^8. It is this dramatic possible decrease in nonlinear thresholds that has spurred much investigation into very high Q silica microresonators. However, until the work I will describe in this thesis there has been no experimental demonstration of nonlinear optical effects (except for a study of the evidence of the Kerr effect in a low temperature microsphere [16]) in a silica microcavity, although there has been over 10 years of work on silica microspheres. This is somewhat striking, as for quite some time quality factors exceeding 10^9 were readily obtained, which predicts sub-microwatt SRS and parametric oscillation thresholds. Thoughts on this situation reveal that the lack of nonlinear oscillation cannot result from the microcavity itself, as they are identical or even superior to those fabricated in this work. Thus, the only resulting influence is the excitation of the microcavity. Previous methods of microcavity excitation have suffered from rather low efficiency, as manifested by the inability to obtain true critical coupling. This means that a fraction of the incident energy is wasted, which can be quite significant. In fact, it is the ability to completely couple all incident power into the microcavity using fiber-taper waveguides that has allowed large resonant buildups of circulating cavity power (and thus intensity) with modest pump powers, such that the nonlinear thresholds can be exceeded.

In order to experimentally investigate nonlinear wave generation in silica microcavities, the same experimental apparatus used to investigate the coupling properties of a fiber-taper/microcavity system was employed. The only difference is the addition of optical spectrum analyzers on both the forward and backwards direction to monitor the transmitted spectrum. This was done by splitting the optical output by use of a 50/50 coupler in the forward and the backwards direction, with one output directed to the OSA and the other to a photodiode to monitor the pump transmission. While this allowed a fraction of any nonlinear generated power to also be detected in the photodiode, the effect on the monitored pump transmission was in general small, since overall conversion efficiencies were typically $< 20\%$. Additionally, for higher power exci-

tation studies an erbium-doped fiber amplifier was used to boost the incoming optical power up to approximately 30 mW.

4.3.1 Stimulated Raman scattering in silica microspheres

Figure 4.7 shows the emission spectrum for a Raman microsphere laser (intrinsic pump quality factor of $Q_0 = 10^8$) excited far above the threshold for stimulated Raman scattering. There are a multitude of nonlinearly generated wavelengths, from stimulated Raman peaks centered around 1670 nm to Raman-assisted four-wave mixing (FWM) peaks located symmetrically about the 1550 nm pump. Stimulated Raman scattering (SRS) has a very high threshold (nonlinear gain coefficient of 10^{-11} cm/W [76]), requiring significant circulating pump powers. This suggests that other nonlinear processes having lower thresholds such as stimulated Brillouin scattering (SBS) could also be present in the systems tested. SBS, for example, should have a threshold roughly 500 times lower than stimulated Raman scattering (nonlinear gain coefficient is 500 times larger). To determine the presence of SBS, an optical spectrum analyzer was used to measure backward propagating optical power coupled from the microresonator into the fiber taper. The gain spectrum for SBS is very narrow (<100 MHz) with a roughly 10 GHz frequency downshift in silica. The microresonators tested here have free spectral ranges on the order of terahertz, with an eccentricity splitting of the azimuthal modes on the gigahertz scale [77]. In general this splitting is dependent upon fabrication-induced irregularities, thus overlap with the SBS spectrum is unlikely. Consequently, SBS was only observed when a WGM overlapped the Brillouin gain spectrum, in agreement with experiments on liquid droplets [10]. However, the backward spectral monitor did show the expected strong Raman oscillation. Cascaded Raman peaks, if present, were not observed in these measurements due to the wavelength range of the optical spectrum analyzer. However, they have also been observed [78]. Additionally, I might mention that four-wave-mixing associated with the Kerr effect, as described theoretically in section 4.2, was also observed. However, such processes in micro-cavities are governed by strict conditions imposed by the combined effect of the phase-matching requirement with the WGM spectral structure. For the spherical geometry, experiments found that the occurrence of parametric oscillation is very difficult, however, this is not the case for toroidal resonators, as will be discussed in more detail shortly

(section 4.3.3).

To investigate the dependence on quality factor, the threshold was measured while varying the coupling between the taper and microsphere by changing the air gap (figure 4.8). The data follow a near parabolic shape with a measured minimum value of 62 microwatts. This value is the lowest directly measured (not inferred) threshold for SRS of any nonlinear substance to date (further experiments in the Vahala group have realized a slightly lower SRS threshold, however, operating at a lower wavelength where the SRS gain is higher). A theoretical fit, based on exponential dependence of the coupling Q, shows excellent agreement. Good agreement is obtained with a calculated minimum threshold value of 50 microwatts under the assumption that the Raman mode Q is equal to the pump mode Q. The minimum threshold does not lie at the critical coupling point, where circulating pump power (Raman gain) is largest. It occurs for the system in a slightly undercoupled state, corresponding to an observed pump transmission of 12%. This is in excellent agreement with the theoretically predicted value of 11% under the assumption of equal pump and Raman mode quality factors.

Examining the threshold equation (4.3), the threshold is expected to scale approximately as radius squared (effective mode volume is nearly quadratic in radius). To investigate this, the minimum threshold for various sphere diameters ranging from 28 to 110 microns was measured (figure 4.8 inset). The threshold indeed follows a quadratic dependence on size. The dependence on quality factor is normalized out (assuming pump and Raman Q's are identical) due to its strong effect on threshold. In previous work on microdroplets, it was found that for droplets with diameters of less than 30 microns there is an additional threshold reduction due to cavity QED effects [79]. The data in this section do not indicate any cavity QED gain enhancement effects, which is in agreement with recent theoretical work [80].

The efficiency of the Raman oscillator was investigated by decreasing the pump power until a single emission wavelength was observed on the optical spectrum analyzer (figure 4.9). The measured threshold is 86 microwatts for this 40-micron-diameter sphere. This value is nearly 1000× lower than the corresponding values measured in previous work using microdroplets (45 mW for a 30-micron-diameter CS_2 droplet; ref. [79]), despite the fact that silica has a 1000 times lower Raman gain coefficient. This improvement of nearly 10^6 results from efficient single WGM excitation, whereas free space beams (used previously) lack high

spatial mode selectivity. Upon closer examination, the Raman emission in fact consisted of a number of separate simultaneously oscillating peaks (to the temporal resolution of the optical spectrum analyzer), corresponding to different azimuthal modes. The number of oscillating modes was typically 3 to 5, owing to the spatial selectivity of the fiber-taper. The measured unidirectional absolute conversion efficiency was 16%, with a differential quantum efficiency (CW and CCW oscillation) of 36%. In other microspheres tested Raman output powers as large as 200 microwatts have been obtained.

There are several ways to improve the performance of this system. As quality factors above 10^9 have been achieved previously in fused-silica microspheres [3], it should be possible to obtain sub-microwatt Raman thresholds. Furthermore, while these preliminary experiments investigated the low power behavior of these structures, improved efficiency will be obtained by optimizing the coupling geometry.

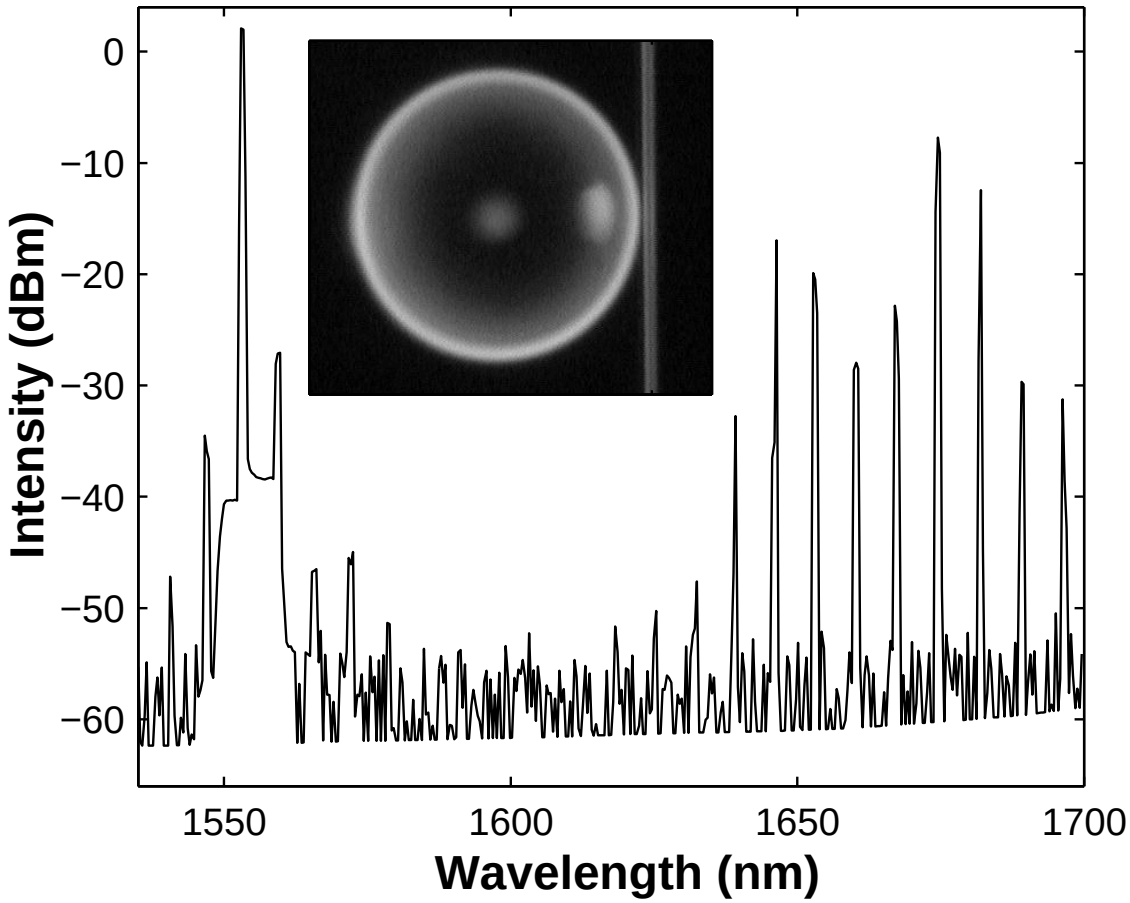

Figure 4.7: Spectrum of a 70-micron-diameter Raman microsphere laser with pump powers of 2 mW. The pump is at 1555 nm. The peaks located around 1670 nm are Raman oscillation, separated by the FSR of the microsphere. The secondary lines around 1555 nm are due to FWM between the pump and two Raman waves. Inset is a microsphere coupled to a fiber taper.

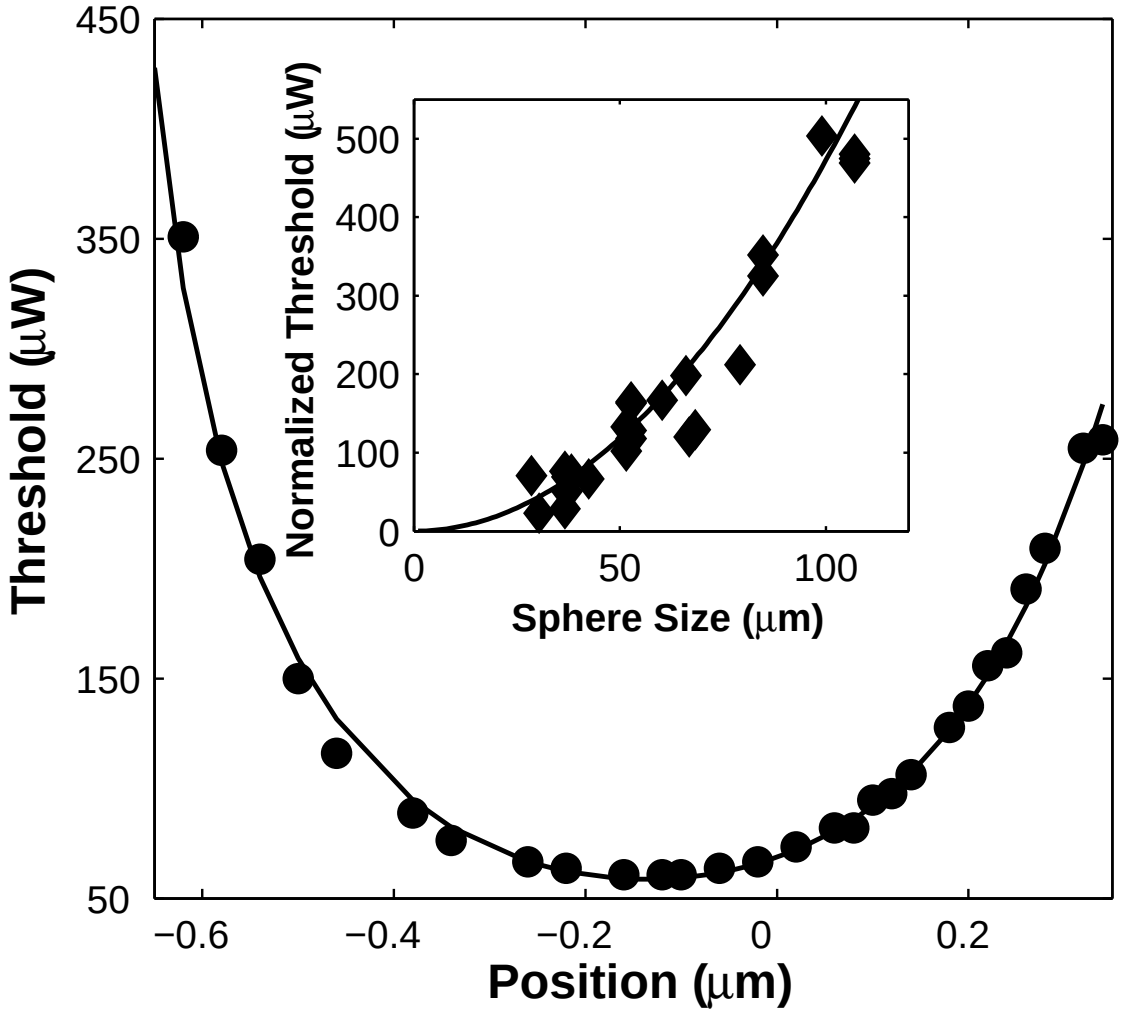

Figure 4.8: Coupling gap and size dependence of the Raman threshold. Main figure, Raman oscillation threshold versus taper-sphere gap for a 40-micron-diameter sphere ($Q_0 = 10^8$). Position is measured from the critical coupling point, where negative values correspond to the undercoupled regime. The minimum threshold occurs with the microsphere about 0.15 microns undercoupled, and corresponds to a transmission of 12%. Solid line, a theoretical fit to the threshold equation. Inset, normalized minimum threshold versus sphere size, following a quadratic dependence.

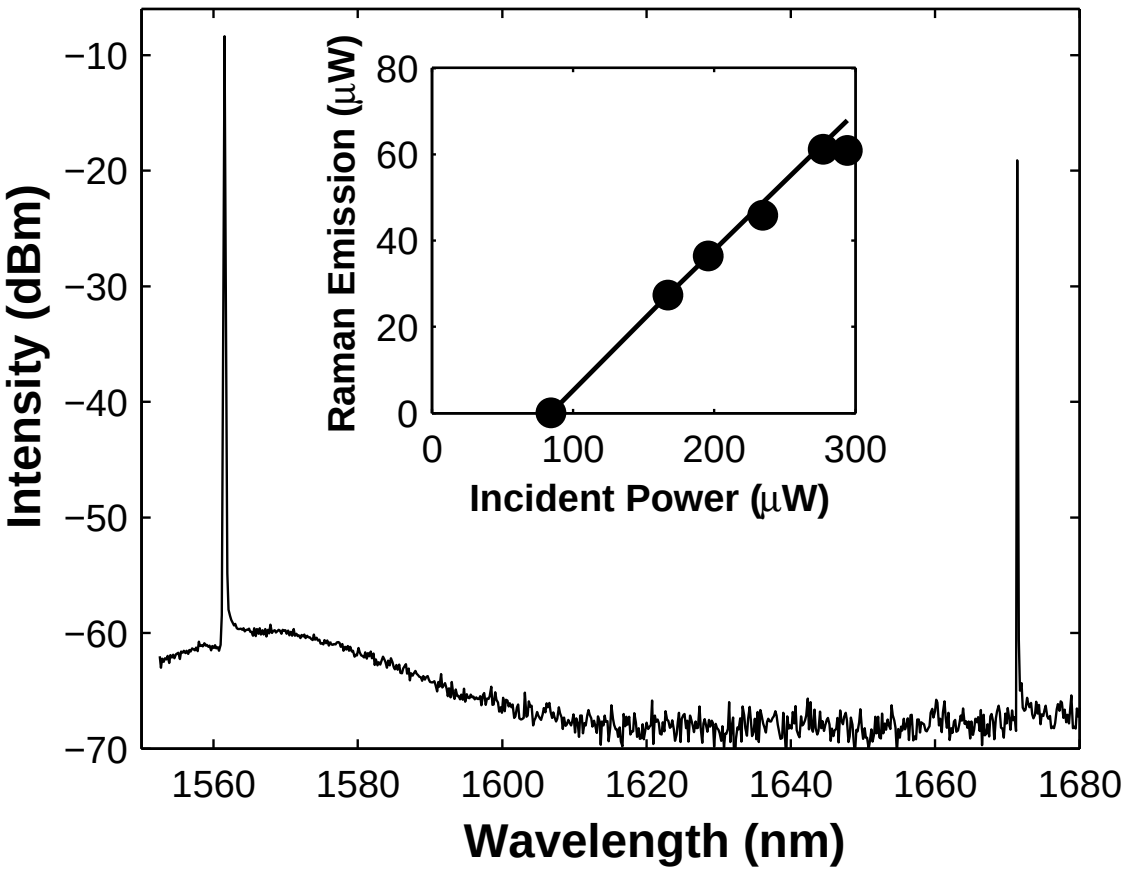

Figure 4.9: Single longitudinal mode Raman lasing. Raman spectrum for a 40-micron-diameter microsphere, exhibiting a uni-directional conversion efficiency of 16% (pump is at 1555 nm). Inset shows Raman power output (sum of forward and backward emission) versus incident pump power. Differential quantum efficiency is 36%.

4.3.2 Stimulated Raman scattering in silica toroidal microresonators

The previous section has shown that efficient generation of nonlinear waves in a silica microsphere through the Raman effect is possible, efficient, and matches very well with a simple theoretical model. However, the presence of a multiline emission spectrum due to the closely spaced azimuthal structure in a spherical cavity [77] is a significant drawback to practical utilization of these structures. As the presence of nearly degenerate azimuthal modes is a necessity in high-quality spherical cavities, methods to resolve this problem are not readily apparent. Furthermore, the lack of easy integration and control do not bode well for future applications. I have demonstrated in section 2.3 that chip-based toroidal microcavities can retain the high-Q of spherical WGM resonators, while having advantages in terms of reproducibility, fabrication parallelism, integration, and a nondegenerate azimuthal mode structure. Thus, these structures should allow low-threshold and single-mode Raman oscillation.

Nonlinear wave generation has been investigated in this microcavity, with figure 4.10 showing a typical Raman emission spectrum for a toroidal microcavity pumped above threshold. Both first order and second order SRS are shown, with the pump near 1550 nm. Observation of the Raman spectrum reveals that only a single azimuthal mode is lasing, in contrast to microspheres. This occurred for a wide range of pump power and coupling conditions, suggesting that this is an intrinsic property of SRS in this cavity. This result is not surprising, as the toroid geometry does not possess degenerate azimuthal modes, due to the added vertical confinement. As described in detail in section 2.3.2, even for weakly toroidal geometries this azimuthal splitting can be significant, such that these modes have a substantially lower Raman gain. This fact alone, coupled with the relative ease of fabrication and chip-based nature suggest these cavities are advantageous to silica microspheres.

Figure 4.11 shows a typical threshold graph of a toroidal microcavity. It shows a threshold of approximately 120 microwatts with a differential efficiency of 22%. This value is consistent with that determined by theory for the experimental values used. Additionally, further investigation has obtained thresholds on the order of 70 microwatts, very close to the current record in microspheres (62 microwatts at a wavelength of 1550 nm). This demonstrates that toroidal cavities do in fact retain the low threshold behavior of microspheres. However, a toroidal cavity design has additional advantages as well.

The threshold for SRS scales linearly with mode volume, as discussed previously. As discussed in detail in section 2.3.2.3, toroidal microcavities have a smaller mode volume than spherical cavities, thus they should also have a lower threshold for SRS. Investigations have shown that this does in fact hold (when a careful accounting of all the parameters determining the threshold is performed) [26].

All these previous results (in both microspheres and toroidal microcavities) have focused on the low or moderate pump power regime, in order to investigate the threshold behavior of such resonators. However, it is also instructive to investigate the high pump power operation of such structures. In contrast to laser sources based on an excited medium (such as erbium), the ultrafast nonlinear response suggests that high output power may also be possible. For example, erbium-doped microcavity lasers have not obtained output powers exceeding approximately 100 microwatts, as a result of the finite density of dopants (limited by effects such as up-conversion and ion-clustering) and the relatively slow lifetime of the radiative and nonradiative transitions (< 1 ns). Nonlinear sources based on silica should not have these drawbacks, as the phonon relaxation rate is on the order of 1 ps, and thus in principle the output power is limited only by the pump power (until very large pump powers, on the order of watts, are used). I have investigated the possibility of obtaining large output powers in a toriodal microcavity, as shown in figure 4.12. The pump wave is near a wavelength of 1550 nm, with an input power of 26 mW, obtained by using an erbium-doped fiber amplifier. The data clearly demonstrate that strong nonlinear oscillations are present. The spectrum consists of a multitude of nonlinearly generated waves ranging from 1450 nm to 1750 nm, a span of 300 nm with a separation of approximately 10 nm, corresponding to the free-spectral range of the resonator. Again, each emission line is single mode as expected in toroidal microcavities. These lines are generated by a combination of SRS (gain peak around 1650 nm) and four-wave mixing between the high power pump and emission beams to generate the resulting blue and red-shifted emission in a complex set of interactions. The inset shows the output power versus input pump power for the emission line at 1650 nm. This shows that an output power of 2.6 mW is achieved for an input power of 26 mW, an overall conversion efficiency of 10%. Furthermore, observation of the output emission for the blue-shifted emission at 1540 nm shows an output power of 5.6 mW. If one considers the total conversion efficiency between

the pump wave and all generated nonlinear waves a value of 40% is obtained. This ability to obtain record high output powers from a microcavity demonstrate that these structures can obtain output powers large enough for practical applications.

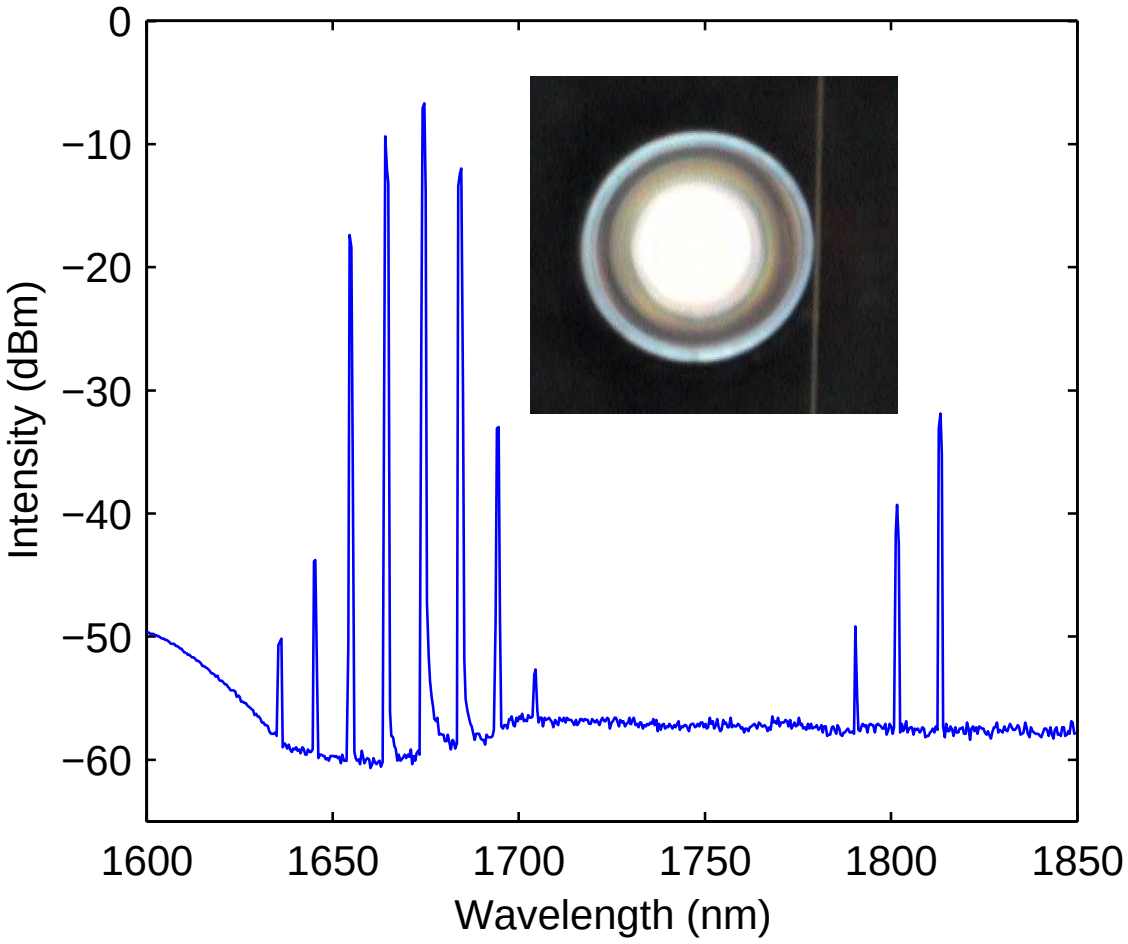

Figure 4.10: Raman spectrum in a toroidal microcavity pumped above threshold. The pump is at 1550 nm (not shown), with SRS emission centered around 1670 nm. The emission at 1800 nm is due to cascaded SRS. Inset shows an optical micrograph of the toroid coupled to a fiber taper.

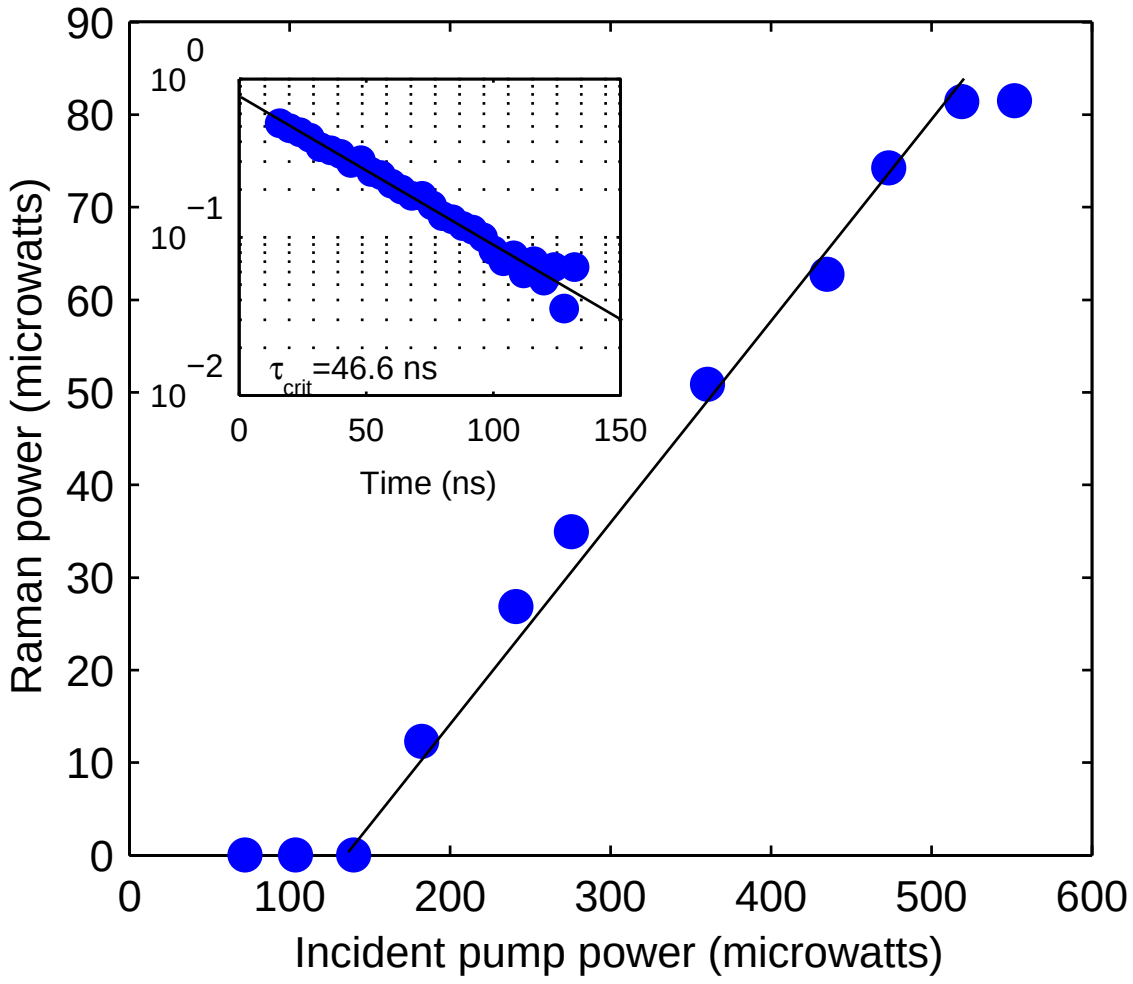

Figure 4.11: Output power versus pump power for a toroidal microcavity. This device had a threshold of 150 microwatts with a differential conversion efficiency of 22%. The inset shows the photon lifetime in the cavity below threshold, indicating a lifetime of 46.6 ns which corresponds to an intrinsic quality factor of 1.13×10^{8}.

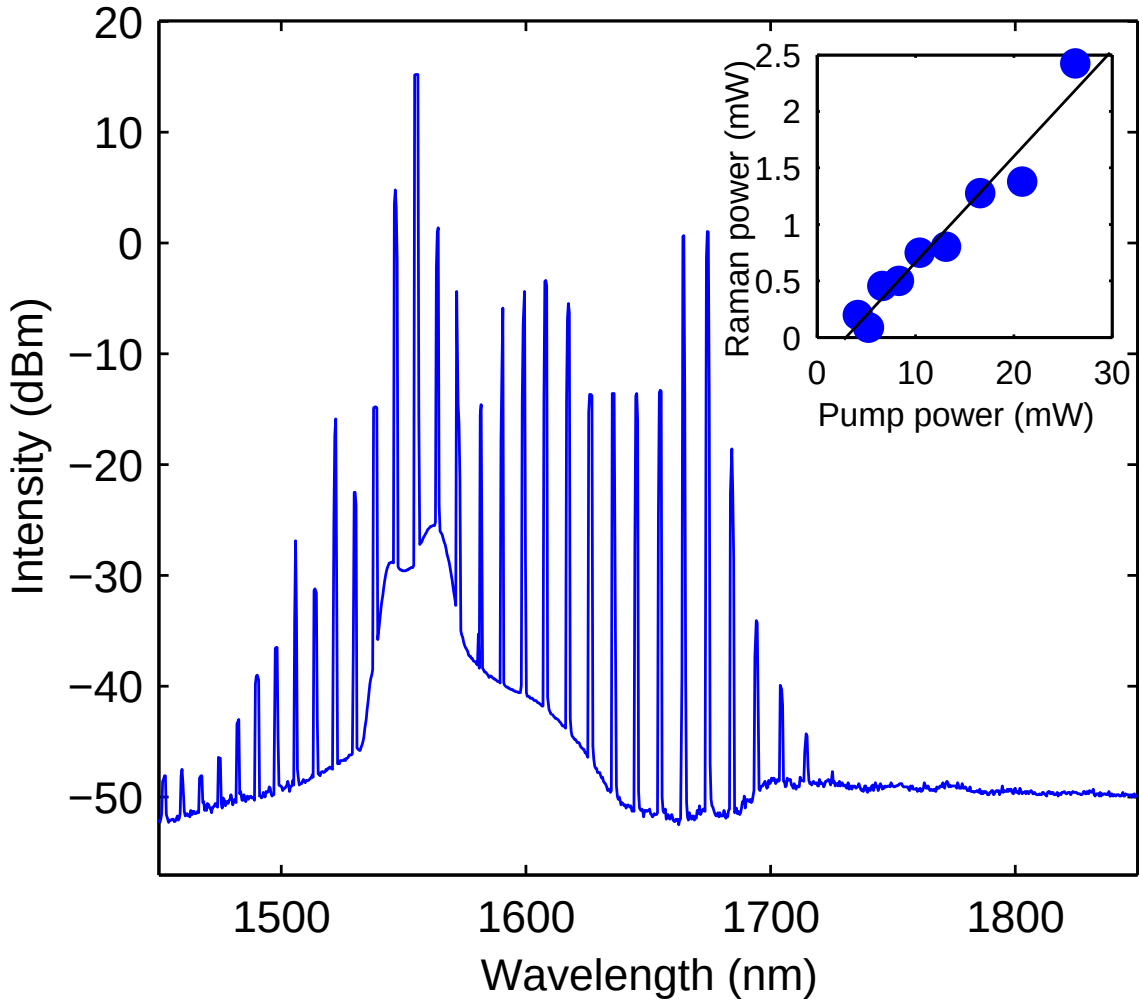

Figure 4.12: Emission spectrum for a toroidal microcavity pumped far above threshold (26 mW). A multitude of emission lines are present, generated from the pump wave at 1550 nm, corresponding to SRS and Raman-assisted FWM. The nonlinearly-generated waves span nearly 300 nm, separated by the FSR of the cavity (∼10 nm). The inset shows the output power versus pump power for emission at 1650 nm, showing a maximum output power of 2.6 mW. Also, the output power is 5.6 mW for emission at 1540 nm. Overall conversion efficiency is 40%.

4.3.3 Parametric oscillation in toroidal microcavities

The experimental realization of optical parametric oscillation at low threshold in a microcavity is difficult, as the requirement of a very low intrinsic cavity frequency detuning ($\sim$ 10 MHz) cannot usually be met, especially when considering cavities with large free-spectral-ranges ($>$ 1 THz) [2]. This arises from the fact that the microcavity mode spacing is not uniform, with the separation between successive longitudinal cavity modes increasing as the resonance wavelength increases. This fact, combined with competition with SRS, resulted in the lack of repeatable parametric oscillation in the silica microsphere cavities first studied. However, the use of toroidal microcavities can overcome these obstacles.

First, the dependence of the parametric bandwidth Ω on the nonlinear parameter γ means that an improved detuning tolerance occurs when γ is increased. As γ is inversely proportional to mode area (or equivalently mode volume), the smaller modal volumes of toroidal cavities result in larger parametric bandwidths. Secondarily, toroidal cavities can reduce the intrinsic cavity detuning $\Delta\omega$, making it much easier in practice to realize parametric oscillation. This can be seen by noting that for the toroidal geometry there is increased modal overlap with the external dielectric medium, which flattens the total modal cavity dispersion. Another way to look at this is to observe that relative to a spherical cavity, the longer wavelength toroidal longitudinal modes are more perturbed by the dielectric interface and have their resonant wavelengths lowered by an amount larger than lower wavelength modes, thus slowing the natural increase of FSR as a function of wavelength. All these effects suggest that by proper geometrical control it may be possible to obtain repeatable low-threshold parametric oscillation in a toroidal microcavity. In fact, this is the case, as small inner diameter toroidal microcavities (below $\sim$4 microns) exhibit pure parametric oscillation, with near unity signal-to-idler ratio. This result is described in more detail in reference [82].

[2] Recently, a microcavity parametric oscillator was demonstrated in a lithium niobate cavity [81]. However, the FSR was about 10 GHz, which makes it much easier to realize a low cavity detuning

Chapter 5

Cavity quantum electrodynamics in toroidal microcavities

5.1 Introduction

The use of an optical microcavity can greatly enhance the interaction between matter and the electromagnetic field, such that even a single atom or photon can significantly change the dynamical evolution of the atom-cavity system [30, 83]. This ability to substantially modify the electromagnetic cavity properties at the single atom or photon level, known as strong-coupling, is critically dependent on the characteristics of the optical cavity. Recent experimental realizations of strong coupling, ranging from observation of the atomic trajectory of a single-atom in real-time [84, 85], to a "one and the same" atom laser [86], have employed high-finesse Fabry-Perot (FP) optical microcavities. These cavities, while possessing ultra-high quality factors and finesses, are difficult to manufacture and control, requiring expensive and sophisticated dielectric mirror coatings. Due in part to these reasons, there has been increased interest in other microcavity systems which not only can address some or all of the limitations of Fabry-Perot cavities, but which in principle can have improved optical properties.

Whispering-gallery-mode cavities have been investigated for cQED experiments for many years, resulting from the possibility of attaining extremely high quality factors [87, 88]. In particular, experimental studies have demonstrated a record quality factor for any optical resonator approaching 10 billion in a silica microsphere [3], with values exceeding 100 million readily achievable over a broad range of cavity diameters and operation wavelengths. The combination of the very low loss of these cavities, plus their relatively easier fabrication than competing cavity designs, makes them strong candidates for future experiments in cQED

[89]. Furthermore, the ability to obtain record coupling efficiencies both to and from optical fiber [21] is promising from a technological standpoint, as optical fiber is a highly desirable transport medium for quantum optic fields [34]. While to date there has been a number of both experimental and theoretical studies on the capabilities of silica microspheres, a fundamental problem arises in that the atom-cavity coupling strength and the quality factor of the cavity are not independent from each other. As discussed in more detail in reference [90], this arises from the single geometrical degree of freedom in a spherical cavity, which thus constrains the atom-cavity coupling strength for a given quality factor. Obviously, it is desirable to be able to control both the atom-cavity coupling strength and cavity loss rate independently, allowing not only flexibility in experimental investigations but also the ability to simultaneously maximize both the coupling strength and cavity quality factor.

Recently, a new type of whispering-gallery-mode optical microcavity was demonstrated, which not only retains the high quality factors of spherical cavities, but also has significant advantages in fabrication reproducibility, control, and mode structure. These cavities consist of a toroidally-shaped silica dielectric produced on a silicon microelectronic chip [25]. The toroidal cavity shape allows an extra level of geometric control over spherical cavities and thus begs the question on how these structures compare with silica microsphere and other microcavity designs for strong-coupling cavity QED. In this thesis I numerically investigate the suitability of toroidal microcavities for strong-coupling cavity QED experiments, for clarity focusing on the interaction with atomic cesium. I show that these cavities can achieve ultra-high-quality factors far exceeding 100 million while simultaneously obtaining very large coupling rates between the cavity and a cesium atom. It is found that not only can these cavities surpass the estimated fundamental limits of FP technology, but also either exceed or compare favorably to other cavity designs such as photonic bandgap cavities, in particular with respect to critical atom number. Lastly, I present preliminary experimental measurements of toroidal cavities for strong-coupling cQED with atomic cesium, which shows that currently attainable values are already quite promising.

5.2 Strong coupling in an atom-cavity system

The coupling rate g between an atomic system and an electromagnetic field is simply related to the one-photon Rabi frequency $\Omega = 2g$, and can be expressed in terms of the atomic and cavity parameters by

$$g(\mathbf{r}) = \gamma_\perp |\vec{E}(\mathbf{r})| \sqrt{V_a/V_m} \tag{5.1}$$

$$V_a = 3c\lambda^2/(4\pi\gamma_\perp) \tag{5.2}$$

where $\gamma_\perp$ is the transverse atomic dipole transition rate, $|\vec{E}(\mathbf{r})|$ denotes the electric field strength at the atom's location $\mathbf{r}$, V_a is a characteristic atomic interaction volume (which depends on the atomic dipole transition rate, the transition wavelength λ, and the speed of light c), and V_m is the cavity electromagnetic mode volume. Assuming the atom interacts with the electromagnetic field for a time T, strong atom-field coupling occurs if the rate of coupling exceeds all dissipative mechanisms, i.e., $g \gg (\kappa, \gamma_\perp, T^{-1})$. In this expression κ denotes the cavity photon loss rate, given in terms of the cavity quality factor Q by $\kappa = \pi c/(\lambda Q)$. The strong-coupling conditions can also be reformulated into a set of normalized parameters,

$$n_0 = \gamma_\perp^2/(2g^2) \tag{5.3}$$

$$N_0 = 2\gamma_\perp \kappa/(g^2) \tag{5.4}$$

$$(N_0, n_0) \ll 1 \tag{5.5}$$

where n_0 is the critical photon number, which is the number of photons required to saturate an intra-cavity atom, and N_0 is the critical atom number, which gives the number of atoms required to have an appreciable effect on the electromagnetic cavity transmission. Examining these parameters, is it apparent that only the critical atom number is dependent on the cavity loss rate (or equivalently Q factor). It is the possibility of realizing extremely low critical atom numbers with ultra-high-Q microcavities that has fostered the investigation of silica microspheres for strong-coupling cQED experiments [87]. However, the spherical geometry greatly constrains the magnitude of atom-cavity coupling available while maintaining ultra-high quality factors [90]. This is a result of the fact that to achieve large atom-cavity coupling

rates (comparable to or exceeding those of FP cavities) the cavity diameter must be made small (8 micron diameter sphere gives $g/(2\pi) \approx 740$ MHz) in order to both lower the modal volume and increase the electric field magnitude at the atomic position. Here though, the cavity dimensions are such that the radiation loss of the cavity is the limiting factor in determining the overall quality factor ($Q \approx 4 \times 10^4$). While the comparatively large mode volumes of silica whispering-gallery-mode cavities preclude them from competing with ultra-small mode volume cavities (such as photonic bandgap cavities) on the basis of coupling strength alone, there is the possibility to access the best features of both worlds (i.e., small mode volumes plus ultra-high-quality factors) by using toroidal microcavities.

5.3 Microtoroid numerical modeling

In order to investigate the properties of microtoroids for cQED, this chapter will focus on the D_2 transition of cesium which occurs at a wavelength of 852.359 nm. Fundamentally, the coupling between an atom and a cavity field can be specified by three parameters: the cavity field strength at the atom's location, the cavity mode volume, and the cavity quality factor. Since the optical modes are confined in the interior dielectric in whispering-gallery-type resonators, the atom can only interact with the cavity evanescent field. In the following discussion, the atom is assumed to be located near the resonator surface at the location where the electric field strength is largest. For TM polarized modes this occurs at the outer cavity boundary in the equitorial plane, while for TE polarized modes the location of the maximum external field strength is more complicated. As discussed below, as the toroidal geometry is compressed with respect to a sphere, the maximum field strength for a TE polarized mode changes from the equitorial outer cavity boundary to approaching the azimuthal axis. While experimentally the ability to precisely localize the atom at the cavity field evanescent maximum is currently not possible, this assumption allows a simple way to characterize the relative merit of this cavity geometry with respect to other cavity designs. Only the fundamental radial and azimuthal modes for both polarizations (TE and TM) are considered, as they possess the smallest modal volumes and thus the highest coupling strengths.

The numerical modeling method described in section 2.3.2 was used to predict the optical cavity properties of interest for strong-coupling to cesium. The calculated geometry corre-

sponded to principle diameters in the range of 16-20 microns for varying minor diameters, with a representative electric field plot of the TM polarized fundamental mode at 850 nm for a principle cavity diameter of 16 microns given in figure 5.1. Due to the fact that for smaller cavity geometries the resonance wavelengths do not necessarily coincide with the cesium transition of interest, the data were taken for the closest resonance wavelengths both blue and red shifted with respect to the desired resonance, then extrapolated to the target wavelength (the mode volumes were linearly extrapolated and the radiation quality factors exponentially extrapolated as a function of wavelength).

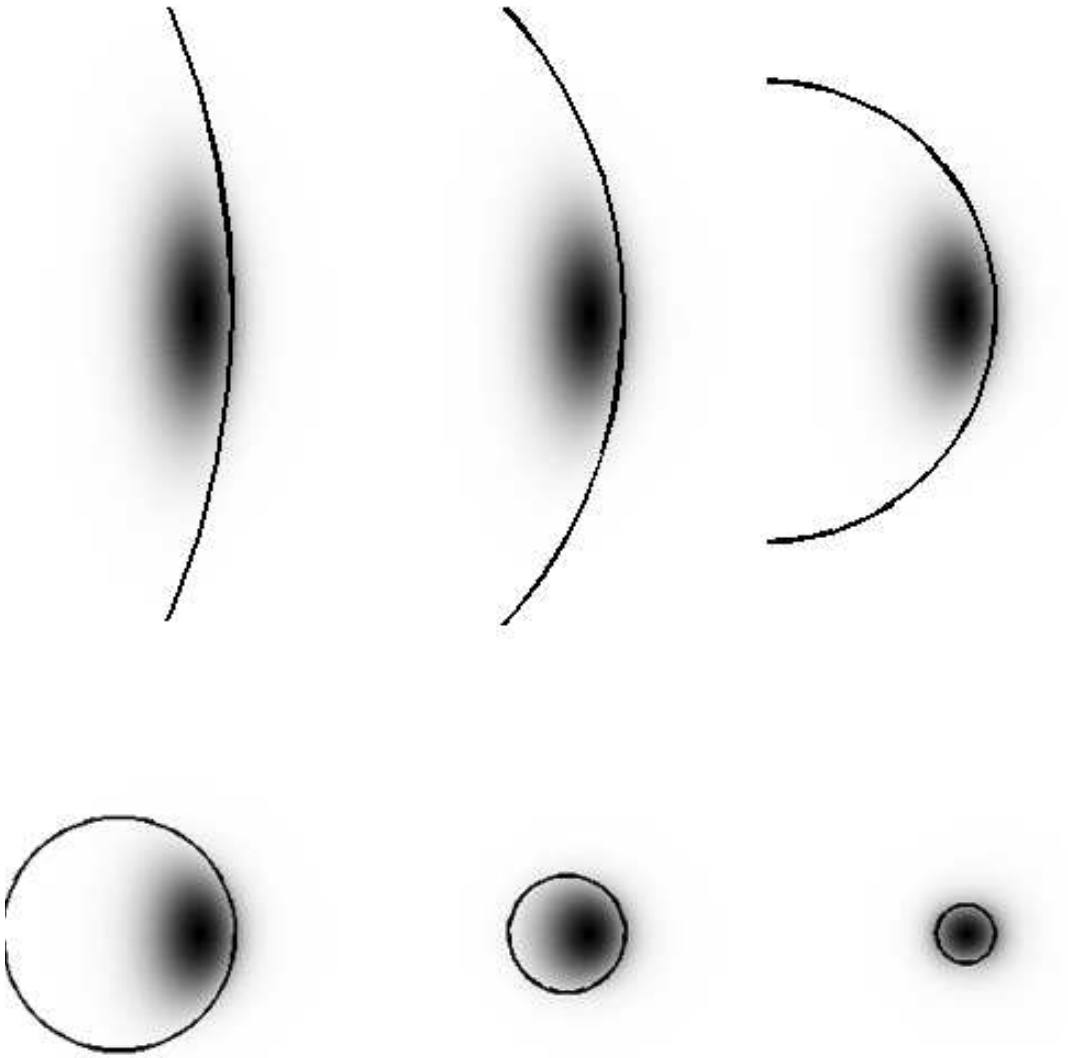

Figure 5.1: Electric field profiles for a toroidal cavity with a principle diameter of 20 microns and inner diameters of 20, 12, 6, 3, 1.5, and 0.75 microns. The calculations correspond to a TM polarized mode near 850 nm. The optical mode behaves as a whispering-gallery-type mode until an inner diameter below approximately 1.5 microns, at which point the mode approaches that of a step-index optical fiber.

5.3.1 Mode volume

The optical mode volume is given by equation 2.5, which is reprinted here for clarity,

$$V_m = \frac{\int_{V_Q} \epsilon(\vec{r})|\vec{E}|^2 d^3\vec{r}}{|\vec{E}_{\max}|^2}$$

where V_Q represents a quantization volume of the electromagnetic field, and $|\vec{E}|$ is the electric field strength [43]. In these calculations, the quantization volume cross-section is chosen to consist of a square region of approximately 10 micron width and height centered about the radial cavity boundary. This choice allows the mode volume to be determined to a good accuracy while minimizing computational requirements. As a further confirmation of the validity of this approach, note that the radiation loss is weak for the range of geometries modeled in this work, resulting in only a marginal difference on the numerically calculated mode volume.

Figure 5.2 shows the calculated modal volumes for the fundamental mode of a toroidal cavity with principle diameters ranging from 16 to 20 microns as a function of the inner diameter. For clarity, only data for inner diameters below 4 microns are shown. Both TM (squares) and TE (circles) polarizations are shown. The data show that there is a reduction of modal volume for both polarizations as the toroid inner diameter is decreased. This is expected when considering the additional confinement provided by the toroid geometry, as illustrated in the electric field plots of figure 5.1. There is initially a slow reduction of modal volume as inner diameter is decreased, which agrees very well with a simple model which treats the optical mode as a two dimensional harmonic oscillator (in the radial and azimuthal directions), with the change of toroid inner diameter changing solely the azimuthal contribution. This approach results in a reduction of modal volume which scales as $(d/D)^{1/4}$ with respect to that of a spherical cavity. This formula holds for inner diameters greater than approximately 2 microns. At this point, the geometrical confinement becomes strong enough that the optical mode is also simultaneously compressed in the radial direction. This results in a faster reduction of modal volume, with the optical modes approaching those of a step-index optical fiber (this occurs for an inner diameter below approximately 1 micron) [62]. The mode volume reduces until the point where the optical mode becomes delocalized due to the weak geometrical confinement,

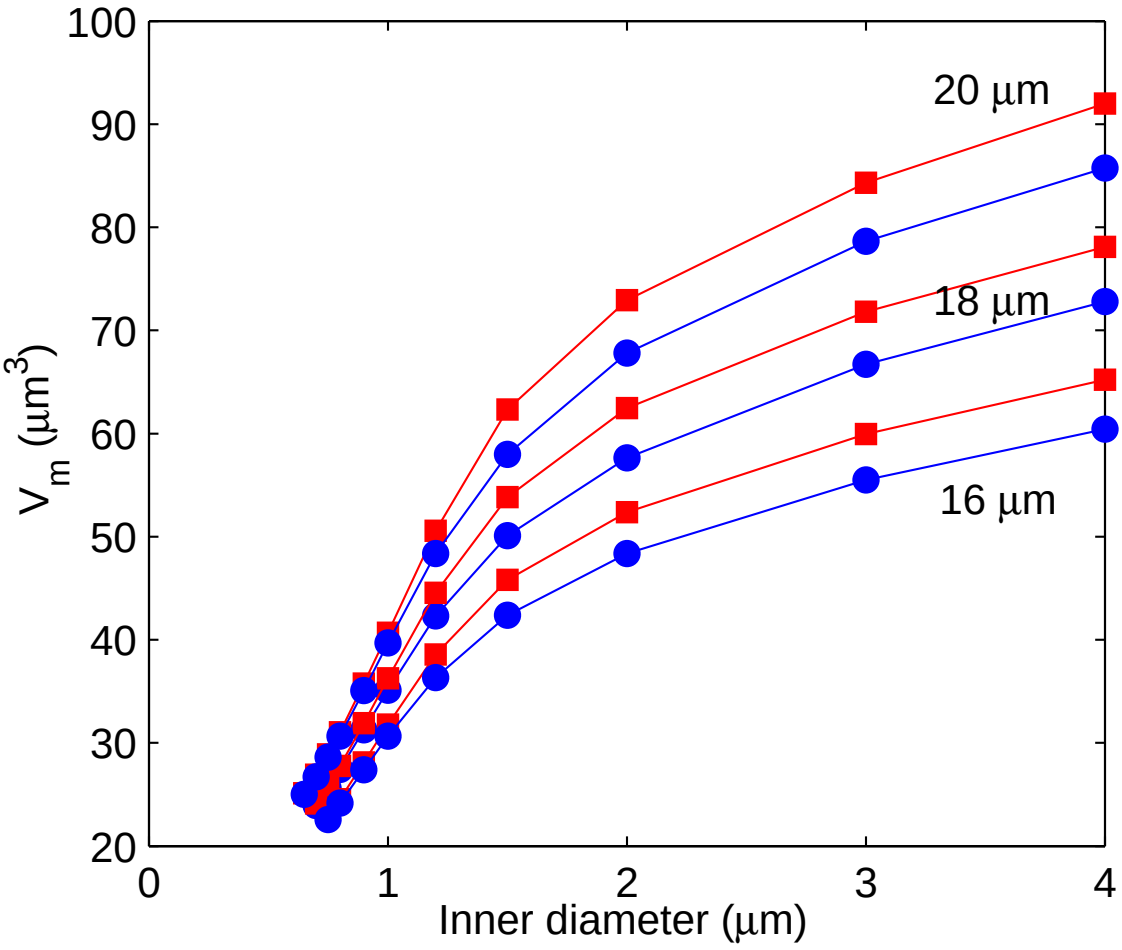

Figure 5.2: Calculated mode volumes for a silica toroidal microresonator versus inner diameter for principle diameters of 20, 18, and 16 microns. The data show both TM (red squares) and TE (blue circles) polarization. The data show that as the inner diameter is reduced there is a slow reduction of modal volume due to confinement in the azimuthal direction, and then a fast reduction for large confinement when the optical mode is strongly compressed in both the radial and azimuthal directions.

causing a finite minimum value. Determination of the exact point of the minimum modal volume upon reduction of inner diameter (for a fixed principle diameter) can be uncertain, as the choice of quantization volume now plays a critical role (as discussed above). Because of this the data in figure 5.2 show the modal volume only for inner diameters down to 0.65 microns.

Calculation of the modal volume and the maximum electric field amplitude at the exterior cavity equatorial boundary is straightforward, giving a simple way to calculate both the coupling strength and the critical photon number. In order to get the critical atom number, however, the cavity Q factor must be determined.

5.3.2 Quality factor

Figure 5.3 shows numerical calculations of the radiative quality factor (described in section 2.3.2.2) as the inner diameter is decreased for various outer diameters of 16, 18, and 20 microns. We see that there is an initial slow reduction of the quality factor when the optical mode retains whispering-gallery behavior, with a scaling in qualitative agreement with the approximate model given by equation 2.11. When the optical mode transitions into a step index fiber-like mode (for inner diameters below 1 micron) the drop-off of the radiative Q is much more dramatic, with decreases over an order of magnitude for a change of inner diameter of just 50 nm.

The total optical loss of a cavity has contributions from not only radiation loss, but also includes other dissipative mechanisms, such as intrinsic material loss, losses resulting from both surface and bulk scattering, and contaminates on the resonator surface [49]. One of the dominate contaminates which adversely affect the cavity Q is OH and water adsorbed onto the cavity surface. While prior investigation on these loss mechanisms have resulted in approximate expressions for water absorption and surface scattering [3, 37], only very large resonators were studied, as opposed to the much small diameter cavities studied in this work. To obtain an improved estimate of the effect of water on the small diameter cavities in this thesis, a simple model was used which determines the fraction of optical energy absorbed by a monolayer of water located at the cavity surface. This method gives an estimated quality factor for a monolayer of water to above 10^{10} for the case of a spherical resonator. As this

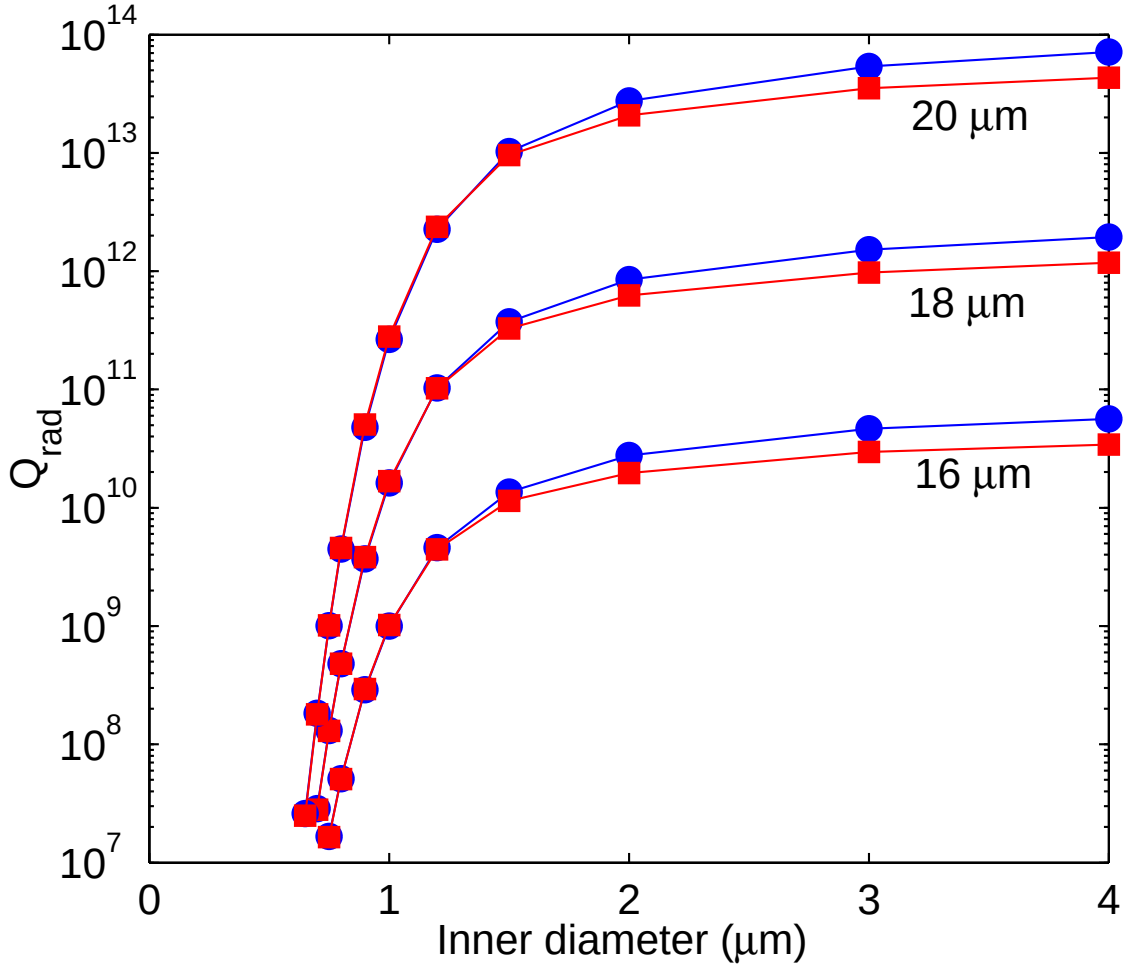

Figure 5.3: Calculated radiation loss for a toroidal microcavity as a function of inner diameter, for principle diameters of 20, 18, and 16 microns. Both TM (red squares) and TE (blue circles) polarizations are shown. The data show that there is a slow reduction of Q as the optical mode is compressed while the mode acts primarily as a whispering-gallery-type mode. However, as the geometrical confinement increases to such a point as the optical mode approaches that of a step-index fiber, there is a much stronger reduction of quality factor.

contribution is weaker than that of the intrinsic silica absorption, and in principle with proper fabrication the presence of water and OH can be prevented, with surface scattering minimized, this chapter will focus on the contributions from intrinsic silica absorption and radiation loss. This puts a fundamental limit on the Q possible in these structures.

Figure 5.4 shows the calculated total quality factor for various outer toroid diameters in the range of 16-20 microns, as a function of the inner diameter. The total quality factor is calculated through the relation $1/Q_{total} = 1/Q_{rad} + 1/Q_{mat}$, where only radiation loss and silica absorption are included. For smaller sizes, there is a monotonic decrease in quality factor as the inner diameter is decreased. This is a result of the whispering-gallery-loss increase due to the additional confinement. The data shows that the decrease in total Q is small unless the inner diameter of the toroid falls below 2 microns.

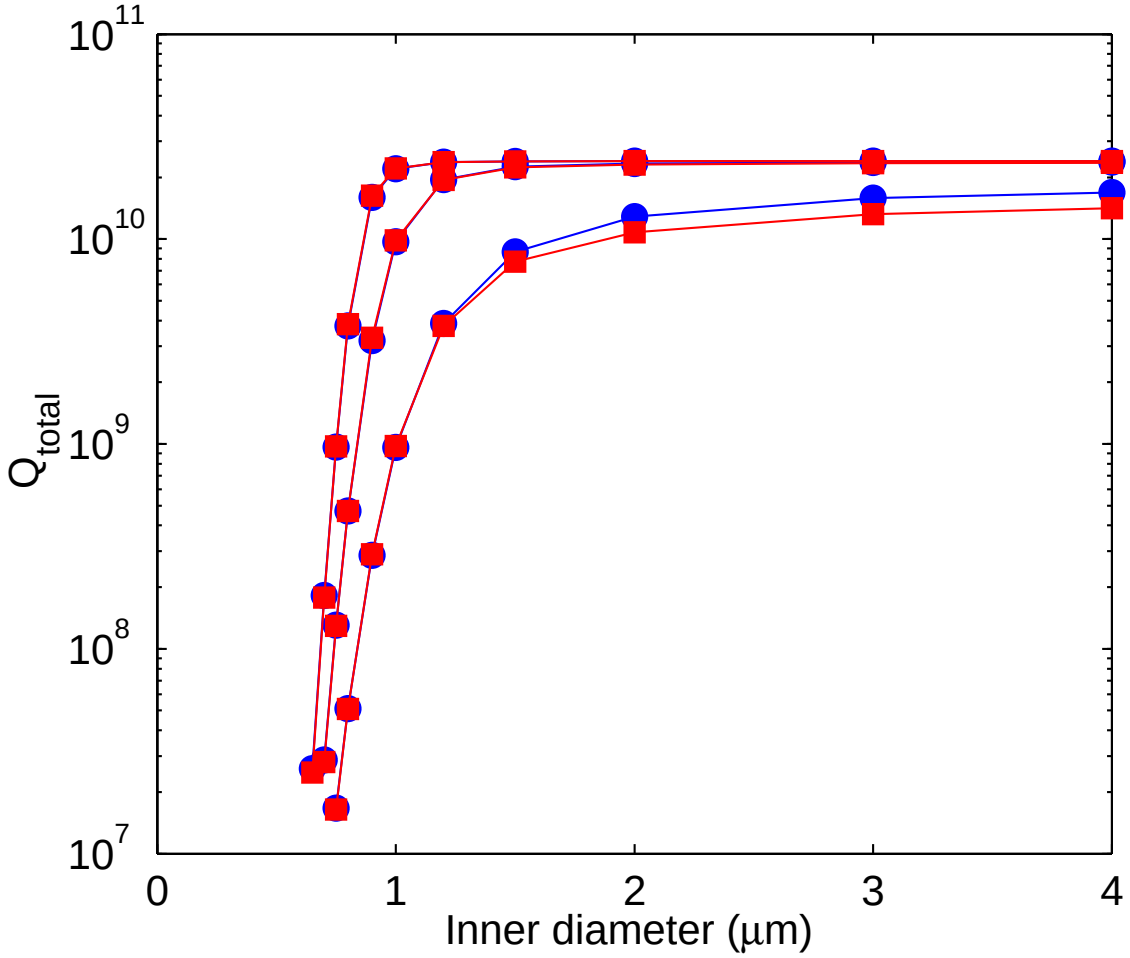

Figure 5.4: Total quality factor for a toroidal microcavity versus inner diameter for outer diameters of 16, 18, 20 microns. The total quality factor is composed of the radiative quality factor from figure 5.3 along with the silica absorption limited $Q_{mat} = 2.4 \times 10^{10}$ at a wavelength of 852 nm. The data indicate that the total quality factor is limited by silica absorption when the principle diameter is larger than 16 microns and the inner diameter is larger than approximately 1 micron. Furthermore, both TE and TM polarizations have similar quality factors over the range of geometries studied.

5.3.3 Cavity QED parameters

The determination of the coupling strength from the modal volume follows from equation 5.1. Figure 5.5 shows the atom-cavity coupling rate $g/(2\pi)$ for various principle diameter toroids as the toroid inner diameter is decreased. It can be seen that there is a monotonic rise in g for higher-aspect ratio toroids, as a direct result of the compression of modal volume. The rate of increase of g as the inner diameter is reduced increases dramatically as the toroid geometry transitions from a whispering-gallery-type mode to a strongly-confined step-index fiber-type mode. This is due not only to the faster rate of reduction of mode volume upon compression, but also due to the increase in electric field strength at the cavity surface. Note that the coupling strengths shown do not correspond to the absolute maximum for these structures, as this work has focused on the simultaneous realization of high quality factors and small modal volume. Therefore, mode volumes were only calculated down to where the radiation quality factor is equal to or exceeds 10 million. Also, as mentioned previously, this regime prevents any uncertainty in the calculated mode volumes (and hence g) through the definition of the modal quantization volume. Under these assumptions, the data indicate that coupling parameters exceeding 700 MHz are possible.

Figure 5.6 shows the corresponding critical photon numbers. The data show that values as low as 6×10^{-6} are possible, with the associated quality factors also exceeding 10 million. As will be discussed in more detail shortly, this value not only is comparable to the fundamental limit of FP technology, but vastly exceeds that possible for microspheres with a comparable quality factor.

One of the primary reasons high-Q whispering-gallery-mode cavities are promising for cQED is on the basis of their very low critical atom number. Figure 5.7 shows the calculated critical atom number versus inner diameter for toroid principle diameters of 16, 18, and 20 microns. The data indicate that for the larger principle diameters of 18 and 20 microns there is a minimum of the critical atom number as the toroidal inner diameter is reduced, occurring near an inner diameter of 1 micron. This minimum results from the clamping of the total quality factor due to silica absorption which occurs for principle diameters larger than approximately 18 microns. Usually there is no added benefit with studying larger principle diameter cavities, as the quality factor is the same but the mode volume is larger. However,

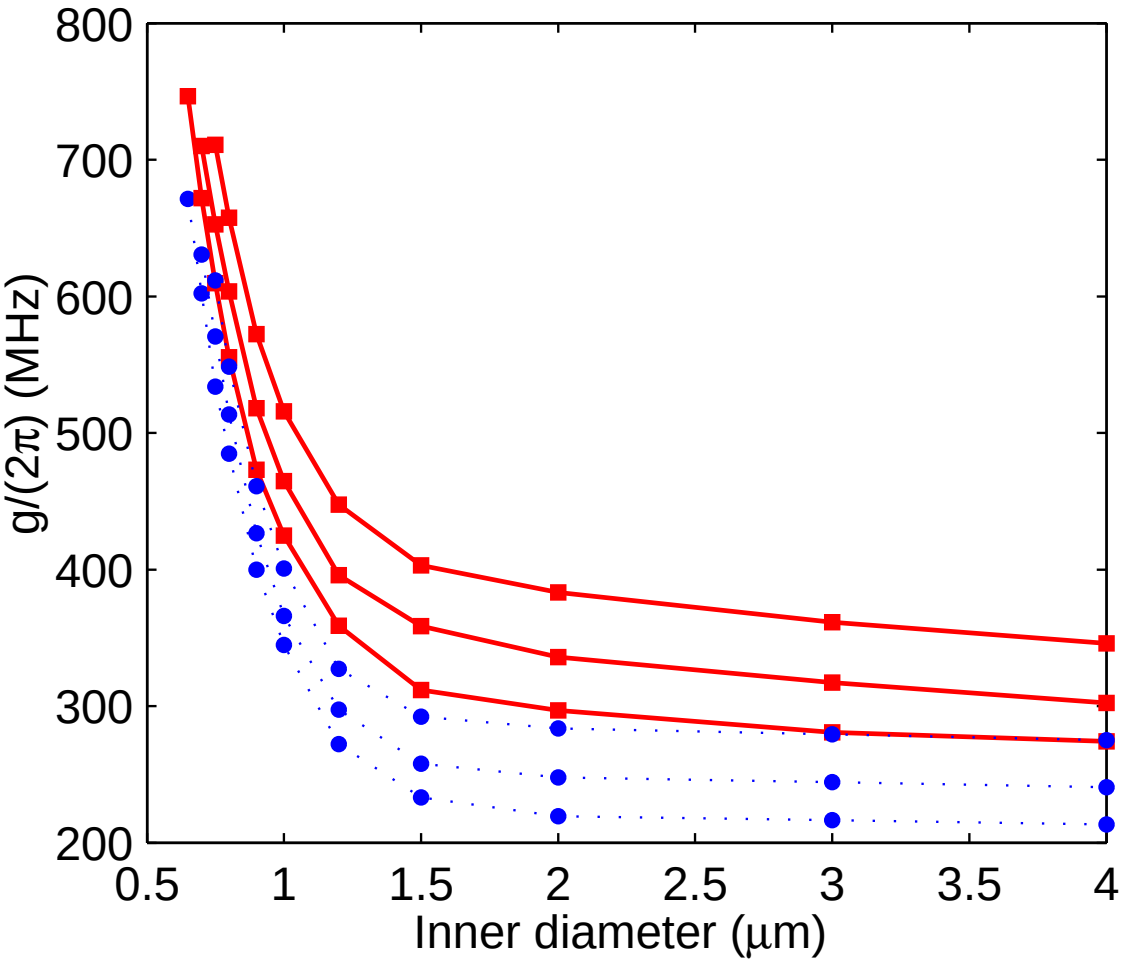

Figure 5.5: Atom-cavity coupling parameter g versus inner diameter for toroidal cavities having an outer diameter of 16, 18, and 20 microns, with g increasing for smaller principle diameters. Both TE (blue circles) and TM (red squares) polarizations are shown. The data indicate that the coupling strength increase dramatically as the inner diameter decreases below 1.5 microns, which is a result of the rapid reduction of mode volume and the increased electric field strength at the cavity surface.

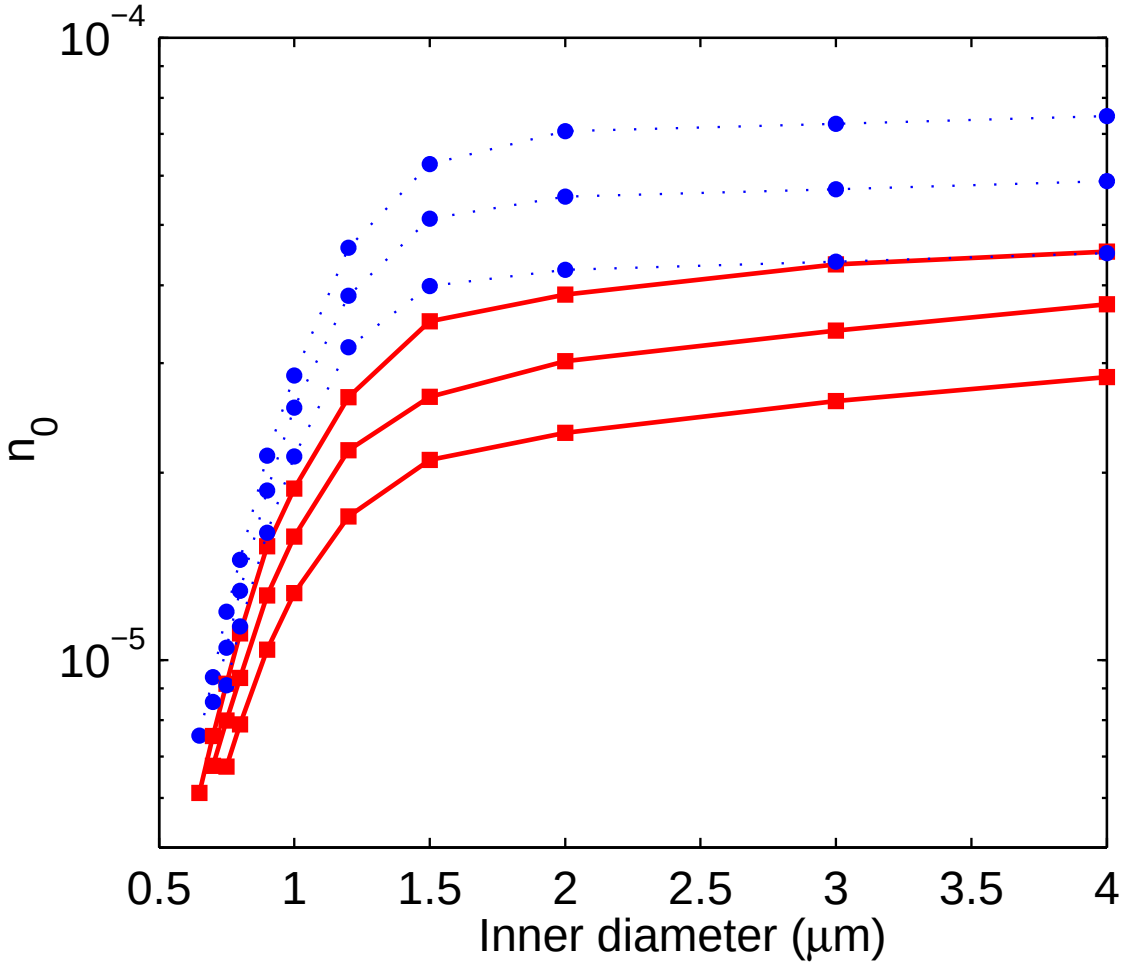

Figure 5.6: Critical photon number versus inner toroid diameter for a cavity with principle diameters of 16, 18, and 20 microns. Both TE (blue circles) and TM (red squares) polarizations are shown. The data show that as both toroid principle diameter and inner diameter are reduced, the critical photon number decreases. This follows directly from the behavior of the atom-cavity coupling parameter g, as indicated in figure 5.5. The data show that critical photon numbers of 6×10^{-6} are possible (with quality factors exceeding 10 million).

in a toroidal geometry there still can be an advantage for slightly larger principle diameters, as the inner diameter can be compressed more strongly while keeping high radiative quality factors, resulting in a lower critical atom number, as illustrated for the 20 micron principle diameter in figure 5.7. The data indicate that a critical atom number of approximately 2×10^{-7} is possible for a toroid principle diameter of 20 microns and an inner diameter of 1 micron.

The presented results indicate that toroidal cavities can obtain high values of atom-cavity coupling while simultaneously retaining an extremely low critical photon number and in particular an exceedingly small critical atom number. While in principle the critical atom number can be greater than 10^3 times smaller than any currently demonstrated cavity, the necessity of realizing material-limited quality factors exceeding 20 billion is experimentally challenging. The current record for any cavity is 9 billion, in a large diameter microsphere cavity, whereas for toroidal cavities we have realized quality factors as high as 500 million at a resonance wavelength of 1550 nm. Furthermore, even if quality factors this large were able to be obtained, it should be pointed out that this may not be desirable, as when the cavity quality factor is much larger than 100 million, the dominant dissipative mechanism in the atom-cavity system is the radiative decay rate of the atomic medium, which is 2.61 MHz for the D_2 transition of cesium. For this reason a more "modest" quality factor, in the range of current experimentally achievable values (e.g., a couple hundred million) is attractive. As these values are currently realizable in our lab for toroidal cavities at a wavelength of 1550 nm, we have investigated the quality factors and fabrication limits for structures designed for strong-coupling to the cesium transition at a wavelength of 852 nm.

As toroidal cavities are fabricated with a combination lithographic-reflow process, the advantages of lithographic control are retained, and in fact are a significant step forward over spherical cavities. As the shape of the initial silica preform dictates the maximum possible principle diameter, and is lithographically formed, precise control of the principle diameter is possible. Reproducible principle diameters ranging from >100 microns to 12 microns have been fabricated. This lower value, while currently dictated by the available laser power in our setup, is sufficient to obtain near optimal cQED parameters, as indicated previously. While the capability to obtain reproducible principle diameters is a significant accomplishment over spherical cavities, the true advantage of the toroidal geometry arises by accurately controlling

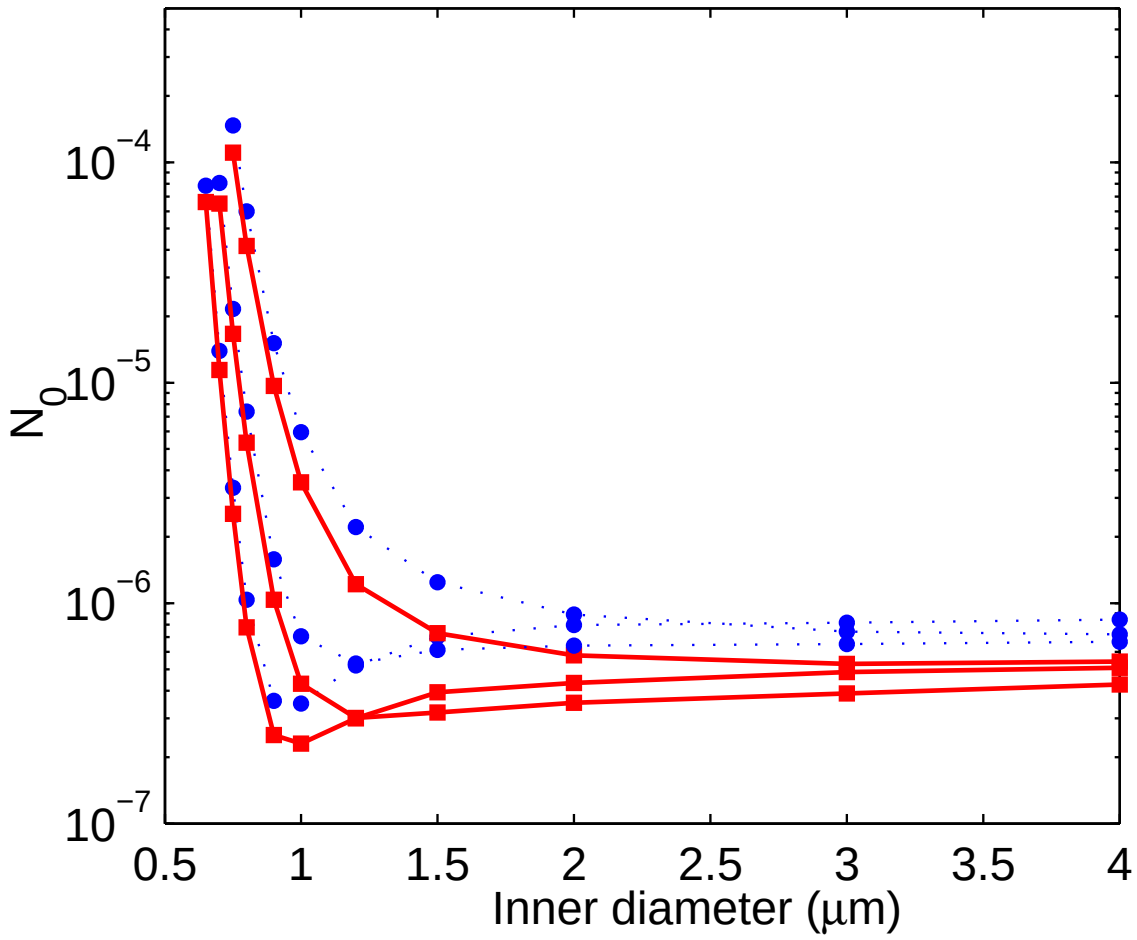

Figure 5.7: Critical atom number versus inner diameter for a toroidal microcavity with principle diameters of 16, 18, and 20 microns. For small inner diameters the critical atom number decreases as the principle diameter increases. Both TE (blue circles) and TM (red squares) polarizations are shown. The data indicate that there is a minimum value of the critical atom number near 2×10^{-7} for a toroidal cavity with a principle diameter of 20 microns and an inner diameter of 1 micron (TM mode).

the inner diameter. The final inner diameter of the fabricated structures is a result of a combination of factors, which are the initial silica preform thickness, the supporting pillar size, and the laser irradiation intensity and duration. As inner diameters down to 3.5 microns have been realized for outer diameters as low as 12 microns, this value of the inner diameter is attainable for the principle diameters investigated in this work.

We measured the quality factor for a toroidal microcavity at a wavelength of 852 nm, obtaining a value of $Q_{total} = 1.2 \times 10^8$ in a cavity with a principle diameter of 50 microns and an inner diameter of 6 microns. While this value is far from the optimal geometry suggested in this manuscript, this structure was chosen in order to simplify the ability to obtain a fundamental resonance which occurs at 852 nm. Even for this relatively large structure, cavity QED parameters of $(g/(2\pi), n_0, N_0) = (86 \text{ MHz}, 4.6 \times 10^{-4}, 1.0 \times 10^{-3})$ are obtained. Comparison of these values to FP cavities indicate that even without additional improvements in fabrication there are significant advantages in both coupling strength and critical atom number. Additionally, provided we can fabricate a toroidal cavity with a quality factor of 100 million at a wavelength of 852 nm with the optimal principle diameter of 13 microns and an inner diameter of 3.5 microns (which has a radiative quality factor limit of 180 million), the TM polarized optical mode would have cQED parameters of $(g/(2\pi), n_0, N_0) = (450 \text{ MHz}, 1.7 \times 10^{-5}, 4.5 \times 10^{-5})$.

Resonator system	Coupling coefficient $g/(2\pi)$ [MHz]	Critical photon number n_0	Critical atom number N_0	Coupling to dissipation ratio $g/max(\gamma_\perp, \kappa)$	Rate of optical information $R \equiv g^2/max(\gamma_\perp, \kappa)[MHz]$
Fabry-Perot experimental state-of-the-art	110	2.8×10^{-4}	6.1×10^{-3}	7.8	8.6×10^2
Fabry-Perot theoretical limits	770	5.7×10^{-6}	1.9×10^{-4}	36	2.8×10^4
Microsphere experimental (D=120 microns)	24	5.5×10^{-3}	3.0×10^{-2}	7.2	1.7×10^2
Microsphere theory					
Maximum g (D=7.25 micron)	750	6.1×10^{-6}	7.3×10^{-1}	0.01	7.5
Minimum N_0 (D=18 micron)	280	4.3×10^{-5}	3.1×10^{-6}	107	3.0×10^4
Photonic bandgap cavity	17000	7.6×10^{-9}	6.4×10^{-5}	3.9	6.6×10^4
Toroidal microcavity theory					
Maximum g	> 700	6.0×10^{-6}	2.0×10^{-4}	40	2.8×10^4
Minimum N_0	430	2.0×10^{-5}	2.0×10^{-7}	165	7.1×10^4

Table 5.1: Summary of the relevant parameters for cavity QED for a variety of resonator systems. The table shows both the experimental state-of-the-art [90] and the theoretically predicted limits for a Fabry-Perot cavity [91], plus current experimental results with silica microspheres [89]. Furthermore, a theoretical comparison between silica microspheres [90], photonic bandgap cavities [92], and toroidal microresonators (this work) is also given. The results indicate that toroidal cavities can uniformly exceed the performance on these parameters for both FP cavities and silica microspheres. Comparison with PBG cavities indicates that toroids possess dramatically lower atom-cavity coupling strengths (as a result of their much larger mode volumes), but can still result in an improvement in critical atom number due to their very large quality factors.

Table 5.1 gives a comparison of toroidal cavities to some other types of microcavities commonly employed or suggested for strong coupling cQED experiments. To date, most experimental work has involved the use of Fabry-Perot cavities, with current state-of-the-art fabrication technology allowing the attainment of coupling strengths of 110 MHz, with corresponding critical atom numbers of 6×10^{-3}. Estimates on the theoretical performance limits of FP cavities have also been investigated [91], predicting coupling rates as large as 770 MHz, with a corresponding critical atom number of 2×10^{-4}. While this level of performance may be theoretically possible, the current necessity of expensive and sophisticated high-reflection dielectric mirror coatings does not bode well for easy improvements with respect to current technology. This is one of the reasons silica microspheres are of such high interest. Observation of the limits possible with silica microspheres [90] shows that not only is it possible to obtain high values of atom-cavity coupling solely by changing the cavity diameter, which is easily in the realm of current fabrication capability, but their ultra-high quality factors result in dramatic improvement in the critical atom number, with values approaching 3×10^{-6} possible provided that silica absorption-limited quality factors can be obtained. Even if quality factors were in the range of a couple hundred million, which are readily achievable, critical atom numbers around 10^{-4} would occur, comparable to the FP limit. Comparison with the results of this work, we see that not only can toroidal cavities attain coupling strengths comparable to or exceeding those possible with both FP and microsphere cavities, but at the same time possess much lower critical atom numbers. As discussed previously, this arises from the extra level of geometrical control possible in a toroidally-shaped cavity, which allows one to retain both the high-coupling strength representative of small-mode volume cavities while preserving the high-quality factors representative of large whispering-gallery-mode cavities. Clearly, this fact, along with other advantages in control and reproducibility over spherical cavities suggest these structures are highly desirable for cQED experiments.

Lastly, comparison with photonic bandgap cavities are also given. Due to the realization of optical mode volumes near the fundamental limit in a dielectric cavity [42], combined with recent results demonstrating reasonably high quality factors ($\sim$ 45000) [41], these cavities are strong candidates for chip-based strong-coupling cQED [92]. While these structures can possess massive atom-cavity coupling strengths (>17 GHz), far greater than those possible in

a silica dielectric cavity, their much lower quality factors still result in greater critical atom numbers than toroidal microcavities. I must also point out that not only do the extremely large atom-cavity coupling rates greatly exceed the hyperfine splitting in atomic cesium, but the correspondingly lower quality factors also result in modest ratios of coupling to dissipation $g/max(\gamma_\perp, \kappa)$ (which is indicative of the number of Rabi oscillations which occur) of 4, much lower than predicted for toroidal structures (165). Furthermore, we can consider an overall figure of merit of the "rate of optical information per atom" [30], given by $R \equiv g^2/max(\gamma_\perp, \kappa)$. The table indicates that toroidal cavities compare favorably with PBG cavities in this figure of merit as well.

This work has demonstrated that toroidal resonators are promising cavities for investigation of the coupling of an atomic system to the electromagnetic field in the regime of strong-coupling. Not only are these structures arguably simpler to manufacture and control than other structures, but also are integrated on a silicon chip, paving the way for the addition of atom traps [93] and waveguides which can enhance the capability and possibly reduce the experimental complexity of cQED studies. Furthermore, in addition to the enhanced performance benefit of having a toroidal geometry, the capability to retain a relatively large resonator diameter over other structures results in a smaller free-spectral range (FSR). This allows not only an easier tuning of the cavity resonance location to precisely correspond to the atomic transition wavelength, but also may allow integration of a supplemental far-off-resonance trap by exciting the cavity at a multiple of the free-spectral range. The realization of a cavity with a smaller FSR may allow a closer matching of a secondary resonance location to the pump wavelength which corresponds to state-insensitive trapping of atomic cesium [94], which can simplify the atom-cavity dynamics. The use of a dielectric whispering-gallery-cavity also allows operation over a broad range of wavelengths, with very high quality factors possible for nearly all resonances, which is in strong contrast to the mirror reflectivity of FP cavities and the designs of PBG cavities.

As a further note, the use of higher-index contrast dielectric material can allow additional improvements in the performance of these structures. The use of silica as the dielectric of choice in both the spherical geometry and in the toroidal microcavities studied in this work was convenient, as these structures not only possess record high quality factors but are currently

producible. However, as the radiative quality factor of a whispering-gallery-type cavity is strongly dependent on the refractive index difference between the structure and the external environment, much smaller modal volumes are possible for a given quality factor with the use of a higher-index resonator material. In fact, this is one of the reasons PBG cavities fabricated from silicon or other high-index dielectrics can obtain such miniscule mode volumes. A simple comparison of the mode volumes possible in a silicon toroid show that mode volumes on the order of only 10 or so times larger than PBG cavities is possible, with much higher quality factors. While this work has focused on silica microcavities, as these structures are currently manufacturable, the reflow process is a relatively flexible method, thus suggesting that it may be possible to also create high-index very high quality factor cavities which come closer to the massive coupling strengths of PBG cavities while further extending the lead in terms of critical atom number.

And lastly, the current experimental ability to obtain large coupling strengths with quality factors exceeding 100 million is promising for the immediate use of these structures for strong-coupling studies, and we are currently pressing forward on improving the fabrication capabilities and losses of these structures. Coupled with the intrinsic fiber-optic compatibility of these structures, and the demonstration of near lossless excitation and extraction of optical energy from these structures using tapered optical fibers, toroidal microcavities can provide a highly advantageous experimental system for the investigation of strong-coupling cavity QED.

Chapter 6

Summary

This thesis has investigated the suitability of fiber-coupled ultra-high-Q silica microresonators for nonlinear optics and strong-coupling cavity quantum electrodynamics. First, the fabrication and modal characteristics of silica microspheres and silica toroidal microresonators were presented. As the optical modes in a toroidal structure are not analytically solvable, a two-dimensional finite-element simulation was developed to calculate the optical modes of circularly-symmetric microresonators. It was shown that not only do toroidal cavities have a non-degenerate mode structure, but that significant reductions in both modal volume and radiation quality factor can occur for highly-confined toroidal cavities. By using an intuitive model to understand the optical behavior of this structure, a simple approximate formula for the scaling of the modal volume was derived, which gives excellent agreement (error $< 5\%$) over the entire geometrical range.

In order to determine the ability to realize low threshold nonlinear and quantum effects in these microcavities with low incident powers, the coupling properties of fiber-taper waveguides was studied. A simple theoretical harmonic oscillator model and coupled mode theory was introduced to understand the conditions required for optimal coupling both to and from the microcavity. It was shown that at the typical fiber diameters necessary to phase-match the microcavity the fiber supported multiple guided modes. This influence of higher-order fiber coupling was investigated by introducing a new transformation which allowed accurate measurement of the extra coupling-induced loss. Experimental results indicted that not only can the higher-order mode structure of the fiber dramatically affect the fiber transmission behavior, but by proper control of fiber diameter and resonator mode high ideality could be attained. An experimental ideality exceeding 99.97% was obtained, which allowed an overcou-

pled transmission of 99.95%.

The threshold for third-order nonlinear effects in a silica microcavity was investigated theoretically, with predicted thresholds for stimulated Raman scattering and parametric oscillation found to be below 100 microwatts for a typical ultra-high-Q microcavity (quality factor of 100 million). These thresholds scale linearly with mode volume and inversely quadratic with quality factor. Experimental studies in silica microspheres showed multiline stimulated Raman scattering at a record low threshold of 62 microwatts, with conversion efficiencies of 35%. Toroidal resonators were found to have single azimuthal mode emission, as a consequence of their non-degenerate mode spectrum. Highly nonlinear wave conversion was observed for input powers up to 26 mW, with a single line Raman output power of 2.6 mW.

Lastly, a calculation on the performance of silica microtoroids for strong-coupling cavity quantum electrodynamics was given. The two geometrical degrees of freedom in a toroidal cavity allowed the creation of a small mode volume cavity (40 cubic microns) with high overall quality factor ($> 10^{10}$). Coupling strengths exceeding 700 MHz were predicted for coupling to atomic cesium at 852 nm, with critical atom numbers approaching 10^{-7}.

Bibliography

[1] V. B. Braginsky, M. L. Gorodetsky, and V. S. Ilchenko. Quality-factor and nonlinear properties of optical whispering-gallery modes. *Phys. Lett. A*, 137:393–397, May 1989.

[2] Richard K. Chang and Anthony J. Campillo, editors. *Optical Processes in Microcavities*. World Scientific, 1996.

[3] D. W. Vernooy, V. S. Ilchenko, H. Mabuchi, E. W. Streed, and H. J. Kimble. High-Q measurements of fused-silica microspheres in the near infrared. *Optics Letters*, 23(4):247–249, February 1998.

[4] K. J. Vahala. Optical microcavities. *Nature*, 424(6950):839–846, August 2003.

[5] F. Vollmer, D. Braun, A. Libchaber, M. Khoshsima, I. Teraoka, and S. Arnold. Protein detection by optical shift of a resonant microcavity. *Appl. Phys. Lett.*, 80(21):4057–4059, May 2002.

[6] V. Sandoghdar, F. Treussart, J. Hare, V. Lefevre-Seguin, J. M. Raimond, and S. Haroche. Very low threshold whispering-gallery-mode microsphere laser. *Phys. Rev. A*, 54(3):R1777–R1780, September 1996.

[7] R. W. Boyd. *Nonlinear Optics*. Academic Press, Boston, 2000.

[8] S.-X. Qian and R. K. Chang. Multiorder Stokes emission from micrometer-size droplets. *Phys. Rev. Lett.*, 56(9):926–929, March 1986.

[9] H. B. Lin, A. L. Huston, J. D. Eversol, and A. J. Campillo. Double-resonance stimulated Raman scattering in micrometer-sized droplets. *J. Opt. Soc. Am. B*, 7:2079–2089, 1990.

[10] J. Z. Zhang and R. K. Chang. Generation and suppression of stimulated Brillouin scattering in single liquid droplets. *J. Opt. Soc. Am. B*, 6:151–153, 1989.

[11] G. P. Agrawal. *Nonlinear Fiber Optics*. Academic Press, San Diego, 2001.

[12] L. S. Meng, P. A. Roos, K. S. Repasky, and J. L. Carlsten. High-conversion-efficiency, diode-pumped continuous-wave Raman laser. *Opt. Lett.*, 26(7):426–429, April 2001.

[13] L. Collot, V. Lefevre-Seguin, M. Brune, J. M. Raimond, and S. Haroche. Very high-Q whispering-gallery mode resonances observed on fused-silica microspheres. *Europhys. Lett.*, 23(5):327–334, August 1993.

[14] D. Braunstein, A. M. Khazanov, G. A. Koganov, and R. Shuker. Lowering of threshold conditions for nonlinear effects in a microsphere. *Phys. Rev. A*, (53):3565–3572, 1996.

[15] V. S. Ilchenko and M. L. Gorodetsky. Thermal nonlinear effects in optical whispering gallery microresonators. *Laser Phys.*, 2:1004–1009, 1992.

[16] F. Treussart, V. S. Ilchenko, J.-F. Roch, J. Hare, V. Leferve-Seguin, J.-M. Raimond, and S. Haroche. Evidence for intrinsic Kerr bistability of high-Q microsphere resonators in superfluid helium. *Euro. Phys. J. D*, 1(3):235–238, March 1998.

[17] M. L. Gorodetsky and V. S. Ilchenko. High-Q optical whispering-gallery microresonators: precession approach for spherical mode analysis and emission patterns with prism couplers. *Opt. Commun.*, 113:133–143, December 1994.

[18] A. Serpenguzel, S. Arnold, and G. Griffel. Excitation of resonances of microspheres on an optical fiber. *Opt. Lett.*, 20:654–656, 1995.

[19] J. C. Knight, G. Cheung, F. Jacques, and T. A. Birks. Phase-matched excitation of whispering-gallery-mode resonances by a fiber taper. *Opt. Lett.*, 22(15):1129–1131, August 1997.

[20] M. Cai, O. J. Painter, and K. J. Vahala. Observation of critical coupling in a fiber taper to a silica-microsphere whispering-gallery mode system. *Phys. Rev. Lett.*, 85(1):74–77, July 2000.

[21] S. M. Spillane, T. J. Kippenberg, O. J. Painter, and K. J. Vahala. Ideality in a fiber-taper-coupled microresonator system for application to cavity quantum electrodynamics. *Phys. Rev. Lett.*, 91(4):043902, July 2003.

[22] S. M. Spillane, T. J. Kippenberg, and K. J. Vahala. Ultralow-threshold raman laser using a spherical dielectric microcavity. *Nature*, 415(6872):621–623, February 2002.

[23] S. L. McCall, A. F. J. Levi, R. E. Slusher, S. J. Pearton, and R. A. Logan. Whispering-gallery mode microdisk lasers. *Appl. Phys. Lett.*, 60:289–291, 1992.

[24] Payam Rabiei, William H. Steier, Cheng Zhang, and Larry R. Dalton. Polymer micro-ring filters and modulators. *J. Lightwave Tech.*, 20(11):1968–1975, November 2002.

[25] D. K. Armani, T. J. Kippenberg, S. M. Spillane, and K. J. Vahala. Ultra-high-Q toroid microcavity on a chip. *Nature*, 421:925–929, February 2003.

[26] T. J. Kippenberg, S. M. Spillane, D. K. Armani, and K. J. Vahala. Ultralow-threshold microcavity Raman laser on a microelectronic chip. *Opt. Lett.*, 29(11), June 2004.

[27] L. Yang, D.Armani, and K. J. Vahala. Fiber-coupled erbium microlasers on a chip. *Appl. Phys. Lett.*, 83(5):825–826, August 2003.

[28] E. M. Purcell. Spontaneous emission probabilities at radio frequencies. *Phys. Rev.*, 69:681, 1946.

[29] D. Kleppner. Inhibited spontaneous emission. *Phys. Rev. Lett.*, 47:233–236, 1981.

[30] H. J. Kimble. Strong interactions of single atoms and photons in cavity QED. *Physica Scripta*, T76:127–137, 1998.

[31] D. Bouwmeester, A. Ekert, and A. Zeilinger, editors. *The Physics of Quantum Information*. Springer, Berlin, 2000.

[32] L.-M. Duan, A. Kuzmich, and H. J. Kimble. Cavity QED and quantum information processing with hot trapped atoms. *Phys. Rev. A*, 67(3):032305, March 2003.

[33] M. Hennrich, T. Legero, A. Kuhn, and G. Rempe. Vacuum-stimulated Raman scattering based on adiabatic passage in a high-finesse optical cavity. *Phys. Rev. Lett.*, 85(23):4872–4875, December 2000.

[34] J. I. Cirac, P. Zoller, H. J. Kimble, and H. Mabuchi. Quantum state transfer and entanglement distribution among distant nodes in a quantum network. *Phys. Rev. Lett.*, 78(16):3221–3224, April 1997.

[35] A. Kuzmich, W. P. Bowen, A. D. Boozer, A. Boca, C. W. Chou, L.-M. Duan, and H. J. Kimble. Generation of nonclassical photon pairs for scalable quantum communication with atomic ensembles. *Nature*, 423:731–734, June 2003.

[36] L.-M. Duan, M. D. Lukin, J. I. Cirac, and P. Zoller. Long-distance quantum communication with atomic ensembles and linear optics. *Nature*, 414:413–418, 2001.

[37] M. L. Gorodetsky, A. D. Pryamikov, and V. S. Ilchenko. Rayleigh scattering in high-Q microspheres. *J. Opt. Soc. Am. B*, 17(6):1051–1057, June 2000.

[38] H. A. Haus. *Waves and Fields in Optoelectronics*. Prentice-Hall, Englewood Cliffs, NJ, 1984.

[39] B. E. Little, J. S. Foresi, G. Steinmeyer, E. R. Thoen, S. T. Chu, H. A. Haus, E. P. Ippen, L. C. Kimerling, and W. Greene. Ultra-compact Si-Si02 microring resonator optical channel dropping filters. *Photon. Tech. Lett.*, 10:549–551, April 1998.

[40] K. Srinivasan, P. E. Barclay, O. Painter, J. Chen, A. Y. Cho, and C. Gmachl. Experimental demonstration of a high-Q photonic crystal microcavity. *Appl. Phys. Lett.*, 83(10):1915–1917, September 2003.

[41] Y. Akahane, T. Asano, B.-S. Song, and S. Noda. High-Q photonic nanocavity in a two-dimensional photonic crystal. *Nature*, 425:944–947, October 2003.

[42] J. Vuckovic, M. Loncar, H. Mabuchi, and A. Scherer. Design of photonic crystal microcavities for cavity QED. *Phys. Rev. E*, 65(1):016608, December 2001.

[43] D. W. Vernooy and H. J. Kimble. Quantum structure and dynamics for atom galleries. *Phys. Rev. A*, 55(2):1239–1261, February 1997.

[44] J. A. Stratton. *Electromagnetic Theory*. McGraw Hill, New York, NY, 1997.

[45] Brent E. Little, J.-P. Laine, and Hermann A. Haus. Analytic theory of coupling from tapered fibers and half-blocks into microsphere resonators. *J. Light. Tech.*, 17(4):704–715, April 1999.

[46] L. A. Weinstein. *Open Resonators and Open Waveguides*. The Golem Press, Boulder, CO, 1969.

[47] C. C. Lam, P. T. Leung, and K. Young. Asymptotic formulas for the positions, widths, and strengths of resonances in Mie scattering. *J. Opt. Soc. Am. B*, 9(9):1585–1592, September 1992.

[48] S. Schiller. Asymptotic expansion of morphological resonance frequencies in Mie scattering. *Appl. Opt.*, 32(12):2181–2185, April 1993.

[49] M. L. Gorodetsky, A. A. Savchenkov, and V. S. Ilchenko. Ultimate Q of optical microsphere resonators. *Optics Letters*, 21(7):453–455, April 1996.

[50] G. M. Hale and M. R. Querry. Optical constants of water in the 200 nm to 200 micron wavelength region. *Appl. Opt.*, 12:555–563, 1973.

[51] D. A. Pinnow, T. C. Rich, Jr. F. W. Ostermayer, and Jr. M. DiDomenico. Fundamental optical attenuation limits in the liquid and glassy state with application to fiber optical waveguide materials. *Appl. Phys. Lett.*, 22(10):527–529, May 1973.

[52] A. Himeno, K. Kato, and T. Miya. Silica-based planar lightwave circuits. *IEEE J. Sel. Top. Quant.*, 4:913–924, 1998.

[53] M. Delfino and T. A. Reifsteck. Laser-activated flow of phosphosilicate glass in integrated circuit devices. *Elect. Dev. Lett.*, 3:116–118, 1982.

[54] T. J. Kippenberg, S. M. Spillane, and K. J. Vahala. Fabrication and coupling to planar high-Q silica disk microcavities. *Appl. Phys. Lett.*, 83(4):797–799, July 2003.

[55] V. S. Ilchenko, M. L. Gorodetsk, X. Yao, and L. Maleki. Microtorus: a high-finesse microcavity with whispering-gallery modes. *Opt. Lett.*, 26(5):256–259, March 2001.

[56] V. S. Ilchenko, D. S. Starodubov, M. L. Gorodetsky, L. Maleki, and J. Feinberg. Coupling light from a high-Q microsphere resonator using a UV-induced surface grating. In *CLEO Technical Digest*, page 67, Baltimore, May 1999.

[57] V. S. Ilchenko, X. S. Yao, and L. Maleki. Pigtailing the high-Q microsphere cavity: a simple fiber coupler for optical whispering-gallery modes. *Opt. Lett.*, 24(11):723–725, June 1999.

[58] H. Ishikawa, H. Tamaru, and K. Miyano. Microsphere resonators strongly coupled to a plane dielectric substrate: coupling via the optical near field. *J. Opt. Soc. Am. A*, 17(4):802–813, April 2000.

[59] H. Ishikawa, H. Tamaru, and K. Miyano. Optical coupling between a microresonator and an adjacent dielectric structure: effects of resonator size. *J. Opt. Soc. Am. B*, 18(6):762–769, June 2001.

[60] J. P. Laine, B. E. Little, D. R. Lim, H. C. Tapalian, L. C. Kimerling, and H. A. Haus. Planar integrated wavelength-drop device based on pedestal antiresonant reflecting waveguides and high-Q silica microspheres. *Opt. Lett.*, 25(22):1636–1638, November 2000.

[61] J. P. Laine, B. E. Little, D. R. Lim, H. C. Tapalian, L. C. Kimerling, and H. A. Haus. Microsphere resonator mode characterization by pedestal anti-resonant reflecting waveguide coupler. *IEEE Phot. Tech. Lett.*, 12(8):1004–1006, August 2000.

[62] Allan W. Snyder and John D. Love. *Optical Waveguide Theory*. Chapman and Hall, 1983.

[63] Amnon Yariv. *Optical Electronics in Modern Communications*. Oxford University Press, New York, 5 edition, 1997.

[64] H. A. Haus and W. Huang. Coupled-mode theory. *Proc. IEEE*, 79(10):1505–1518, October 1991.

[65] Masanori Matsuhara and A. Watanabe. Coupling of curved transmission lines, and application to optical directional couplers. *J. Opt. Soc. Am.*, 65(2):163–168, February 1975.

[66] D. R. Rowland and J. D. Love. Evanescent wave coupling of whispering gallery modes of a dielectric cylinder. *IEE Proceedings-J*, 140(3):177–188, June 1993.

[67] M. L. Gorodetsky and V. S. Ilchenko. Optical microsphere resonators: optimal coupling to high-Q whispering-gallery modes. *J. Opt. Soc. Am. B*, 16(1):147–154, January 1999.

[68] The equivalence of the coupling amplitudes both into and out of the resonator is true only when time-reversal symmetry and power conservation applies, however as will be shown later the coupling junction is nearly lossless so this approximation is justified.

[69] D. S. Weiss, V. Sandoghdar, J. Hare, V¿ Lefevre-Seguin, J. M. Raimond, and S. Haroche. Splitting of high-Q Mie modes induced by light backscattering in silica microspheres. *Opt. Lett.*, 20(18):1835–1838, September 1995.

[70] T. J. Kippenberg, S. M. Spillane, and K. J. Vahala. Modal coupling in traveling-wave resonators. *Optics Letters*, 27(19):1669–1671, October 2002.

[71] A. J. Campillo, J. D. Eversol, and H.-B. Lin. Cavity quantum electrodynamic enhancement of stimulated emission in microdroplets. *Phys. Rev. Lett.*, 67:437–440, 1991.

[72] M. Cai, O. J. Painter, K. J. Vahala, and P. C. Sercel. Fiber-coupled microsphere laser. *Opt. Lett.*, 25:1430–1432, 2000.

[73] H.-B. Lin and A. J. Campillo. Microcavity enhanced Raman gain. *Opt. Comm.*, 133:287–292, January 1997.

[74] Y. Wu, X. Yang, and P. T. Leung. Theory of microcavity-enhanced Raman gain. *Opt. Lett.*, 24(5):345–347, March 1999.

[75] R. H. Stolen and J. E. Bjorkholm. Parametric amplification and frequency-conversion in optical fibers. *IEEE J. Quant. Elect.*, 18(7):1062–1072, 1982.

[76] R. H. Stolen and E. P. Ippen. Raman gain in glass optical waveguides. *Appl. Phys. Lett.*, 22(6):276–278, 1973.

[77] H. M. Lai, P. T. Leung, K. Young, P. W. Barber, and S. C. Hill. Time-independent perturbation for leaking electromagnetic modes in open systems with application to resonances in microdroplets. *Phys. Rev. A*, 41:5187–5198, 1990.

[78] B. K. Min, T. J. Kippenberg, and K. J. Vahala. Compact, fiber-compatible, cascaded raman laser. *Opt. Lett.*, 28(17):1507–1509, September 2003.

[79] H. B. Lin and A. J. Campillo. CW nonlinear optics in droplet microcavities displaying enhanced gain. *Phys. Rev. Lett.*, 73:2440–2443, 1994.

[80] A. B. Matsko, A. A. Savchenkov, R. J. Letargat, V. S. Ilchenko, and L. Maleki. On cavity modification of stimulated raman scattering. *J. Opt. B*, 5:272–278, June 2003.

[81] V. S. Ilchenko, A. A. Savchenko, A. B. Matsko, and L. Maleki. Nonlinear optics and crystalline whispering gallery mode cavities. *Phys. Rev. Lett.*, 92(4):043903, January 2004.

[82] T. J. Kippenberg. *Nonlinear Optics in Ultra-high-Q Whispering-Gallery Optical Microcavities*. PhD thesis, Caltech, 2004.

[83] H. Mabuchi and A. C. Doherty. Cavity quantum electrodynamics: coherence in context. *Science*, 298:1372–1377, November 2002.

[84] H. Mabuchi, J. Ye, and H. J. Kimble. Full observation of single-atom dynamics in cavity QED. *Appl. Phys. B*, 68:1095–1108, March 1999.

[85] C. J. Hood, T. W. Lynn, A. C. Doherty, A. S. Parkins, and H. J. Kimble. The atom-cavity microscope: single atoms bound in orbit by single photons. *Science*, 287:1447–1453, 2000.

[86] J. McKeever, A. Boca, A. D. Boozer, J. R. Buck, and H. J. Kimble. Experimental realization of a one-atom laser in the regime of strong coupling. *Nature*, 425:268–271, September 2003.

[87] V. Lefevre-Seguin and S. Haroche. Towards cavity-QED experiments with silica microspheres. *Mat. Sci. Eng. B-Solid*, 48:53–58, August 1997.

[88] F. Treussart, J. Hare, L. Collot, V. Lefevre, D. S. Weiss, V. Sandoghdar, J. M. Raimond, and S. Haroche. Quantized atom-field force at the surface of a microsphere. *Opt. Lett.*, 19(20):1651–1653, October 1994.

[89] D. W. Vernooy, A. Furusawa, N. P. Georgiades, V. S. Ilchenko, and H. J. Kimble. Cavity QED with high-Q whispering gallery modes. *Phys. Rev. A*, 57(4):R2293–R2296, April 1998.

[90] J. R. Buck and H. J. Kimble. Optimal sizes of dielectric microspheres for cavity QED with strong coupling. *Phys. Rev. A*, 67(3):033806, March 2003.

[91] C. J. Hood, H. J. Kimble, and J. Ye. Characterization of high-finesse mirrors: Loss, phase shifts, and mode structure in an optical cavity. *Phys. Rev. A*, 64(3):033804, August 2001.

[92] B. Lev, K. Srinivasan, P. Barclay, O. Painter, and H. Mabuchi. Feasibility of detecting single atoms using photonic bandgap cavities.

[93] W. Hansel, P. Hommelhoff, T. W. Hansch, and J. Reichel. Bose-Einstein condensation on a microelectronic chip. *Nature*, 413:498–501, 2001.

[94] J. McKeever, J. R. Buck, A. D. Boozer, A. Kuzmich, H.-C. Naegerl, D. Stamper-Kurn, and H. J. Kimble. State-insensitive trapping and cooling of single atoms in cavity QED. *Phys. Rev. Lett.*, 90(13):133602, April 2003.

[95] J. Jin. *The Finite Element Method in Electromagnetics*. Wiley, 2002.

[96] A. Taflove and S. C. Hagness. *Computational Electrodynamics: The Finite-Difference Time-Domain Method*. Artech House, 2000.

[97] Y. Chen, R. Mittra, and P. Harms. Finite-difference time-domain algorithm for solving Maxwell's equations in rotationally symmetric geometries. *IEEE Trans. Microwave Theory Tech.*, 44(6):832–839, June 1996.

[98] D. W. Prather and S. Shi. Formulation and application of the finite-difference time-domain method for the analysis of axially symmetric diffractive optical elements. *J. Opt. Soc. Am. A*, 16(5):1131–1142, May 1999.

Appendix A: Numerical simulation of optical whispering-gallery-mode microcavities

Obviously, analytic expressions are the preferred way to investigate the properties of any system. However, theoretically solvable expressions cannot in general account for the experimental and practical realities involved in studying physical processes in nature. The study of microresonators based on spherical cavities has been greatly facilitated by the ability to analytically determine the resonant structure and optical properties to a large degree of accuracy. This is a consequence of the complete separability of the governing Helmholtz equation in spherical coordinates, which reduces the eigenvalue problem to one dimension. Other cavity designs of interest in microresonator studies do not, however, possess this inherent separability into an easily solvable reduced dimension. While analytic approximations can be obtained for individual cases in certain regimes, and can give valuable insight into the structure's behavior, full knowledge of the complete properties is not available. Numerical techniques can be used to gain insight into the behavior of these systems. Two main numerical techniques, finite element (FE) and finite difference time domain (FDTD) simulation, were used in this work to investigate the properties of optical microresonators.

A.1 Finite element modeling of optical modes

Finite element methods [95] are commonly used to simulate physical systems, from heat-flow to structural mechanics. This method consists of breaking the system down into a patchwork of individual elements, with an element dimension chosen such that both the problem parameters and desired solution has a small variation over each element. The dimensions of each element do not have to be identical, thus allowing more, smaller elements to be located wherever the

solution and/or geometrical features vary quickly. Each individual element, which is typically a triangular area in two dimensions and pyramidal in three dimensions, is then related to all neighboring elements through the governing equation of the problem to be solved, such as Helmholtz's equation for eigenvalue/eigenfunction problems in electromagnetics. This results in a set of equations relating each element to its neighbors, which can be written in a matrix form. This matrix equation then is solved to obtain the problem solution.

Finite element methods have a number of advantages over other approaches, in particular finite difference time domain techniques, when modeling high-Q resonators. First, when considering typical high-Q optical resonators the cavity boundaries are curvilinear functions, which are hard to model with FDTD without either choosing a nonstandard grid or very densely gridding the entire computation region to minimize the "staircase effect." FE methods, on the other hand, easily allow the element boundaries to follow local geometric boundaries. Secondly, the ability to vary the element size over the computation region results in a much smaller amount of data which must be stored for comparable accuracy when compared to FDTD. This results in a considerable memory savings, which in turn allows larger regions to be simulated. And lastly, the computation time is dramatically lower than FDTD for certain problems in this work. In particular, the necessity of long simulation times for high-Q resonators (because of the slow temporal decay of the optical energy), coupled with the dense spatial grid required for numerical stability, result in a computation time which is over an order of magnitude larger.

A commercial finite element simulation package (FEMLAB) was chosen to model the resonant structure of the microresonators studied in this work. This particular package is integrable with MATLAB and possesses many visualization and post-processing tools. Additionally, this software already contains a significant amount of electromagnetic-specific tools, such as vector elements, which greatly facilitate the study of EM problems. However, the preprogrammed electromagnetic tools are not directly applicable to solve the resonant spectrum of azimuthally-symmetric resonators, so new expressions must be derived which do represent the correct problem.

As the resonators studied in this work possess an axis of symmetry, the dimensionality of the eigenvalue problem can by reduced to two dimensions by explicitly accounting for the

azimuthal symmetry. Cylindrical coordinates are used so that the cross-sectional coordinates (r, z) remain Cartesian. Substituting the azimuthal phi-dependence $e^{im\phi}$ into the governing equation for the electric field, derived from Maxwell's equations, and assuming a steady-state solution for an eigenvalue problem, the ϕ dependence vanishes and we are left with a vector equation in a Cartesian (r, z) coordinate basis. This vector equation is in fact three equations, one for each electric field component. Thus, each sub-equation can be manipulated independently, and reordered into the general form used by FEMLAB. The resulting expression is exact, and accounts for the full-vectorial nature of Maxwell's equations. Thus not only are both optical polarizations directly solvable, but there is no restriction to weak-guiding or low contrast structures. The input parameters consist of the problem geometry (including the electric and magnetic index profiles), and the azimuthal mode number m.

These expressions were used to model the resonant spectrum and modes of microresonator structures. In order to verify the numerical technique, both the resonance locations and fields were compared with the analytically-known case of a spherical cavity. It was found that the fractional error in the location of the optical resonances was less than 10^{-4}. Calculations of the modal volume indicated a deviation from the theoretical value of less than 1%.

The radiation loss of a microresonator cavity is also an important quantity to determine, as this loss mechanism puts a limiting factor on the total performance of the cavity. This loss is a result of the curved cavity boundary in the azimuthal direction coupled with an infinite outer boundary, such that any radiated energy does not get reflected back into the cavity. The need for an infinite outer boundary presents a difficulty when trying to numerically calculate the radiation loss of a cavity. The preferred solution to this problem is to implement an artificial boundary that possesses the properties of an infinite one; appear transparent and absorb all incident optical energy, such that there is minimal energy reflected back into the domain of interest. This type of boundary is known as a perfectly-matched layer (PML). There has been a great deal of effort developing and characterizing this type of boundary condition for the FDTD method, where the shrinking of the computation boundary results in a huge reduction of computation effort. Use in finite element electromagnetics has garnered significantly less attention.

I have implemented a PML boundary in the FE method described above, in order to

determine the radiation loss of microcavities. In principle, the presence of the boundary (which consists of an anisotropic complex dielectric medium) results in a complex valued resonance k-vector, which can be simply converted into a radiation-limited quality factor, $Q_{rad} = \Re(k)/(2 * \Im(k))$. This indicates that the FE method can be used to calculate the radiation loss of rotationally-symmetric structures with high accuracy. However, a FDTD model was also used to provide further confirmation on the accuracy of the numerical modelling. Figure A.1 shows the error for the radiation loss from a spherical cavity at a wavelength near 850 nm as a function of sphere diameter. Both TM and TE polarized fundamental modes are calculated and compared to the exact solution obtained by numerically solving the characteristic equation for a spherical cavity (equation 2.9). The error is observed to be less than 10% over a range exceeding 11 orders of magnitude (10^3 to 10^{14}), which indicates that this method can give the accuracy needed for investigating ultra-high-Q whispering-gallery-mode microresonators. For comparison, values determined from FDTD as described in the next section also have reasonable agreement. However, I must note that the approximate formulas derived on the basis of asymptotic expansions of the characteristic equation do not give good agreement. While the general scaling is in line with the actual values as a function of diameter, the actual magnitude for both TE and TM modes are in significant error. While this is most likely due to the fact that the cavity diameters considered here do not fall completely within the range of validity of these approximations, this large error should be considered when predicting the radiative quality factor limit of smaller diameter cavities as studied in this thesis.

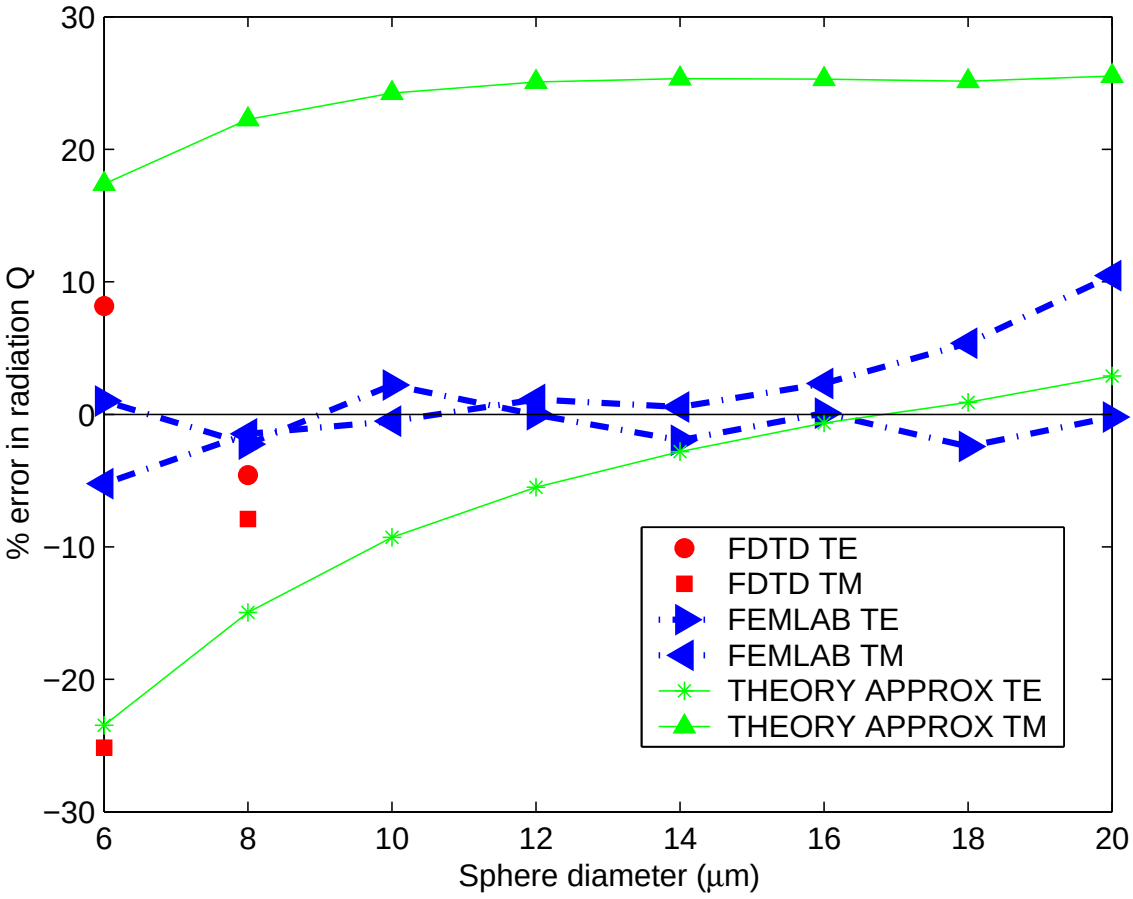

Figure A.1: Comparison of the error in techniques to calculate the radiation loss of spherical cavities. The exact value was found be numerical solution of the characteristic equation for the modes of a microsphere. The data indicate that the finite element method is accurate for both TE and TM polarizations over a wide range of cavity diameters (11 orders of magnitude in radiation Q). Both FDTD and approximate analytic theory points are also shown.

A.2 FDTD modeling of azimuthally symmetric optical resonators

The finite difference time domain method [96] consists of solving Maxwell's curl equations over a discretized time and space lattice. By suitable choice of both the time step and spatial lattice construction, this method is guaranteed to be numerically stable. Commonly, the Yee lattice is used, which consists of a staggered rectangular grid of electric and magnetic fields. This lattice has the nice property of naturally enforcing both Faraday's and Ampere's laws, and thus mimics nature by explicitly solving for both the electric and magnetic fields in an alternating manner.

FDTD has many advantages for modeling electromagnetic systems. For one, this method is fully explicit, and can handle most types of electromagnetic problems, including current sources and nonlinearities. Furthermore, the core algorithms are relatively simple, allowing easy implementation and parallelization. Additionally, the natural analogy of time propagation of electric and magnetic fields as expressed through Maxwell's equations results in modelling results which represent what happens physically. Methods such as Poynting surfaces to determine power flow and current sources to generate incident waves are also readily implemented. Thus, FDTD is often a good choice for modelling microresonator systems, as by just defining the resonator and coupling geometry, along with an excitation field and any required analysis functions, the resonant and coupling properties can be readily obtained.

The simplicity of the typical FDTD approach also is one of its drawbacks when modelling high-Q microresonators. As most implementations use a fixed size Cartesian grid over the entire computational region, modelling three dimensional structures including the excitation waveguide requires a memory storage which exceeds that possible on a typical workstation for simulating the problems of interest in this work. Furthermore, the large number of time steps required to reach steady-state in a high-Q resonator creates an excessive computation time. However, the common availability of PML boundary conditions and Poynting surfaces to determine power flow provide a compelling argument for the use of FDTD to determine the radiation loss of microresonant structures.

To a large degree, the computational inefficiency of typical FDTD modelling of optical

microresonators can be avoided by using the available knowledge of the resonant geometry and structure to reduce the degrees of freedom of the simulation. This was done in two ways. First, the azimuthal symmetry of the microresonators studied in this work suggest that a two-dimensional cross-sectional geometry can be used, dramatically reducing the memory requirements, which allows implementation on a typical desktop computer. This is done by explicitly accounting for the axis of symmetry in the formulation of the FDTD algorithm, in an analogous manner to that done for the FE method described previously. Applying the explicit rotational symmetry to Faraday and Ampere's equation, one can derive a set of equations which determine the time evolution of the electric and magnetic fields. This method, which can be found in the literature as a "body-of-revolution" FDTD algorithm [97], requires the azimuthal mode number m as an input parameter. Furthermore, the application of a PML layer is straightforward [98].

The necessity of a long simulation time in order to allow the optical fields to reach steady-state in the resonator can be avoided by using the optical fields determined by the FE method as input fields in the resonator. As the FE method determines both the fields and spectrum to a large degree of accuracy, this approach allows an effective bypass of the time-consuming step of choosing the proper resonant field to study. And lastly, the influence of the discretized grid on the representation of surfaces which do not follow the grid axes ("staircase effect") is minimized by using a technique where the electric and magnetic indices are averaged over the grid cells which intersect the boundary, giving a large improvement in accuracy without requiring an excessive spatial grid.

The initial electric and magnetic fields were then evolved in time, with a time step chosen to satisfy the stability condition. PML layers were used at both the radial outer boundary and the vertical boundaries, in order to absorb any outgoing energy. A Poynting surface was placed in the radial direction beyond the outer radiation caustic to determine radiated power flow. From knowledge of the time-averaged radiated power $\bar{P}$, and the total stored power in the resonator U, the radiation quality factor can be determined by the relation $Q = \omega U/\bar{P}$, where the optical frequency ω is obtained from the FE solution. Figure A.2 shows the total energy U and the radiated power P versus time step for propagation of a spherical whispering-gallery-mode. The top panel show that the optical energy in the computation

region decreases in time due to the radiated power being absorbed by the PML layers. The bottom panel shows the corresponding power flow through a radial surface located outside the spherical dielectric boundary. The sudden drop in the total energy (and corresponding spike in radiated power) is due the initial mismatch of the FE starting field profiles with the FDTD grid. After approximately 50000 time steps all nonphysical field components are shed, as evidenced by the pure exponential field decay for larger time steps. This corresponds with a near steady-state radiated power, with a slight oscillation due to residual excitation of a counterpropagating wave. Quality factor measurements from both the temporal decay of the optical energy and by using the time-averaged radiated power are in good agreement. Comparison of the determined radiation loss was compared with the analytic solution for a microsphere and matches relatively well. The residual error is attributed to scattering from the discretized spatial grid. The excellent agreement shows that the FDTD implementation is correct.

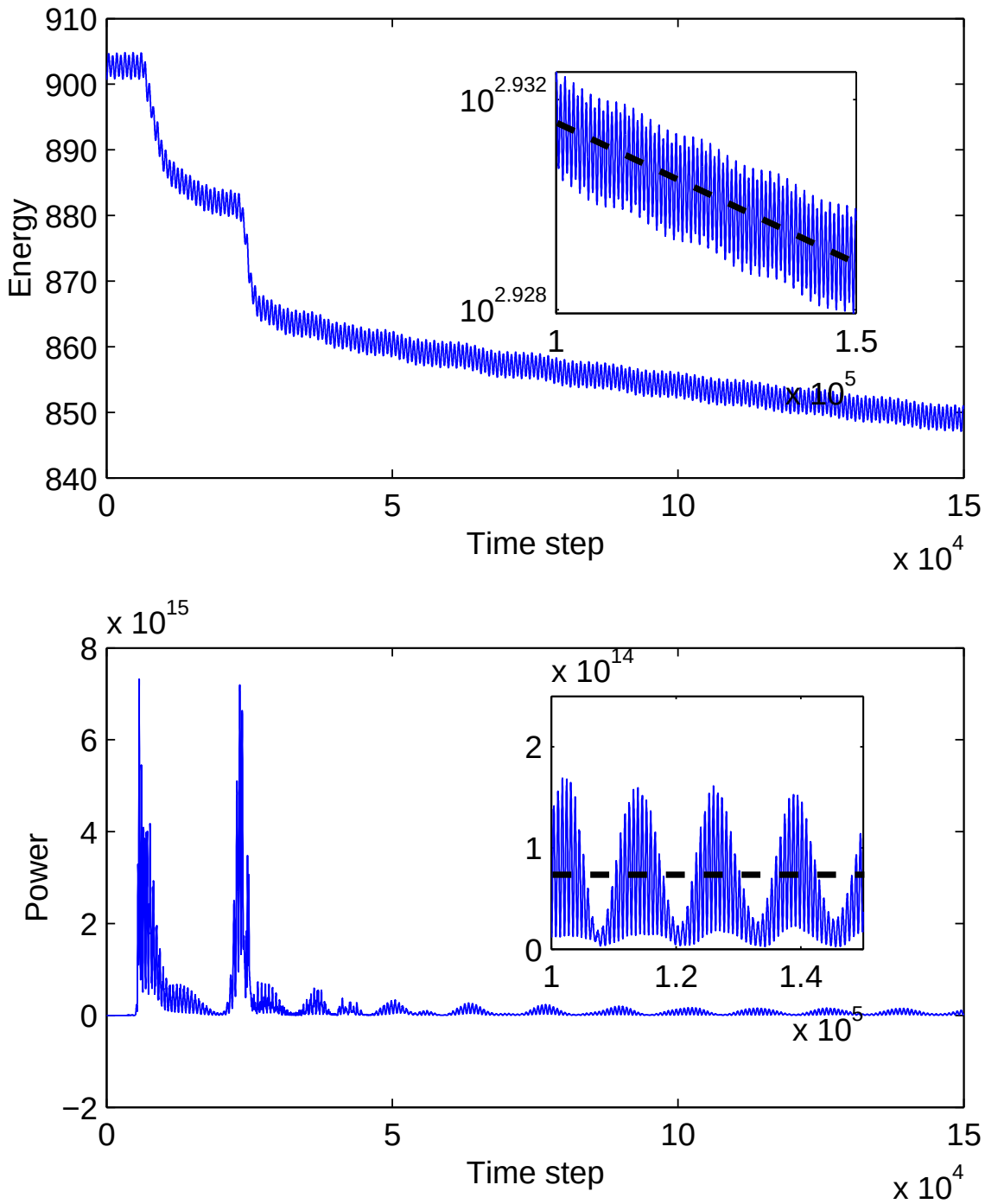

Figure A.2: FDTD determination of the temporal dependence of stored energy and radiated power in a spherical cavity. After an initial period, the stored energy and radiated power match the behavior expected for a microsphere whispering-gallery mode. The residual slow oscillatory behavior for long time steps results from the half-time step difference between the electric and magnetic fields used to compute the total energy and power flow. The calculated quality factor is in good agreement with the theoretical value.